

Small Angle X-ray Scattering Study of Palladium Nanoparticle Growth on Genetically Engineered Tobacco Mosaic Virus Nanotemplates

A thesis
submitted by

Amy K. Manocchi

in partial fulfillment of the requirements for
the degree of

Doctor of Philosophy

in

Chemical Engineering

TUFTS UNIVERSITY

November, 2010

Adviser: Dr. Hyunmin Yi

ABSTRACT:

Transition metal nanoparticles possess valuable specific size dependent properties that arise at the nanoscale, and differ significantly from their bulk properties. However, the fabrication of these nanoparticles is often difficult to predict and control due to harsh reaction conditions and effects of capping agents or surfactants. Therefore, there is a critical need for facile routes toward controllable nanoparticle fabrication. Biological supramolecules, such as viruses, offer attractive templates for nanoparticle synthesis, due to their precise size and shape. In addition, simple genetic modifications can be employed to confer additional functionality with a high number of precisely spaced functional groups. In this work we exploit the specificity of genetically modified Tobacco Mosaic Virus (TMV1cys) for readily controllable palladium (Pd) nanoparticle synthesis via simple electroless deposition. TMV1cys, engineered to display one cysteine residue on the surface of each of over 2000 identical coat proteins, provides high density precisely spaced thiol groups for the preferential nucleation and growth of Pd nanoparticles. Small-Angle X-ray Scattering (SAXS) was employed to provide a statistically meaningful route to the investigation of Pd nanoparticle size ranges formed on the viral-nanotemplates. Specifically, we examine the size range and thermal stability of Pd nanoparticles formed on surface assembled TMV1cys. Further, we investigate the growth of Pd nanoparticles on TMV1cys in solution using *in situ* SAXS to better understand and predict nanoparticle growth on these nanotemplates. Lastly, we compare TMV1cys templated particle

growth to Pd nanoparticle growth in the absence of TMV1cys to elucidate the role of TMV in particle formation.

We show that Pd nanoparticles form preferentially on surface assembled TMV1cys in high density in a broad particle size range (4-18nm). Further, we show that Pd nanoparticles are significantly smaller and more uniform when formed on TMV1cys in solution as compared to Pd particle growth in the absence of TMV1cys. Finally, we provide insight into the fundamental Pd growth mechanism through in depth *in situ* SAXS analysis. We anticipate that this work will have a broad and significant impact on the use of biological supramolecules for the well-controlled fabrication of nanoparticles for a wide range of applications by providing fundamental information on particle growth.

ACKNOWLEDGEMENTS

First, I want to express my sincere gratitude to my advisor, Professor Hyunmin Yi. His patience and support guided me through this entire project and were the key driving force in fulfilling this dissertation.

I also would like to express my appreciation to Dr. Byeongdu Lee. Without his copious amounts of time, valuable guidance and expertise, this work could never have been possible.

Thanks are also owed to my thesis committee members, Professor Nakho Sung and Professor Terry Haas, for their helpful suggestions and valuable time.

Furthermore, I'd like to thank my labmates Cheryl, Christina, Cuixian, Jen, and Jihae for making the long hours in the lab so enjoyable, and for being such wonderful labmates and friends.

Finally, I am grateful for my incredible family, who have always supported and encouraged me through all of the challenging moments.

I owe many thanks to my parents especially, who never stopped believing that I could do *anything* I dreamed of.

TABLE OF CONTENTS

ABSTRACT.....	ii
ACKNOWLEDGEMENTS.....	iv
TABLE OF CONTENTS.....	v
LIST OF FIGURES.....	ix
LIST OF TABLES.....	xii
LIST OF VARIABLES.....	xiii
LIST OF EQUATIONS.....	xv
1 INTRODUCTION.....	1
1.1 Our Approach.....	6
2 SMALL ANGLE X-RAY SCATTERING THEORY.....	9
2.1 General Theory.....	9
2.2 GISAXS.....	13
2.2.1 GISAXS Analysis: Pd Nanoparticles vs. TMV.....	16
2.3 Analysis Methods.....	24
2.3.1 Guinier Analysis.....	24
2.3.2 Size Distributions.....	27
2.3.3 Invariant.....	28
3 PALLADIUM NANOPARTICLE GROWTH ON SURFACE ASSEMBLED TMV1CYS.....	29
3.1 Materials and Methods.....	31

3.1.1	Materials.....	31
3.1.2	TMV1cys Surface Assembly.....	32
3.1.3	Pd Nanoparticle Growth on Surface-Assembled TMV1cys.....	32
3.1.4	Atomic Force Microscopy.....	33
3.1.5	X-ray Photoelectron Spectroscopy.....	34
3.1.6	Transmission Electron Microscopy	34
3.1.7	Grazing Incidence Small-Angle X-ray Scattering.....	34
3.2	Results and Discussion	35
3.2.1	TMV1cys Surface Assembly.....	35
3.2.2	Pd Nanoparticle Formation on Surface-Assembled TMV1cys.....	38
3.2.3	Pd Nanoparticle Size Control Using Sodium Hypophosphite.....	42
3.3	Conclusions	58
4	THERMAL STABILITY OF SURFACE ASSEMBLED PD-TMV COMPLEXES	59
4.1	Materials and Methods	61
4.1.1	Materials.....	61
4.1.2	Sample Preparation.....	61
4.1.3	<i>In situ</i> Grazing Incidence Small-Angle X-ray Scattering..	61
4.2	Results and Discussion	62
4.2.1	Analysis of GISAXS Images.....	62

4.2.2	Analysis of GISAXS Curves.....	65
4.2.3	AFM Analysis of Degraded Surfaces.....	76
4.3	Conclusions	79
5	<i>IN SITU SAXS ANALYSIS OF Pd NANOPARTICLE GROWTH MECHANISM, IN THE ABSENCE OF TMV</i>	81
5.1	Materials and Methods	85
5.1.1	Materials.....	85
5.1.2	Pd Nanoparticle Formation.....	85
5.1.3	<i>In situ</i> Small-Angle X-ray Scattering.....	86
5.1.4	Transmission Electron Microscopy.....	86
5.1.5	Inductively Coupled Plasma.....	87
5.1.6	X-ray Photoelectron Spectroscopy.....	87
5.2	Results and Discussion	88
5.2.1	Pd Precursor Conversion.....	88
5.2.2	Analysis of Pd Nanoparticle Size.....	98
5.2.3	Four-step Particle Growth Mechanism.....	110
5.3	Conclusions	122
6	<i>IN SITU SAXS ANALYSIS OF Pd NANOPARTICLE GROWTH ON TMV1CYS TEMPLATES</i>	124
6.1	Materials and Methods	127
6.1.1	Materials.....	127

6.1.2	Pd Nanoparticle Formation on TMV1cys.....	128
6.1.3	<i>In situ</i> Small-Angle X-ray Scattering.....	128
6.1.4	Transmission Electron Microscopy.....	129
6.2	Results and Discussion	129
6.2.1	Comparison of Pd Nanoparticle Growth in the Presence and Absence of TMV1cys.....	129
6.2.2	Effect of Reaction Parameters on Pd Nanoparticle Growth.....	135
6.2.3	Simulated Effect of Reaction Parameters on Pd Nanoparticle Growth.....	144
6.3	Conclusions	149
7	CONCLUSIONS	150
8	REFERENCES	153

LIST OF FIGURES

1.1	Chimera simulation of TMV1cys.....	3
2.1	X-ray scattering schematic.....	11
2.2	GISAXS schematic diagram, and representative TMV and Pd-TMV scattering images.....	15
2.3	Simulation of SAXS curves of polydisperse spheres.....	19
2.4	SAXS curve of TMV in solution.....	21
2.5	GISAXS curves of TMV1cys and Pd-TMV.....	23
2.6	Typical Guinier fits.....	26
3.1	Schematic diagram depicting TMV1cys assembly on gold chips, and Pd metallization.....	30
3.2	AFM images of tunable TMV1cys surface assembly density.....	37
3.3	AFM images of TMV1cys and Pd nanoparticles formed on TMV1cys...	40
3.4	XPS analysis of TMV chip and Pd-TMV chip.....	41
3.5	GISAXS curves of Pd nanoparticle size controlled using sodium hypophosphite concentration.....	45
3.6	Normalized Pd nanoparticle volume distribution for particles formed in varying sodium hypophosphite concentration.....	48
3.7	GISAXS curves of Pd-TMV chips further reduced with DMAB.....	51
3.8	TEM image of Pd nanoparticles that have been removed from TMV1cys.....	53

3.9	Normalized Pd nanoparticle volume distribution for particles formed using other reducing agents.....	55
4.1	Schematic diagram of <i>in situ</i> GISAXS setup for thermal stability study..	60
4.2	Representative GISAXS images throughout heating for a TMV chip, a Pd-TMV chip with small particles, a Pd-TMV chip with large particles and a Pd-Au chip.....	63
4.3	<i>In situ</i> GISAXS curves for four chip samples throughout heating.....	67
4.4	Plot of normalized intensity vs. temperature at the nanoparticle scattering location.....	73
4.5	AFM images of the chip surfaces after heating.....	77
5.1	Schematic diagram of <i>in situ</i> SAXS setup, and representative <i>in situ</i> SAXS curves for Pd nanoparticle formation in the absence of TMV1cys.....	83
5.2	Plot of invariant (Q) vs. time.....	90
5.3	Plot of maximum invariant vs. Pd precursor concentration.....	94
5.4	Plot of amount of Pd precursor converted to Pd particles.....	98
5.5	Plot of change in particle diameter vs. time.....	100
5.6	Plot of maximum diameter vs. Pd precursor concentration.....	102
5.7	Particle size distributions.....	105
5.8	Representative TEM images of Pd nanoparticles formed in the absence of TMV1cys.....	109
5.9	XPS analysis of Pd nanoparticles formed in the absence of TMV1cys...	113
5.10	Proposed four-step Pd nanoparticle growth mechanism.....	119

6.1	Schematic diagram of <i>in situ</i> SAXS setup, and representative <i>in situ</i> SAXS curves for Pd nanoparticle formation on TMV1cys.....	126
6.2	<i>In situ</i> SAXS curves comparing Pd nanoparticle growth in the presence and absence of TMV1cys.....	131
6.3	SAXS curves of Pd nanoparticle formation on TMV1cys with varying Pd precursor concentration.....	137
6.4	SAXS curves of Pd nanoparticle formation on TMV1cys with varying sodium hypophosphite concentration.....	137
6.5	TEM images of Pd nanoparticles formed on TMV1cys.....	142
6.6	Simulated scattering curves depicting the shift in minima location with increased rod diameter.....	145
6.7	Simulated scattering curves depicting the increase in the number of observable minima with increased Pd coating.....	148

LIST OF TABLES

5.1	Approximate slopes of early conversion, calculated using a linear regression fit for the time range with the greatest change in Invariant in Figure 5.2.....	91
-----	--	----

LIST OF VARIABLES

C_0 :	Constant relating electron density to scattered intensity
C_1 :	Constant relating conversion to initial Pd precursor concentration
C_2 :	Factor relating initial amount of dissolved Pd to scattered intensity
C_3 :	Constant that varies with hypophosphite concentration
d :	Distance between scattering planes, diameter of a particle
$F(q)$:	Scattering from a single particle
ΔH_F :	Latent heat of fusion
$I(q)$:	Scattering intensity
$I_s(q)$:	Scattering intensity from a spherical particle
J_1 :	Bessel function of the first kind
k :	Constant relating conversion to Pd initial precursor concentration
n :	Number density of converted Pd atoms in the form of Pd nanoparticles
$n(r)$:	Number of particles of size, r
N :	Number of particles
$[Pd]_0$:	Initial dissolved Pd precursor concentration
$[Pd]$:	Number of converted Pd atoms in the form of Pd nanoparticles
Q :	Invariant
Q_{max} :	Maximum invariant
q :	Scattering vector (SAXS)
q_{xy} :	Scattering vector (GISAXS)
q_{xy}^* :	Location of nanoparticle scattering feature
\mathbf{r} :	Location of a particle
r :	Radius of a particle
r_c :	Radius of curvature
r_{max} :	Final particle radius
r_{TMV} :	Radius of TMV rod
r_{rod} :	Radius of Pd-TMV rod
R_g :	Radius of gyration of a particle
\mathbf{s} :	Scattered X-ray

\mathbf{s}_0 :	Incident X-ray
T_M :	Melting temperature of a particle
$T_M(\infty)$:	Melting temperature of the bulk
V :	Volume of a single particle
α_i :	Incident angle (GISAXS)
α_j :	Scattering angle in the out-of-plane direction (GISAXS)
2θ :	Scattering angle
λ :	X-ray wavelength
μ :	Chemical potential
μ_0 :	Chemical potential of an infinite sized particle
ρ :	Electron density of a particle
ρ_s :	Density of a particle
$\Delta\rho$:	Electron density contrast of two phases
σ :	Solid-liquid interface energy
ϕ :	Azimuthal angle
Ω :	Atomic volume

LIST OF EQUATIONS

$$2.1 \quad \sin \theta = \frac{\lambda}{2d}$$

$$2.2 \quad I(q) = \left| \sum F(q) e^{-jqx} \right|^2$$

$$2.3 \quad q = \frac{4\pi \sin \theta}{\lambda}$$

$$2.4 \quad \begin{aligned} I(q) &= \left| \sum F(q) \right|^2 \\ &= \int n(r) |F(q, r)|^2 dr \end{aligned}$$

2.5

$$|F(q_{xy})|^2 = I_s(q_{xy}) = \rho^2 V^2 \frac{9(\sin(q_{xy}r) - q_{xy}r \cos(q_{xy}r))^2}{(q_{xy}r)^6}$$

$$2.6 \quad I(q_{xy}) \sim \rho^2 V^2 \exp\left[\frac{-(q_{xy}R_g)^2}{3}\right]$$

$$2.7 \quad I(q) = \int n(r) I_s(q, r) dr$$

$$2.8 \quad I_s(q) = \rho^2 V^2 \frac{9(\sin(qr) - qr \cos(qr))^2}{(qr)^6}$$

$$2.9 \quad Q = \int_{q=q_{\min}}^{q=q_{\max}} I(q) q^2 dq$$

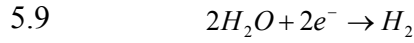
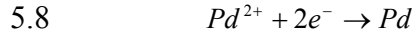
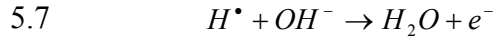
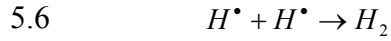
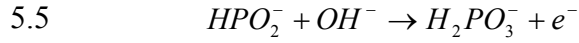
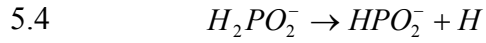
$$4.1 \quad \mu = \mu_o + \frac{2\gamma\Omega}{r_c}$$

$$4.2 \quad \Delta T_M = T_M - T_M(\infty) = \frac{4\sigma T_M}{d\Delta H_F \rho_S}$$

$$5.1 \quad \ln(Q_{\max}) = k \ln([Pd]_0) + C_1$$

$$5.2 \quad Q_{\max} = C_2 \cdot [Pd]_0^k$$

$$5.3 \quad [Pd]_0 = C_3 \cdot r_{\max}^3$$



$$5.11 \quad Q = C_0 (\Delta\rho)^2 NV = C_0 (\Delta\rho)^2 [Pd] / n$$

$$5.12 \quad [Pd] = n[Pd]_0 C_0 C_2 / (\Delta\rho)^2$$

$$5.13 \quad [Pd] = n[Pd]_0 NC_0 / C_3$$

$$5.14 \quad N = C_2 C_3 / (\Delta\rho)^2$$

$$I(q) = 2\pi r_{rod}^2 \frac{J_1(qr_{rod})}{(qr_{rod})}$$

$$6.1$$

$$r_{rod} = r_{TMV} + d$$

1 INTRODUCTION

Transition metal based nanoparticles offer enhanced and unique size-dependent catalytic, electronic and optical properties that arise at the nanoscale. An important example is palladium (Pd) nanoparticles, which play a vital role in catalysis for a wide range of applications in energy,[1-5] chemical synthesis,[6-8] and environmental cleanup.[9, 10] While catalysis is clearly the dominant application of Pd nanoparticles, their electronic properties have also been exploited for nanoelectronic device fabrication[11, 12] and electrochemical sensing applications.[13]

In order to effectively harness these valuable properties, simple routes to controllable Pd nanoparticle fabrication are needed. However, despite the numerous and significant uses of Pd nanoparticles, their controllable and reproducible synthesis remains challenging due to harsh reaction conditions, artifacts from surfactants and capping agents, and often unpredictable particle growth.[14-16] Additionally, in contrast to many other transition metals, fundamental knowledge on the growth mechanism of Pd nanoparticles is lacking, in turn resulting in limited routes for controllable synthesis.

Biologically derived macro/supramolecules (e.g. proteins, DNA and viruses) have gained significant attention as templates for nanoparticle synthesis due to their precise size, structure and shape. In addition, their readily

manipulated surface properties offer enhanced functionality.[17-25] Notably, spherical protein cages have been studied for the templated synthesis of metallic nanoparticles within the cage cores.[26, 27] Filamentous M13 bacteriophage has also been used extensively as a template for the formation of quantum dot or metallic nanowires.[28-30] Another significant example of biological nanotemplates is Tobacco Mosaic Virus (TMV), a rigid rod-shaped plant virus. TMV has been utilized as a nanotemplate in a wide range of applications, such as conductive nanowires, battery electrodes and digital memory devices.[31-34]

Wild-type TMV (wtTMV) is a rigid tubular plant virus, with a length of 300nm and diameter of 18nm, and is comprised of 2130 identical coat proteins, which are helically assembled around a single genomic mRNA strand.[35] Our approach exploits genetically modified TMV (TMV1cys), which possesses one cysteine residue displayed on the outer surface of each coat protein, as shown in the Chimera model drawing of TMV1cys in Figure 1.1.

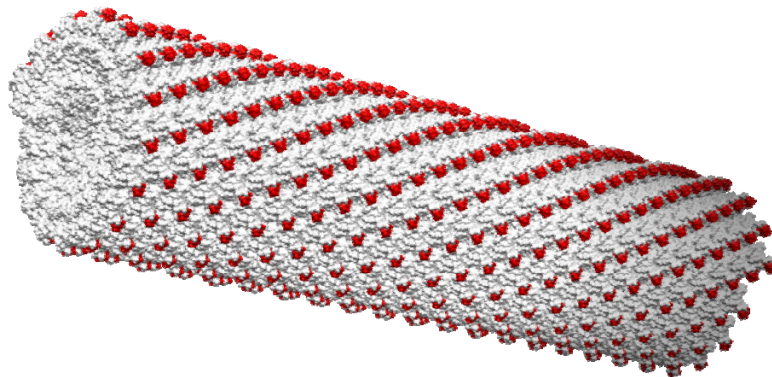


Figure 1.1: Chimera simulation of a portion of TMV1cys. The TMV coat proteins are shown in white, and the inserted cysteine groups are shown as the red balls.

The Chimera drawing of TMV1cys shown in Figure 1.1 was produced using the UCSF Chimera package (<http://www.cgl.ucsf.edu/chimera>) from the Resource for Biocomputing, Visualization and Informatics at the University of California, San Francisco.[36] The TMV structure (PDB ID: 2tmv)[37] was obtained from the Research Collaboratory for Structural Bioinformatics Protein Data Bank (RCSB PDB, <http://www.pdb.org>).[38] *Simulation by Nicholas Horelick.*

Previous studies reported the formation of metal nanoparticles on wt-TMV through electrostatic interactions.[39-41] However, TMV1cys provides a dense and precisely spaced array of thiol functionalities,[42] enabling enhanced[43] and readily controllable Pd nanoparticle formation rising from the sulfur atom's high affinity to Pd.[44, 45] In other studies, the high capacity thiol functionality of TMV1cys and TMV2cys (displaying two surface accessible cysteine residues) has been exploited for the attachment of fluorescent markers and metal nanoparticles.[42, 46-49] Despite these earlier demonstrations of nanoparticle formation on genetically modified TMV's, facile metal nanoparticle size control, as well as any in depth size examination, are lacking in all studies.

Furthermore, the majority of these studies are limited to commonly employed *ex situ* analytical techniques such as Transmission Electron Microscopy (TEM), Scanning Electron Microscopy (SEM) and Atomic Force Microscopy (AFM), which often require sample preparation. Thus *in situ* examinations of the formation of these viral-nanoparticle hybrid entities are severely lacking. Although *in situ* techniques, such as UV-visible Spectroscopy[50] or Dynamic Light Scattering (DLS),[51] have been utilized to gain insight into the growth of metal nanoparticles in a variety of solution based systems, these techniques pose several limitations. For example, UV-visible studies are applicable only to materials possessing surface plasmon resonance, such as gold.[52] Therefore, there is also a critical need for dynamic analyses conducted with simple and

nondestructive *in situ* monitoring methodology that is capable of detecting small changes in these viral-inorganic hybrid materials at the nanoscale.

The Small-Angle X-ray Scattering (SAXS) technique offers several advantages that make it suitable for the *in situ* examination of dynamic changes in complex nanoscale systems. First, it is non-destructive to the sample since the measurement does not involve physical contact like in AFM, or extensive sample preparation procedures such as the coating of thin metals for SEM. Second, the feature size range achieved in SAXS (approximately 1 to 60 nm) is highly applicable for a variety of nanoscale systems. Third, abundant information can be gathered in real-time in a highly programmable manner with a time resolution better than 10 msec with the help of a synchrotron radiation X-ray source and modern detector technologies.[53] SAXS produces statistically meaningful measurements of the average properties of the system by utilizing a sizable sampling area with a large beam size (for example, $\sim 0.5 \times 0.5 \text{ mm}^2$ in our solution studies or $\sim 0.05 \times 5 \text{ mm}^2$ in our surface studies). Most importantly, SAXS techniques have been shown to be a highly accurate method to examine nanoscale features, as compared to TEM.[54, 55] These advantages have made SAXS a powerful tool that has been extensively employed in polymer and material science fields as well as in monitoring the growth of nanoparticles in real time.[56-61] However, the study of dynamic behaviors of viral-inorganic complexes via *in situ* SAXS has remained uninvestigated to date.

1.1 Our Approach

Our approach exploits the high capacity thiol functionality on genetically engineered TMV1cys for the controllable synthesis of palladium (Pd) nanoparticles, and utilizes SAXS to understand the formation of these viral-metal entities. In this thesis, I report the SAXS examination of the chemical reduction of Pd precursor with a mild reducing agent (similar to the common autocatalytic process of “electroless plating”)[62, 63] to form readily controllable Pd nanoparticles on the surface of TMV1cys nanotemplates.

Specifically, we first examine the formation of Pd nanoparticles on surface assembled TMV1cys. In Chapter 3, we show that Pd nanoparticles formed in high density on the TMV1cys templates, and not on the substrate surface. Grazing Incidence Small-Angle X-ray Scattering (GISAXS) showed that Pd nanoparticle size was tunable in a broad size range (4-18nm), simply by controlling the concentration of the mild reducing agent, sodium hypophosphite.[64]

Next, we examined the limitations and dynamic behavior of these viral-nanoparticle structures by conducting a thermal stability study using *in situ* GISAXS. In Chapter 4 we demonstrate that the Pd nanoparticles enhance the thermal stability of the surface assembled TMV templates, and vice versa. We

also show that the degradation of the Pd nanoparticles and TMV templates are coupled.[65]

In order to better control Pd nanoparticle formation on TMV1cys, and understand the role that the TMV templates play in particle formation, we conducted two particle growth studies using *in situ* SAXS. First, in Chapter 5, we examined the growth of Pd nanoparticles in the absence of TMV1cys templates, in order to understand the growth mechanism of particles formed through the electroless reduction of metal precursor. From this study, we learned that the amount of Pd particles converted from Pd precursor increased with increasing Pd precursor concentration. Also, particle size consistently increased with increasing initial Pd precursor concentration. Based on our findings, we propose a four-step particle growth mechanism: (1) Rapid formation of Pd nuclei initiated by the hypophosphite reducer, (2) further growth through conversion of Pd precursor to Pd nanoparticles, (3) slight further particle growth through agglomeration of already formed particles, followed by (4) sedimentation in some cases.

Finally, in order to determine the role that TMV1cys plays in Pd particle growth, we examined the growth of Pd nanoparticles on TMV1cys templates in solution using *in situ* SAXS. The results in Chapter 6 show that Pd particle growth on TMV templates is significantly different than in the absence of the TMV template. We achieved significantly smaller particles on TMV1cys than when formed in the absence of TMV templates, and show that particles

preferentially form on the TMV surface, and not in the bulk solution. Finally, we examined several reaction parameters affecting particle growth, and determined that the coating of Pd particles on the TMV1cys templates was tunable based on Pd precursor concentration.

Combined, the results presented in this thesis demonstrate the facile and readily controllable formation of Pd nanoparticles on TMV1cys nanotemplates. We utilized various SAXS analysis methods in order to elucidate the role of many critical reaction parameters in order to understand the fundamental mechanism of particle formation in this system. As a result, we have created a facile route to reproducible and predictable Pd nanoparticle synthesis on TMV1cys nanotemplates. The results and methodology of this work have already been applied to several catalysis studies,[66-69] and we envision that these results could be further expanded to additional catalysis studies as well as nanodevice fabrication.

2 SMALL-ANGLE X-RAY SCATTERING THEORY

Typically, a variety of *ex situ* analysis techniques are utilized to examine nanoscale features in a wide range of nanosystems. Microscopy methods such as Transmission Electron Microscopy (TEM), Scanning Electron Microscopy (SEM) and Atomic Force Microscopy (AFM) are quite common in nanotechnology, however all are limited due to their *ex situ* nature. Small Angle X-ray Scattering (SAXS) is a measurement technique that is valuable to a wide range of research areas; ranging from nanotechnology, to polymer science, to biology[70]. SAXS is utilized to probe structures on the order of about 1nm or larger in size that are solid or liquid.[71] Unlike microscopy methods, which examine surface detail and local complexities, SAXS examines global parameters resulting in average size, size distribution and average shape measurements.

2.1 General Theory

In SAXS, a sample is irradiated with a high energy monochromatic X-ray beam, and the 2-D scattering image recorded at small angles, 2θ , as shown in Figure 2.1. The 2-D scattering image gives rise to a wide range of information about the size and shape of nanoscale features in the sample as well as their orientation. SAXS differs from X-ray Diffraction (XRD) in that XRD measures the diffraction of X-rays at wide angles (greater than 1°) enabling the measurement of significantly smaller features on the order of inter-atomic distances. Bragg's Law, in Equation 2.1, shows that the scattering feature size, d ,

is inversely proportional to the scattering angle θ , where λ is the wavelength and d is the spacing between scattering planes or nanoparticle size in the case of our experiments.[70]

$$\sin \theta = \frac{\lambda}{2d} \quad (\text{Equation 2.1})$$

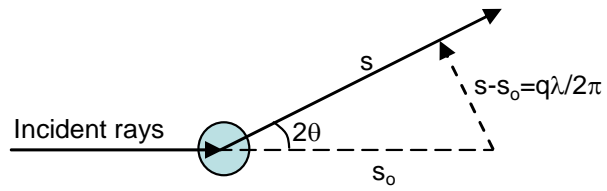


Figure 2.1: X-ray scattering schematic. The sample is irradiated with a high energy X-ray, and the scattered rays, s , are measured as a function of the scattering angle 2θ .

With Wide-Angle X-ray Scattering (WAXS), one can calculate unit cell parameters for a crystalline nanoparticle and could possibly extract the size of the nanoparticle if it is a single crystal from the width of diffraction peaks. When the nanoparticle is polycrystalline, the size determined from the peak width is that of a crystallite within the nanoparticle. On the other hand, as seen from the Bragg equation, SAXS enables the determination of larger features, such as the size of a nanoparticle where the nanoparticle does not need to be crystalline. In typical SAXS, it is assumed that the size of the individual particle of interest is far smaller than the coherent length and size of the X-ray beam. The basic theory of SAXS is identical to that of WAXS, shown in Equation 2.2, where q is the scattering vector (which is related to the scattering angle, 2θ , by Equation 2.3), $I(q)$ is the scattering intensity at q , and the summation is performed for all atoms or particles exposed to the X-ray beam.[70]

$$I(q) = \left| \sum F(q) e^{-jq\mathbf{r}} \right|^2 \quad (\text{Equation 2.2})$$

$$q = \frac{4\pi \sin \theta}{\lambda} \quad (\text{Equation 2.3})$$

In the case of WAXS, $F(q)$ is the atomic scattering factor and \mathbf{r} is the location of an atom. In the case of SAXS, $F(q)$ is the form factor scattering of a single particle and \mathbf{r} is the location of the particle. For dilute particle concentrations, the equation is simplified to Equation 2.4, where $n(r)$ is the size distribution function of nanoscale particles exposed to the X-ray beam.

$$\begin{aligned}
I(q) &= \left| \sum F(q) \right|^2 \\
&= \int n(r) |F(q, r)|^2 dr \quad (\text{Equation 2.4})
\end{aligned}$$

2.2 Grazing Incidence Small-Angle X-ray Scattering (GISAXS)

In this work, we employed Grazing Incidence Small-Angle X-ray Scattering (GISAXS) for analysis of all chip samples, where an X-ray beam was irradiated on the sample at a grazing angle ($\alpha_i=0.1^\circ$), as shown in Figure 2.2(a). GISAXS is the same technique as SAXS (which was utilized for all solution samples), except it is performed with reflection geometry. Samples for GISAXS are typically solid and thus the orientation of the nanoscale objects on the substrate is usually not three-dimensionally randomly oriented. In our case, as shown in Figure 2.2(a), Tobacco Mosaic Virus (TMV) lay down on the gold chip and their cylindrical axes are randomly distributed on the substrate, forming a so-called two-dimensional “powder.” With this reasoning, the GISAXS image is described by Cartesian coordinates (q_{xy}) while the SAXS image is described by polar coordinates (q , and the azimuthal angle ϕ). A typical GISAXS image is recorded as a function of the scattering angle (2θ in the horizontal direction and α_f in the vertical direction) as shown in Figure 2.2(a). The two-dimensional scattering images (shown in Figure 2.2(b,c)) give clear yet qualitative information about the samples such as feature shape and feature size. For example, the shape of the scattering image provides information about the shape of the sample features; where spherical objects produce round isotropic scattering images, and

faceted objects produce winged scattering images because the X-ray is reflected perpendicularly to the facet.[60, 72] Similarly, the “width” of the scattering image, or the broadness of $|F(q)|$, provides qualitative information on the size of the features, where “wider” patterns are produced from smaller sample features. Additionally, the "height" of the scattering image is correlated to the size of the particle in the direction normal to the substrate. Quantitative size and shape analysis of the scattering image is conducted by model-fitting the scattering data.

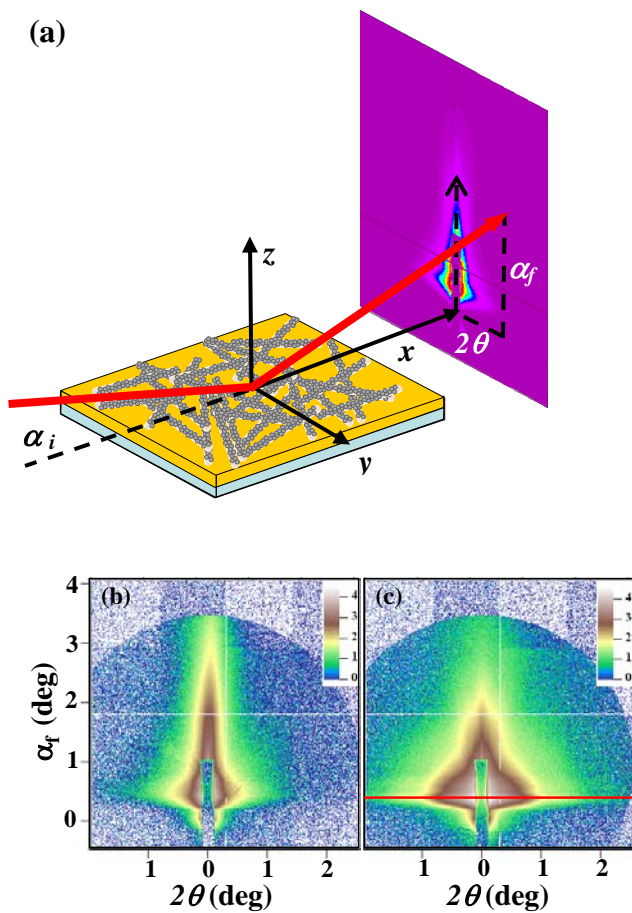


Figure 2.2: (a) Schematic diagram of GISAXS setup. The sample is irradiated at an incident angle α_i , and the scattered rays measured as a function of 2θ and α_f . (b) Typical GISAXS scattering pattern of surface-assembled TMV1cys before metallization (TMV chips). (c) Typical GISAXS scattering pattern of Pd nanoparticles formed on TMV1cys templates (Pd-TMV chips). The red line indicates location of horizontal linecut.

2.2.1 GISAXS Analysis: Pd Nanoparticles vs. TMV

In this work, we examine two different nanoscale objects: one is TMV and the other is Pd nanoparticles. Both TMV and Pd particles contribute scattering in the angular range of GISAXS in this work, however I'll first address analysis of the Pd nanoparticles.

As shown in the schematic diagram of a typical GISAXS setup of Figure 2.2(a), the incident X-ray is irradiated onto the sample at a low angle α_i (0.1°), and the scattering pattern at small angle ranges is recorded on a 2-D CCD detector. Figure 2.2(b) and (c) show typical GISAXS scattering patterns of a TMV chip and a Pd-TMV chip (a TMV chip with Pd nanoparticles), respectively. As shown in Figure 2.2(b), surface assembled TMV1cys exhibits strong scattering in the out of plane (at $2\theta=0$) direction, characteristic of the rod shape of TMV and inter-TMV scattering.⁴⁸ In stark contrast, the pattern shown in Figure 2.2(c) shows strong scattering rising from spherical Pd nanoparticles in a wider area on the CCD detector. The overall scattering intensity emerging from the Pd-TMV chip is significantly increased as compared to that of the TMV chip, due to a substantial amount of highly scattering Pd nanoparticles. Importantly, the out-of-plane scattering from TMV1cys remains strong in Figure 2.2(c), indicating that the Pd nanoparticles are formed right on the TMV1cys templates while the TMV templates maintain the overall tubular structure upon Pd nanoparticle formation. Concurrently, the gold substrate has moderate surface roughness as shown later in the AFM image of Figure 3.4(a) (Section 3.2.2), and generates significant

scattering (at around $0 < \alpha_f < 1$ and $-0.5 < 2\theta < 0.5$). Despite this potential interference, the TMV chips we examined clearly show oscillating scattering patterns characteristic of TMV shown on other substrates.⁴⁸ Further, the clear difference between the scattering patterns in Figure 2.2(b) and (c) shows that this potential background scattering from gold is minimal, and an isotropic feature in the scattering pattern of Figure 2.2(c) clearly signals that Pd particles formed are spherical (above $\alpha_f > \alpha_{f,c}$ ($\sim 0.5^\circ$)). In summary, these clear distinctions in the GISAXS scattering patterns between the TMV chip and the Pd-TMV chip confirms substantial Pd nanoparticle formation on TMV1cys templates, and further suggests the utility of GISAXS.

To interpret the GISAXS images for particle size estimations, a horizontal line-cut is made, as shown by the red line in Figure 2.2(c), and the intensity is plotted as a function of the scattering vector q_{xy} , to create scattering curve plots. First, if we examine a simulated system consisting of nanoparticles of radius r , volume $V(=\frac{4}{3}\pi r^3)$, and electron density of the particle ρ subtracted by that of the surroundings, we obtain $|F(q)|^2$ under the assumption of a spherical particle given in Equation 2.5.[70]

$$|F(q_{xy})|^2 = I_s(q_{xy}) = \rho^2 V^2 \frac{9(\sin(q_{xy}r) - q_{xy}r \cos(q_{xy}r))^2}{(q_{xy}r)^6} \quad (\text{Equation 2.5})$$

This function is a spherical Bessel function and is oscillatory, but the oscillations become damped with increasing polydispersity, and as a result the zeros become smeared out, as shown in Figure 2.3.[55]

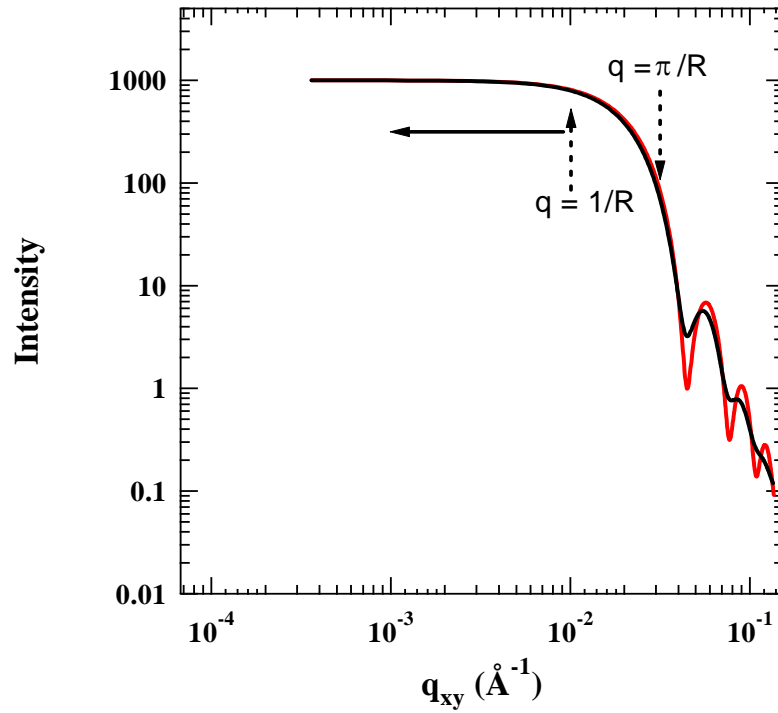


Figure 2.3: Simulation of polydisperse spheres; $R=10\text{nm}$ with 5% (red) and 10% (black) polydispersity. The Schultz distribution function is used for the particle size distribution function. *Simulation by B. Lee.*

In this work, we examine rod shaped TMV, as well as spherical Pd nanoparticles. Typical GISAXS images and analyses of pure TMV on flat substrates have been well-established and are published elsewhere.[73] As shown in Figure 2.4, a scattering curve of monodisperse rod shaped TMV (courtesy of B. Lee), shows a significant number of oscillations due to the highly monodisperse nature of the TMV. The scattering curves of TMV bound to a gold chip shows oscillations that are less pronounced, as shown later in Section 3.2.3, Figure 3.6 These oscillations are damped as a result of the TMV cross section becoming deformed through binding to the gold surface.[73] Further details about GISAXS of TMV deposited on a flat substrate can be found in the literature.[73]

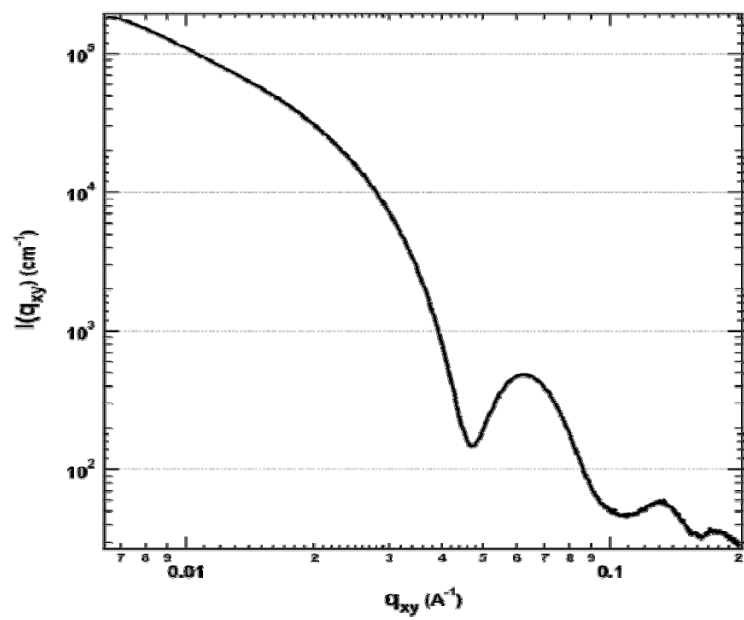


Figure 2.4: Scattering curve of TMV in solution, *measured by B. Lee.*

Next, we examine scattering curves acquired from GISAXS examination of TMV1cys on a gold chip and metallized TMV1cys on a gold chip (Pd-TMV chip). First, the TMV scattering curve (solid line) shows a clear oscillation minimum (denoted by the vertical arrow), which is characteristic of the TMV monodispersity. As described above, the oscillations are damped in this case, due to deformation of the TMV cross section through binding to the gold chip surface. In contrast, the scattering curve of a Pd-TMV chip (dotted line) shows a broad bump-like feature (denoted by the slanted arrow), which is indicative of a polydisperse object; in this case, Pd nanoparticles. This bump feature allows us to deduce valuable information about the nanoparticles, such as average size and size distribution, as described in the next few sections.

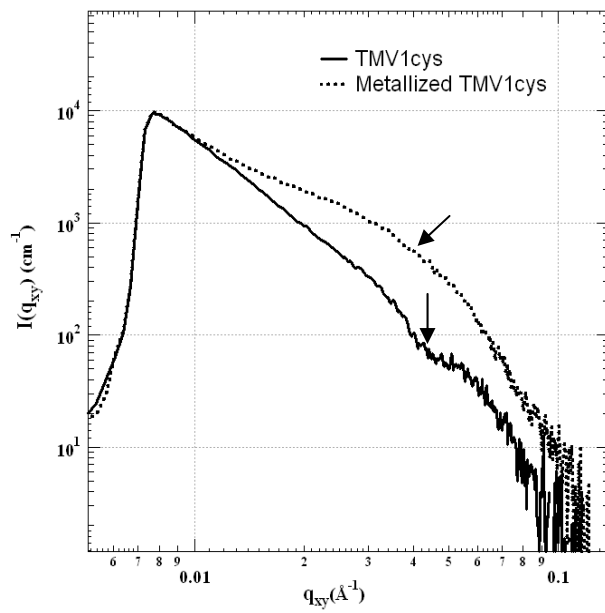


Figure 2.5: GISAXS curves of TMV1cys on a gold chip (solid line) and metallized TMV1cys on a gold chip (Pd-TMV chip) (dotted line).

2.3 Analysis Methods

2.3.1 Guinier Analysis

Dilute polydisperse particle systems exhibit a bump-like feature in a log-log plot of intensity vs. q_{xy} , at $q \sim \pi/r = 2\pi/d$ (d is the average size of the particle) and none or very weak oscillations at $q > \pi/r$ as shown in Figure 2.5. While the model fitting provides $n(r)$, one could apply a rather simple analysis method when only the average size of the particle is of interest. The q region where $q \ll 1/r$ has been called the Guinier region named after A. Guinier.[70] In this region, as long as the average sizes of objects are the same as each other's, the scattering curves of the objects are identical regardless of the shapes of the objects. With the help of a small angle (or small q) approximation, all scattering functions of differently shaped particles are approximated to the Gaussian function form (Equation 2.6), where R_g is the radius of gyration of a nanoparticle.

$$I(q_{xy}) \sim \rho^2 V^2 \exp\left[\frac{-(q_{xy} R_g)^2}{3}\right] \text{ (Equation 2.6)}$$

Therefore, a plot of $\ln[I(q_{xy})]$ vs. q_{xy}^2 results in a linear plot with the slope equaling $-R_g^2/3$. When a particle is a solid sphere, the radius of the particle, r , is related to R_g as $R_g = \sqrt{\frac{3}{5}}r$. [71] The linear portions of the Guinier plot

corresponding to the region where q_{xy} is less than the Guinier knee locations were used in the Guinier analysis to calculate average particle size in this work.

Typical Guinier analysis plots are shown in Figure S1, for three representative Pd nanoparticle samples prepared in 0.5mM Pd precursor and 15mM hypophosphite, 1.5mM Pd precursor and 2.5mM hypophosphite and 5mM Pd precursor and 15mM hypophosphite respectively (Section 5). The q region utilized for the Guinier analysis was selected based on the distinct particle scattering feature (that appears as a bump in a log-log plot of intensity vs. q) observed in the original scattering data.

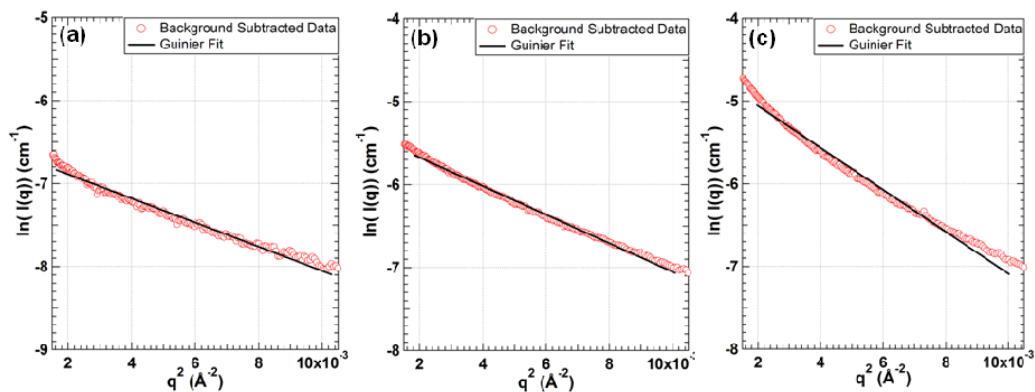


Figure 2.6: Typical Guinier analysis plots. Background subtracted data curves for Pd particles formed in (a) 0.5mM Pd precursor and 15mM hypophosphite, (b) 1.5mM Pd precursor and 2.5mM hypophosphite and (c) 5mM Pd precursor and 15mM hypophosphite are shown as the red markers. Guinier fit in the q region of nanoparticle scattering is shown in black.

2.3.2 Size Distributions

The Guinier analysis can often over-estimate particle diameter since interactions between particles can affect $I(q)$ in the small q range. Thus, an alternative method of estimating particle size is to fit the particle scattering region of the scattering curve using a polydisperse sphere model to create a particle size distribution. In this case, SAXS intensity is described in Equations 2.7 and 2.8 below, where $n(r)$ is the number of particles with radius r , ρ is the electron density of the particle, and V is the particle volume.

$$I(q) = \int n(r)I_s(q,r)dr \quad (\text{Equation 2.7})$$

$$I_s(q) = \rho^2 V^2 \frac{9(\sin(qr) - qr \cos(qr))^2}{(qr)^6} \quad (\text{Equation 2.8})$$

Particle size distributions were calculated using Irena data fitting software, where the scattering curves ($I(q)$ vs. q) were fit using the Maximum Entropy Method with 15% error allowance.[74] The Maximum Entropy Method doesn't require a specific functional form for $n(r)$; only an approximation for a particle shape, which is a sphere in this work. The solution to the data fit is the solution with the largest value of "entropy" which is chosen through an iterative procedure.[75]

2.3.3 Invariant

Invariant (Q), a parameter that represents the overall scattering power of the sample,[71] can be calculated to provide insight into the relative amount of scattering material by integrating the measured intensity, $I(q)$, over the measured q range, as shown in Equation 2.9

$$Q = \int_{q=q_{\min}}^{q=q_{\max}} I(q)q^2 dq \text{ (Equation 2.9)}$$

Theoretically, the Q is proportional to $(\Delta\rho)^2NV$, where N is the number of particles, V is the volume a single particle in the scattering volume, and $\Delta\rho$ is the electron density contrast of the two phases in the system, in this case the solvent and Pd particles.[76] In theory, the intensity $I(q)$ should be measured and integrated from 0 to infinity (strictly speaking, before the wide-angle scattering begins), however, in reality the integration is confined to the detectable q range.

3 PALLADIUM NANOPARTICLE GROWTH ON SURFACE-ASSEMBLED TMV1CYS

In this chapter, we demonstrate readily controllable and tunable Palladium (Pd) nanoparticle formation on surface-assembled TMV1cys nanotemplates. We first examined particle growth in a surface-assembled format for simplicity in order to screen reaction parameters, and to examine particle growth “in house” using Atomic Force Microscopy (AFM). As shown in the schematic diagram of Figure 3.1, we first assembled TMV1cys onto clean gold surfaces by simply dipping a clean gold chip in TMV1cys solution. Following this surface assembly, Pd nanoparticles were synthesized on the TMV1cys surface via reduction of Pd precursor with a mild reducing agent (sodium hypophosphite). Initial examination with AFM showed that surface assembly density of TMV1cys was controllable and tunable, and that Pd nanoparticles were synthesized in high density preferentially on the TMV1cys surface.

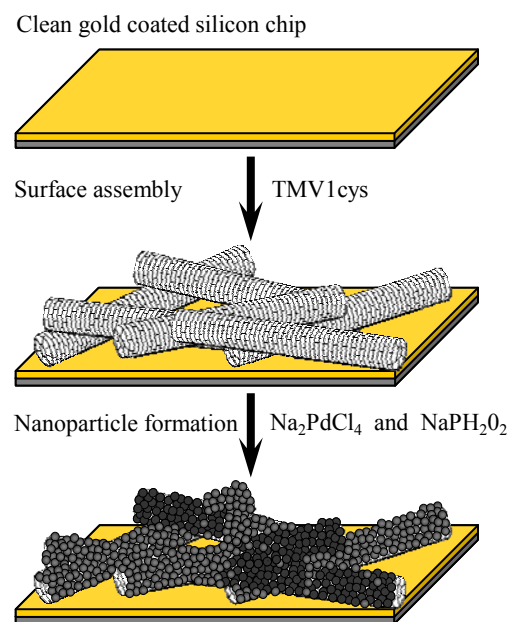


Figure 3.1: Schematic diagram depicting TMV1cys assembly onto gold surfaces, followed by chemical reduction of Pd precursor by sodium hypophosphite to form Pd nanoparticles on the TMV1cys templates.

Further examination with Grazing Incidence Small-Angle X-ray Scattering (GISAXS) indicated that Pd nanoparticle size varied in a broad range and was readily controllable via simple manipulation of sodium hypophosphite reducer concentration. Finally, investigation of other commonly enlisted reducing agents showed a lack of nanoparticle size control and batch-to-batch inconsistency. These results indicate that sodium hypophosphite is an effective reducer for the controllable synthesis of Pd nanoparticles on TMV1cys templates. This study shows, for the first time, an in depth examination of Pd nanoparticle formation on TMV1cys nanotemplates. Further, the results presented in this study indicate facile and broad Pd nanoparticle size manipulation under mild aqueous conditions.[64] Importantly, analysis with GISAXS facilitated the measurement of statistically meaningful and accurate Pd nanoparticle size and size distribution.

3.1 Materials and Methods

3.1.1 Materials

Acetone (HPLC grade), isopropanol and methanol were used as received (all from Fisher Scientific, Waltham, MA). Sodium tetrachloro-palladate (II) (Na_2PdCl_4) was used as the Pd precursor for Pd nanoparticle formation (Sigma-Aldrich, St. Louis, MO). Precursor reduction was conducted using sodium hypophosphite (Sigma-Aldrich), sodium borohydride (Fisher Scientific), sodium

cyanoborohydride (MP Biomedicals, Santa Ana, CA) or Borane Dimethylamine Complex (DMAB) (97%, Sigma-Aldrich). Ethanol (200 proof, 99.5%) was also used (Fisher Scientific).

3.1.2 TMV1cys Surface Assembly

TMV1cys was generously provided by Dr. James Culver at the University of Maryland Biotechnology Institute, Center for Biosystems Research. Gold-coated silicon wafers (Platypus, Madison, WI) were cut into small chips (about 1cm×2cm) and then cleaned sequentially in acetone, isopropanol and methanol each for 20 minutes, with thorough rinsing with deionized water between the steps. After organic solvent cleaning, the chips were dried under a stream of ultrapure nitrogen gas and then etched with plasma (Ernest F. Fullam Inc., Clifton Park, NY). Immediately after etching, the chips were incubated in 100µg/ml TMV1cys in 0.01M sodium phosphate (pH 7) buffer overnight at room temperature. Finally, after TMV1cys binding, the chips were thoroughly rinsed with deionized water, and dried under a stream of ultrapure nitrogen gas, and stored at room temperature until AFM and GISAXS analyses.

3.1.3 Pd Nanoparticle Growth on Surface Assembled TMV1cys

Pd nanoparticles were formed on the TMV1cys templates through the reductive metallization of palladium precursor, Na₂PdCl₄, in aqueous sodium

hypophosphite solutions. TMV1cys bound gold chips (TMV chip) were incubated in 0.5mM Na₂PdCl₄ and sodium hypophosphite solution for 20 minutes, vertically in a micro-centrifuge tube. The metallized TMV chips (TMV-Pd chip) were then thoroughly rinsed in deionized water for five minutes after metallization, and dried under a stream of nitrogen gas.

Pd nanoparticles were also formed on the TMV1cys surface through the reduction of palladium precursor using sodium borohydride, sodium cyanoborohydride and dimethyl-amine borane (DMAB). This reduction was completed in the same manner as with sodium hypophosphite; however in some cases of sodium borohydride and sodium cyanoborohydride, solutions were prepared in both water and 25% aqueous ethanol solution.

3.1.4 Atomic Force Microscopy

Atomic Force Microscopy (AFM) images were acquired using a Dimension 3100 series Scanning Probe Microscope (SPM) (Veeco, Woodbury, NY). Images were analyzed using NanoScope software. All AFM measurements were conducted in tapping mode, with TAP-AI-50 AFM tips (Budget Sensors, Sofia, Bulgaria).

3.1.5 X-ray Photoelectron Spectroscopy

TMV chips and Pd-TMV chips were prepared as described above. Chips were placed under high vacuum and probed using an SSX-100 ESCA X-ray Photoelectric Spectrometer at the Center for Nanoscale Systems (CNS) at Harvard University.

3.1.6 Transmission Electron Microscopy

Pd nanoparticles were formed on TMV chips as described above. To release the particles from the surface, a drop of bleach was placed on the chip, and allowed to sit for two minutes. 5 μ l of solution was then removed from the chip placed on a copper TEM grid (Electron Microscopy Sciences, Hatfield, PA), and allowed to sit for two minutes. The grid was then placed on filter paper to wick away the liquid. TEM samples were probed with a JEOL-2100 High Resolution TEM at the Center for Nanoscale Systems (CNS) at Harvard University.

3.1.7 Grazing Incidence Small-Angle X-ray Scattering

GISAXS measurements were conducted at the Advanced Photon Source (Argonne National Lab, Argonne, IL) BESSRC/XOR 12 ID-C beamline. Samples were mounted on a goniometer, and the beam irradiated on the sample at an incident angle (α_i) of 0.1 $^\circ$, as shown in Figure 2.2(a). The scattered X-rays

were collected on a CCD detector (Rayonix; Mar165), with a sample to detector distance of approximately 2m. Strong scattering and incident beam reflections in the α_f direction were blocked using a vertically mounted beamstop between the sample and detector. The beam energy was 8 keV.

3.2 Results and Discussion

3.2.1 TMV Surface Assembly

As shown in the Atomic Force Microscopy (AFM) images of Figure 3.2, we first demonstrate simple and tunable surface assembly of TMV1cys on gold chip substrates. For this, clean gold-coated silicon chips were incubated in varying concentrations of TMV1cys solution overnight at room temperature. The chips were then thoroughly rinsed with deionized water, dried with stream of ultrapure nitrogen gas, then probed via tapping mode AFM. As clearly shown in Figures 3.2(a) through (d), the surface-assembly density of TMV1cys increased with increasing TMV1cys concentration; ranging from sparse to near-monolayer coverage under the concentration ranges shown. Importantly, the TMV1cys binding on the gold surfaces was highly consistent and stable throughout all of the assembly and probing procedures; including rigorous rinsing, drying, and physical contact with AFM tips, signifying the utility of the genetically displayed thiol functionality. Also, higher surface densities of TMV1cys can be consistently obtained at higher TMV1cys concentrations, while wild-type TMV, (with no

cysteine residues present on the surface), showed inconsistent binding (results not shown). Notably, Royston et al. recently reported a similar trend of TMV1cys binding based on concentration; however they report TMV1cys to be standing at higher TMV1cys concentrations (1mg/ml).[31] The near-monolayer surface coverage of our lateral TMV1cys assembly offers uniform templating conditions for Pd nanoparticle synthesis and allows surface characterization techniques such as GISAXS to be readily employed. As such, TMV-assembled chips with near-monolayer coverage (100µg/ml) were employed for Pd metallization throughout the remainder of the surface assembled TMV studies.

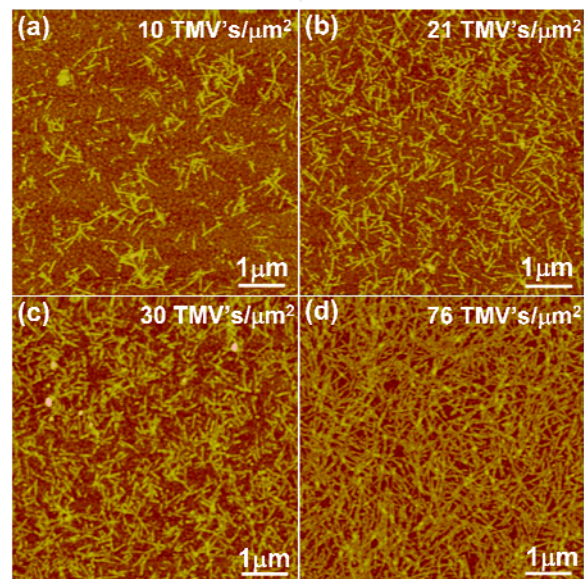


Figure 3.2: AFM images of surface-assembled TMV1cys with varying surface density controlled using TMV1cys incubation concentrations of (a) 10 μg/ml, (b) 30 μg/ml, (c) 50 μg/ml and (d) 100 μg/ml. Scale bar represents 1 μm in all images.

3.2.2 Palladium Nanoparticle Formation on Surface-Assembled TMV1cys

We next demonstrate preferential Pd nanoparticle formation on surface-assembled TMV1cys templates. For this, TMV-assembled chips were incubated in sodium hypophosphite (NaPH_2O_2) solution containing Pd precursor (Na_2PdCl_4). These chips were then thoroughly rinsed, dried with nitrogen gas, and examined using tapping mode AFM as described earlier (Section 3.1). First, Figure 3.3(a) shows a high resolution AFM image of surface assembled TMV1cys before exposure to Pd precursor and reducer. Notably, TMV1cys appears to have a smooth surface while the underlying gold surface shows mildly rough granular curvature. Next, Figure 3.3(b) clearly shows Pd nanoparticles formed on TMV1cys templates along their lengths with high density upon exposure to Pd precursors in reducing agent. Importantly, the number of Pd nanoparticles on the bare gold surface was consistently minimal in the presence of TMV1cys templates, clearly demonstrating preferential templating of Pd nanoparticles on TMV1cys templates. In the absence of TMV1cys, minimal Pd nanoparticle formation was observed on the bare gold surface (data not shown). Also, the metallized TMV (Pd-TMV complex) was highly stable and remained strongly bound throughout extensive rinsing, drying, extended storage under ambient conditions and physical contacts during AFM, unlike previously reported results conducted in aqueous solutions.^[47] Further, another AFM scan of a larger area on a different sample, shown in Figure 3.3(c), clearly shows the consistency of the Pd nanoparticle formation on TMV1cys templates. Combined, these AFM studies

illustrate preferential and high density Pd nanoparticle formation on the surface-assembled TMV1cys templates.

As shown in Figure 3.4, the presence of Pd nanoparticles on the Pd-TMV chip as compared to the TMV chip was confirmed using X-ray Photoelectron Spectroscopy (XPS). TMV chips and Pd-TMV chips were placed under high vacuum and probed using an SSX-100 ESCA X-ray Photoelectric Spectrometer at the Center for Nanoscale Systems (CNS) at Harvard University. First, the bottom XPS curve of the TMV chip (blue) shows strong peaks at 351 and 333 eV, indicating the presence of gold. The upper XPS curve of the Pd-TMV chip (red) shows a strong Pd peak at 338eV, indicating the presence of Pd. Meanwhile, the significant decrease in the gold peak intensity at 351eV for the Pd-TMV chip as compared to the TMV chip strongly suggests a dense coating of Pd on the surface of the chip. While the Pd 3d and Au 4d_{5/2} peaks overlap at about 333eV resulting in the appearance of a slight shoulder, the Pd 3d_{3/2} peak at 338 eV clearly confirms the presence of Pd.

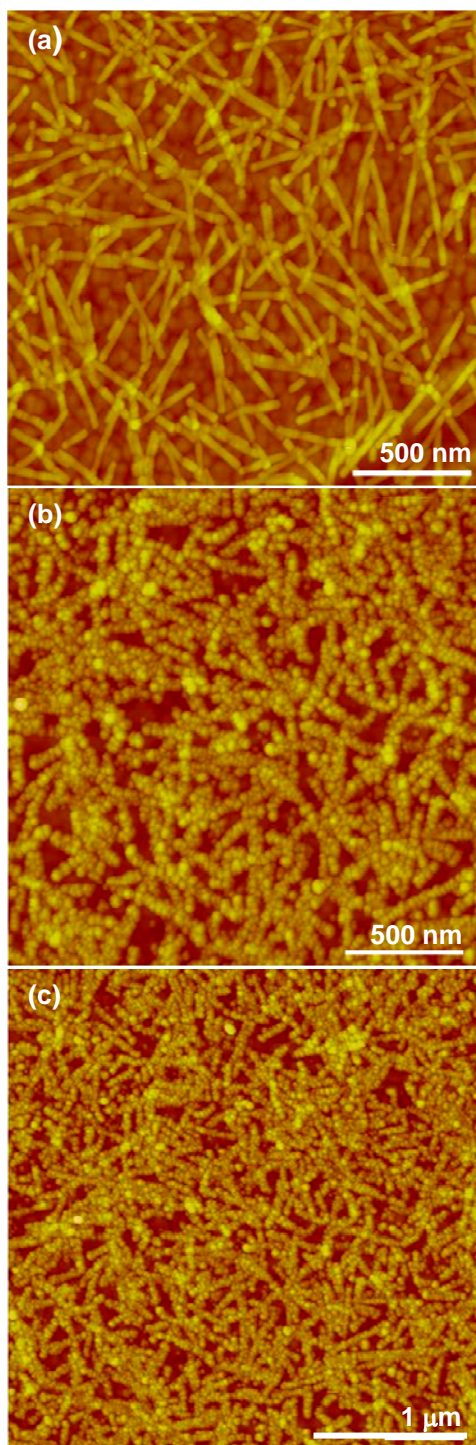


Figure 3.3: Pd nanoparticle formation on TMV1cys templates. (a) AFM image of surface-assembled TMV1cys, bound in 100mg/ml TMV1cys. (b), (c) AFM images of Pd nanoparticles formed on the surface-assembled TMV1cys templates. Pd nanoparticles were formed using 0.5mM Na₂PdCl₄ in 10mM sodium hypophosphate.

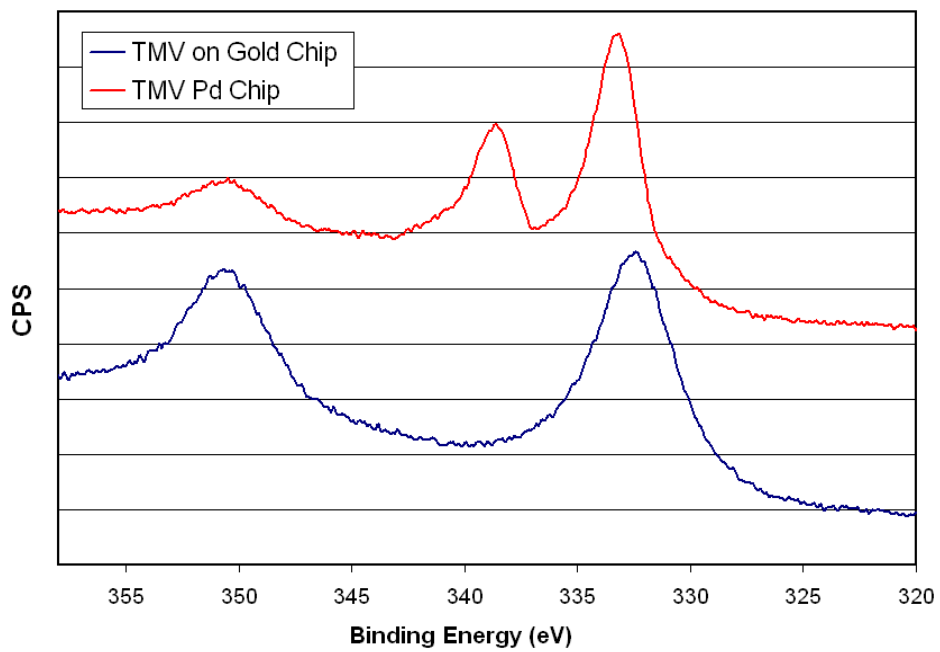


Figure 3.4: X-ray Photoelectron Spectroscopy (XPS) of a TMV chip (blue) and a Pd-TMV chip (red).

3.2.3 Palladium Nanoparticle Size Control using Sodium Hypophosphite

While providing a simple means to probe surface topology at the nanoscale, AFM is not suitable for the accurate examination of particle size or inter-particle distances due to the inherent physical contact between the tip and the sample, resulting in the gross overestimation of particle sizes.[77] Grazing Incidence Small-Angle X-ray Scattering (GISAXS) provides a simple and non-destructive method to calculate nanoscale particle size and size distribution, film thickness, crystal structures, etc.[78] GISAXS measurements of nanoparticle size have been shown to be highly accurate when compared to other common analysis methods, such as High Resolution Transmission Electron Microscopy (HRTEM) and result in statistically meaningful measurements of the average properties of the surface. As shown in the schematic diagram of a typical GISAXS setup in Figure 2.2(a), the incident X-ray is irradiated onto the sample at a low angle α_i (0.1°), and the scattering image at small angle ranges was recorded on a 2-D CCD detector (SAXS Theory, Section 2.2)

To interpret the GISAXS scattering images for particle size estimations, a horizontal line-cut was made as shown by the red line in Figure 2.2(c), and the scattering intensity plotted as a function of the scattering vector q_{xy} ($q_{xy}=4\pi\sin\theta/\lambda$), where θ is the scattering angle (Figure 2.2a) and λ is the X-ray wavelength. The features of these scattering curves were then analyzed using the Guinier law[70], a widely accepted method[78] to calculate particles sizes from

X-ray scattering data, which relates the scattering profile to the particle diameter (SAXS Theory, Section 2.3.1).

Based on the preliminary examinations via AFM, we employed GISAXS to examine several critical reaction parameters that could affect the Pd nanoparticle size, such as Pd precursor concentration, reducer type and concentration, and metallization time. We observed clear distinctions between the scattering curves of samples prepared under various sodium hypophosphite concentrations, indicating that this parameter had the strongest potential as the particle size controlling parameter. Dense surface coverage TMV chips were then incubated in Pd precursor and sodium hypophosphite solutions for 20 minutes, thoroughly washed with deionized water and dried under nitrogen gas, then examined with AFM and GISAXS. Figure 3.5(a) shows scattering curves of Pd-TMV chips prepared in varying concentrations of sodium hypophosphite.

First, the scattering curve of an unmetallized TMV chip (black line) at the bottom of Figure 3.5(a) shows several oscillations at high q_{xy} values (minima shown by black arrows), characteristic of TMV nanotubes[73] whose frequency is observed only when the object is monodisperse in size, and is inversely proportional to the diameter of an object measured (in this case, TMV). Second, the 60mM sodium hypophosphite curve (magenta line) maintains some of these oscillations that are shifted to lower q_{xy} locations with higher frequency. This indicates the presence of small particles (diameter less than 4nm) that evenly coat

the TMV1cys surface while maintaining its monodisperse tubular shape with increased diameter. The presence of nanoparticles is signaled not only by the increase in the frequency of TMV scattering as observed for the 60mM sample, but also by Guinier type scattering (or form factor scattering that could be described by a Gaussian function centered at $q_{xy} = 0$).[71] The width of the Guinier type form factor scattering is inversely proportional to nanoparticle size and parameterized with the q_{xy} value of the Guinier type feature, q_{xy}^* . The Guinier type feature appears as a bump-like feature in a log-log plot of intensity vs. q_{xy} , where the slopes of intensity are different before and after q_{xy}^* . The size of the nanoparticle can be approximated from q_{xy}^* using the Bragg equation, such that $d = 2\pi/q_{xy}^*$:[70] for instance, the location of the bump feature for the 60mM curve is about 0.15\AA^{-1} indicating that the average particle diameter was about 4nm. Next, the Pd-TMV chips with lower sodium hypophosphite concentrations (5-50mM) possess bump features that shift to lower q_{xy} as the sodium hypophosphite concentration decreases, indicating an increase in the particle size. The TMV oscillation features are not visible for these samples, indicating that the scattering from the Pd particles was much stronger than that of the TMV and that Pd particles were becoming polydisperse.

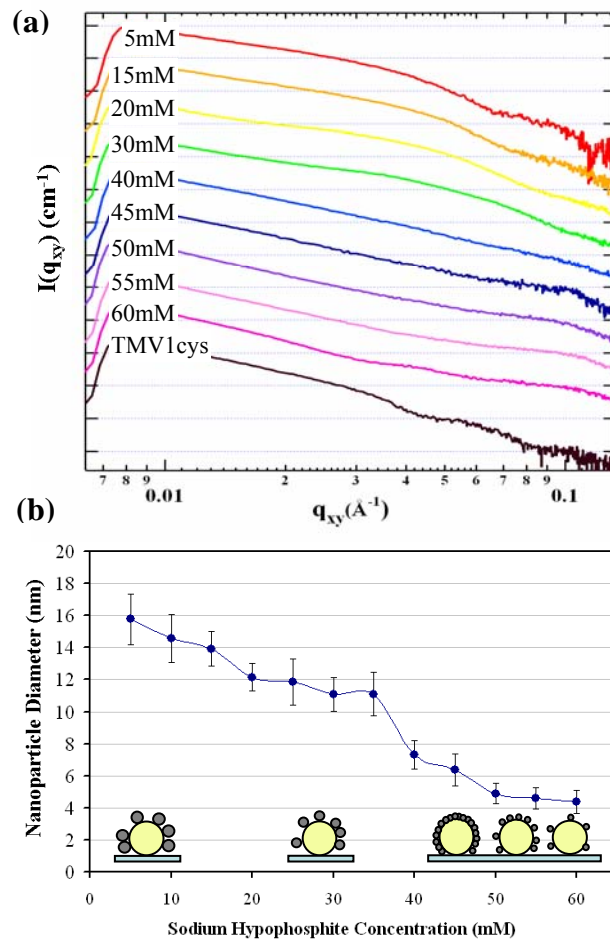


Figure 3.5: (a) Staggered GISAXS curves ($I(q_{xy})$ vs. q_{xy}) of samples prepared 0.5mM Na_2PdCl_4 and varied concentrations of sodium hypophosphite. (b) Average Pd nanoparticle size as a function of sodium hypophosphite concentration, calculated using the Guinier analysis. The error bars represent standard deviations rising from Guinier analyses conducted in ten different linear regions of the Guinier plot for each sample.

In the case of the 60, 55, and 50mM sodium hypophosphite samples, the locations of the bump features shown in Figure 3.5(a) are approximately the same indicating similar particle size, which is further confirmed via Guinier analysis[70] (approximately 4nm in diameter, Figure 3.5(b)). At 45mM sodium hypophosphite (dark blue line in Figure 3.5(a)), the bump feature is slightly shifted to lower q_{xy} indicating slightly larger particles (approximately 6nm in diameter). Importantly, this 45mM sodium hypophosphite sample exhibits a sharper bump feature peak due to scattering between closely packed particles, indicating that the particles were more closely packed than the lower sodium concentration samples. Notably, the particle diameter plot in Figure 3.5(b) shows a sharp increase in particle size from the 45mM to 40mM sodium hypophosphite samples, followed by a steady increase to a maximum diameter of approximately 16nm for the 5mM sodium hypophosphite sample. Importantly, this trend is consistent for several samples prepared on different occasions and batches illustrating the reproducible and robust nature of our TMV1cys assembly, Pd nanoparticle formation and GISAXS-based particle examination strategy. Meanwhile, other parameters studied did not show significant potential as particle size-controlling parameters. Specifically, the effect of incubation time was investigated, where it was observed that the growth of the Pd nanoparticles occurred fast and reached their final size after one minute of incubation (data not shown). Notably, the size range shown here (4-16nm) is significantly broader than in previously reported studies on TMV templates in aqueous conditions such as in S-Y. Lee *et. al.*, where the Pd particles bound to TMV2cys were not uniform

or well-controlled.[47] Also, some of the large (~70nm) particles were not strongly bound on the TMV surface and could be easily washed away, in contrast to particles presented in this study which were strongly bound to TMV templates. Additionally, Knez *et al.* previously reported significantly smaller Pd particles formed on wild-type TMV in aqueous solutions.[41] In contrast, Pd particles we report in this study show a significantly different and broad range of sizes (4-16nm) on surface-assembled TMV1cys templates, further suggesting the uniqueness and utility of our TMV1cys surface assembly strategy for facile size control via modulation of simple parameters such as the reducing agent concentration.

Next, to further understand the size distribution of the Pd nanoparticles measured in Figure 3.5(a) and (b), we employed Irena data fitting software and plotted normalized Pd particle volume distributions, as shown in Figure 3.6.[74] The Irena software utilized for size distribution fittings uses the Maximum Entropy Method and 15% error allowance (SAXS Theory, Section 2.3.2). As shown in Figure 3.6, the Pd nanoparticles are more uniform at small sizes (thus high sodium hypophosphite concentrations), and became polydisperse as the average size increased.

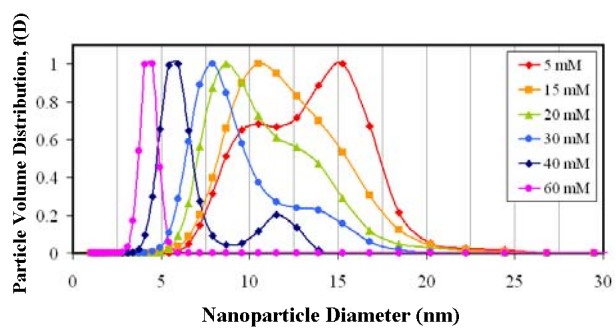


Figure 3.6: Normalized Pd nanoparticle volume distributions under various sodium hypophosphite concentration.

In summary, results in Figures 3.5 and 3.6 show a wide range of Pd nanoparticle sizes (4-16nm) formed on surface-assembled TMV1cys templates under mild aqueous environments with a clear relationship between the size and the reducer concentration as a key size-controlling parameter.

Further reduction of the Pd nanoparticles with dimethylamine borane complex (DMAB) did not change the nanoparticle size, as shown in the GISAXS curves in Figure 3.7, where five samples prepared in identical preparation conditions were further reduced in varied concentrations of DMAB. More importantly, the five identical samples that exhibit identical scattering curves, and confirm the reproducibility and consistency of our nanoparticle formation method and GISAXS measurements.

Five Pd-TMV chips prepared with 0.5mM Pd precursor and 30mM sodium hypophosphite were then exposed to varied concentrations of DMAB for three minutes to further reduce the Pd nanoparticles. The GISAXS scattering curves for all samples exhibit a distinct bump feature at $q_{xy}=0.04 \text{ \AA}^{-1}$ indicating that Pd nanoparticles were the same size for all samples. This result shows that further reduction with DMAB does not affect Pd nanoparticle size, since all nanoparticle sizes remain the same as the samples not exposed to DMAB. Importantly, this result further demonstrates that our TMV-templated approach for Pd nanoparticle formation is highly reproducible as all samples show nearly identical scattering curves. Additionally, all of the scattering curves in Figure 3.7

correlate well with the 30mM curve shown in Figure 3.5(a) (samples in Figure 3.8 were prepared and measured months apart from samples in Figure 3.5(a)). Based on this GISAXS result, it is clear that our viral-templated approach for tunable Pd nanoparticle formation is highly reproducible and reliable.

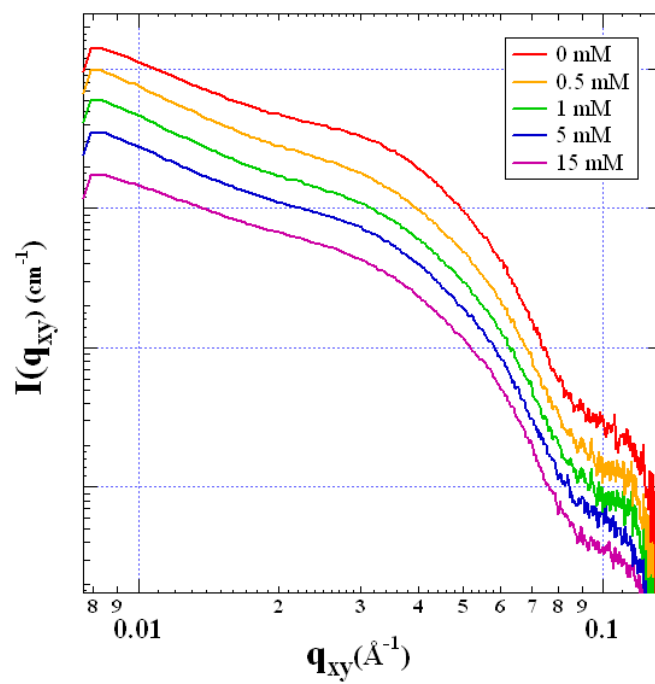


Figure 3.7: Staggered GISAXS curves of Pd-TMV chips prepared in identical conditions, then further reduced with varied concentrations of DMAB.

As shown in Figure 3.8 Pd nanoparticle size was confirmed using Transmission Electron Microscopy (TEM). For this, Pd nanoparticles were formed on surface-assembled TMV1cys nanotemplates (as described in Materials and Methods, Section 3.1) using 30mM sodium hypophosphite, then the TMV1cys templates were dissolved by placing a drop of bleach on the Pd-TMV chip. Next, 10 μ l of the bleach droplet containing the released Pd nanoparticles was placed on the TEM grid and allowed to sit for two minutes before placing the grid on filter paper to wick away the liquid. As shown in the TEM image of Figure 3.8, the Pd nanoparticles were spherical, which further confirms the validity of the isotropic scattering pattern observed with GISAXS (Figure 2.2(c)) that indicated spherical particles. The nanoparticle sizes were measured, and the size distribution reported in Figure 3.8(inset). This size distribution correlates well with the GISAXS size distribution results shown in Figure 3.6 with most nanoparticles in the 6-9nm diameter range. Importantly, Figure 3.8 also shows that the Pd nanoparticles aggregated in the absence of the TMV1cys nanotemplate. In summary, this result clearly validates the accuracy of the GISAXS measurement method and size distribution simulations in Figures 3.5 and 3.6.

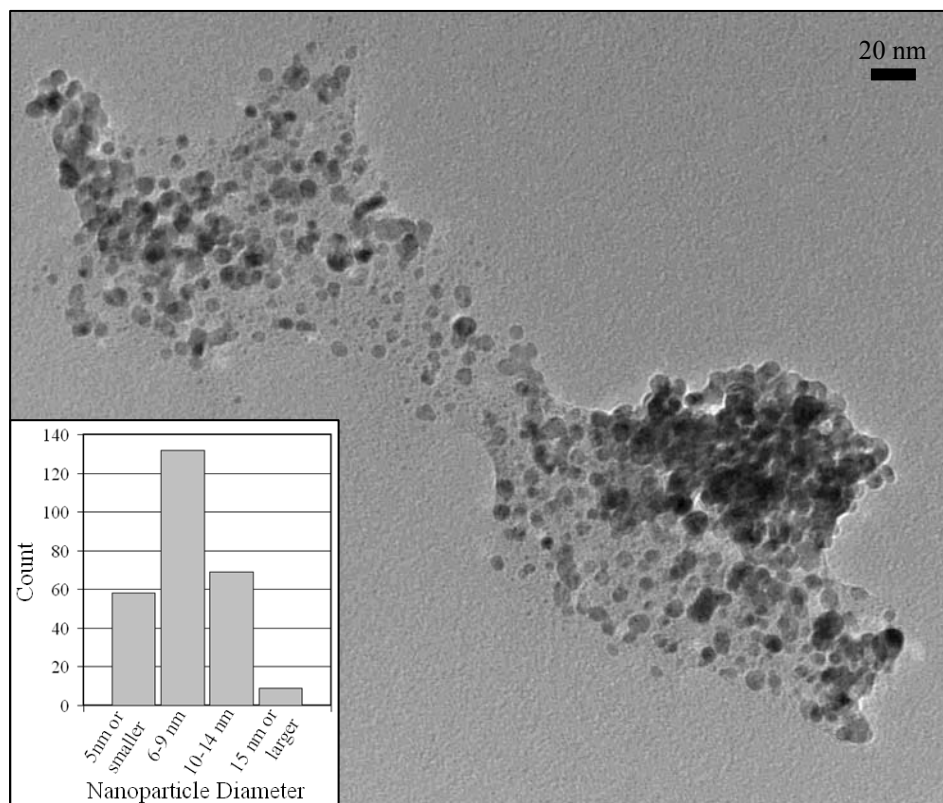


Figure 3.8: Transmission Electron Microscopy (TEM) image of Pd nanoparticles.
Inset: Pd nanoparticle diameter distribution.

Building on the observation that sodium hypophosphite concentration plays a significant role in Pd nanoparticle size control, we further investigated the effects of other commonly enlisted reducing agents; dimethylamine borane complex (DMAB), sodium cyanoborohydride, and sodium borohydride.[79, 80] For this, TMV-chips were incubated in aqueous or 25% ethanol solutions containing the Pd precursor and reducing agents, and examined with AFM and GISAXS. Their normalized volume distributions were calculated via Irena software in the same manner as described above. Several representative size distribution curves for each set of reducing environments that produced meaningful nanoparticles are plotted in Figure 3.9.

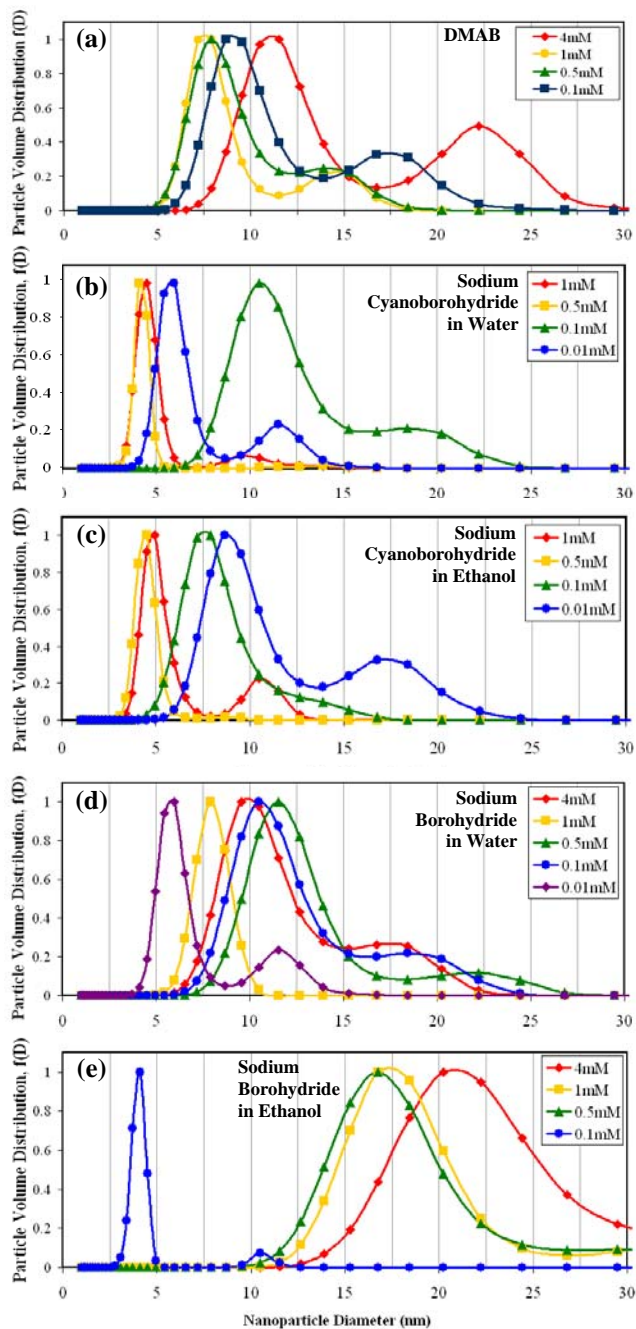


Figure 3.9: Normalized Pd nanoparticle volume distributions for Pd nanoparticles formed through the reduction of 0.5mM Na_2PdCl_4 using (a) DMAB, (b) sodium cyanoborohydride in water, (c) sodium cyanoborohydride in 25% ethanol, (d) sodium borohydride in water, and (e) sodium borohydride in 25% ethanol..

First, in Figure 3.9(a), aqueous DMAB solution resulted in particles ranging from 5 to 15 nm average diameter, with some larger particles (15-20 nm) present. Importantly, the size distributions were broad throughout the concentration ranges studied, with no apparent concentration-size relationship. Second, Figure 3.9(b) shows that reduction with sodium cyanoborohydride in aqueous conditions resulted in narrow size distributions (4-6nm diameter) for the two highest reducer concentrations tested (1mM and 0.5mM). Similarly, the lowest reducer concentration tested (0.01mM) also resulted in small nanoparticles with a narrow size distribution. In contrast, at 0.1mM reducer concentration, larger and more polydisperse particles were observed (8-20 nm). Third, Figure 3.9(c) shows similar particle sizes (4-6 nm) at the higher concentrations of sodium cyanoborohydride in 25% ethanol as in the aqueous condition. Next, Figure 3.9(d) shows that aqueous sodium borohydride produced broad particle size ranges. The size distribution was quite narrow in the case of 1mM and 0.01mM sodium borohydride, however the particle size became highly polydisperse at 0.1mM, with no apparent concentration-size relationship. Finally, Figure 3.9(e) shows that sodium borohydride in 25% ethanol results in highly narrow size distributions at 0.1mM, with 4nm average particle diameter. At higher concentrations, Pd nanoparticles became highly polydisperse and quite large (12-30nm). Again, there is no clear concentration-size relationship.

In general, the three reducing agents studied here often exhibited polydisperse particle sizes with no apparent concentration-size relationship. In

stark contrast to the reproducible and broad (4-16nm) size ranges for sodium hypophosphite, these reducing agents did not produce meaningful size ranges, and there was high batch-to-batch inconsistency. Further, other reducer concentrations studied (e.g. greater than 4mM) did not show any meaningful Pd particle formation via either AFM or GISAXS (data not shown). Nevertheless, all the reducing conditions studied here (cyanoborohydride, borohydride and DMAB) show several important aspects that are consistent with the sodium hypophosphite case. First, both AFM images and GISAXS scattering patterns clearly show preferential Pd nanoparticle formation on TMV templates. Second, GISAXS results show that TMV templates retained their tubular structures upon metallization in all conditions examined. Finally, in all cases, Pd nanoparticles formed on TMV templates (thereby the Pd-TMV complexes on the surface) retained their overall structures through extensive rinsing, drying with nitrogen gas stream, extended storage, tapping mode AFM and GISAXS, indicating the stability of the Pd-TMV complexes and TMV templates under various reducing and physical environments. In summary, the three buffers studied here (Figure 3.9) produced inconsistent, unreproducible and polydisperse particles whereas sodium hypophosphite (Figure 3.5 and 3.6) yielded easily controlled, consistent and broad size ranges.

3.3 Conclusions

The results in this chapter demonstrate the readily controllable formation of uniform Pd nanoparticles on the surface of genetically modified TMV1cys templates via electroless deposition of Pd precursor simply by modulating the concentration of the mild reducing agent, sodium hypophosphite. Both AFM- and GISAXS-based examinations clearly showed spherical Pd nanoparticle formation preferentially on TMV1cys templates in high density. In depth Guinier analyses further indicated that the Pd nanoparticles were consistently and controllably formed in a broad size range (4-16nm diameter) using sodium hypophosphite as the controlling parameter. Stronger reducing agents resulted in inconsistent Pd particle growth. We believe that our viral templated nanoparticle formation approach employing simple dipping procedures throughout, coupled with the first-time in depth particle size examination via GISAXS, represents a significant advancement toward controlled metal nanoparticle formation.

4 THERMAL STABILITY OF SURFACE-ASSEMBLED Pd-TMV COMPLEXES

The applications of these Pd-TMV nanostructures are far reaching; ranging from nanoelectronic applications to catalysis. To better understand the limitations of these nanostructures, and their dynamic behavior when exposed to external stressors, we examined the thermal stability of the Pd-TMV complexes using *in situ* GISAXS. Specifically, we examined the scattering patterns of four different complex types during heating; TMV1cys on a gold chip (TMV chip), Pd nanoparticles on a gold chip (Pd-Au chip), TMV1cys with large Pd nanoparticles, and TMV1cys with small Pd nanoparticles (Pd-TMV chips) all assembled on gold chip substrates. As shown in Figure 3.2 and 3.3, we first assembled TMV1cys onto clean gold surfaces, then synthesized large or small Pd nanoparticles on the TMV1cys template surface via reduction of Pd precursor with a mild reducing agent (sodium hypophosphite). The samples were heated in a sample cell purged with Helium gas and their scattering images measured throughout the course of heating via *in situ* GISAXS, as shown in the schematic diagram of Figure 4.1.[65]

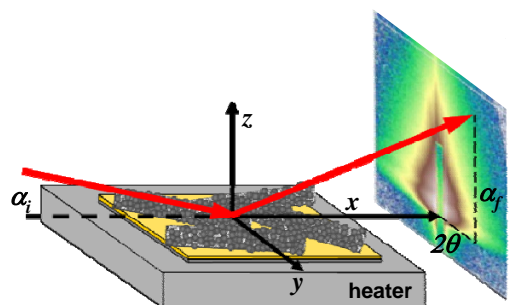


Figure 4.1: Schematic diagram of thermal stability examination via *in situ* GISAXS. The chip sample is irradiated at an incident angle α_i , and the scattered rays measured as a function of 2θ and α_f .

4.1 Materials and Methods

4.1.1 Materials

Acetone (HPLC grade), isopropanol and methanol were used as received (all from Fisher Scientific, Waltham, MA). Sodium tetrachloro-palladate (II) (Na_2PdCl_4) was used as the Pd precursor for Pd nanoparticle formation (Sigma-Aldrich, St. Louis, MO). Precursor reduction was conducted using sodium hypophosphite (Sigma-Aldrich)

4.1.2 Sample Preparation

All Pd-TMV chip samples were prepared as described previously in Sections 3.1.2 and 3.1.3.

4.1.3 *In situ* Grazing Incidence Small-Angle X-ray Scattering

GISAXS measurements were conducted at the Advanced Photon Source (Argonne National Lab, Argonne, IL) BESSRC/XOR 12 ID-C beamline. Samples were mounted in a homemade portable cubic chamber equipped with a boron nitride heater and two window ports transparent to the X-ray beam. The sample cell was purged with Helium gas to a pressure of 800 torr, and the sample heated from room temperature to 300°C at a rate of 5°C/min using a LakeShore 340 temperature controller (LakeShore, Westerville, OH). The beam was irradiated on the sample at an incident angle (α_i) of 0.2° for the pure TMV sample

and 0.1° for all other samples, as shown in Figure 4.1 The scattered X-rays were measured every 20°C , and collected on a CCD detector (Rayonix; Mar165), with a sample to detector distance of approximately 2 meters. Strong scattering and incident beam reflections in the α_f direction were blocked using a vertically mounted beamstop between the sample and detector. The beam energy was 12 keV.

4.2 Results and Discussion

4.2.1 Analysis of GISAXS Images

As shown in Figure 4.2, we first show the suitability of the *in situ* GISAXS technique for investigation of the thermal stability of the Pd-TMV complexes. For this, we examined the four chip samples by placing each on a heater and recording their GISAXS images throughout heating ($5^\circ\text{C}/\text{min}$). Figure 4.2 shows representative scattering images at the start of heating, at the temperature where the most drastic change in the image starts to occur, and at the end of heating.

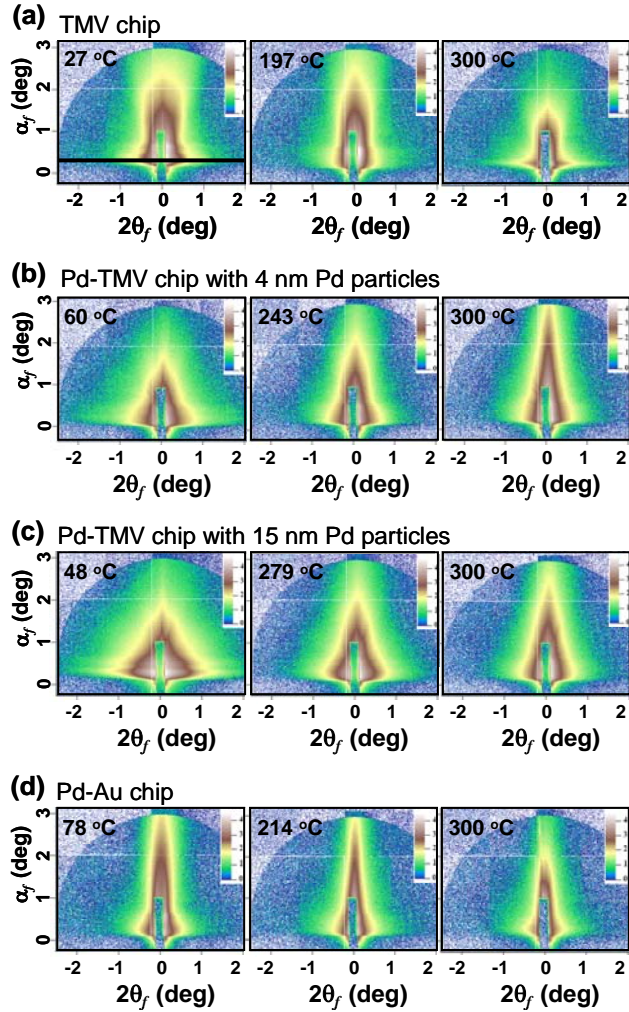


Figure 4.2: Representative GISAXS images of intensity as a function of scattering angle initially, at the temperature of greatest change and at the end of heating for: (a) a TMV chip, (b) a Pd-TMV chip with 4nm Pd particles, (c) a Pd-TMV chip with 15nm Pd particles, and (d) a Pd-Au chip.

First, Figure 4.2(a) shows GISAXS images of a TMV chip throughout heating. Initially, the TMV scattering image shows strong scattering in the vertical (q_y) direction, which is characteristic of TMV. As heating progresses, the two-dimensional scattering image shape became narrower and the overall intensity decreased. Next, Figure 4.2(b) shows representative scattering images of a Pd-TMV chip with small (4nm) particles. At low temperature, the scattering image shows strong isotropic scattering in the horizontal direction rising from the spherical nanoparticles, as well as vertical scattering resulting from the TMV. Throughout heating, the shape of the scattering image became narrower and the intensity continued to decrease. Figure 4.2(c) shows scattering images of a Pd-TMV chip with large (15nm) particles. Similar to the small particle chip shown in Figure 4.2(b), the Pd-TMV chip with large particles initially showed strong horizontal scattering from the spherical nanoparticles, with the scattering image shape becoming narrower as heating progressed. Finally, Figure 4.2(d) shows scattering images of a Pd-Au chip, where the initial scattering image showed a narrow scattering shape that became narrower and decreased in intensity as heating progressed.

Upon closer examination, the overall intensity of the scattering images decreased for each sample over the course of heating, indicating that the scattering objects in the measurable size range of GISAXS (less than 60nm in this experiment, $d_{max} = 2\pi/q_{min}$) decreased. For the TMV sample, the decrease in intensity rises from the destruction of the TMV's on the chip surface. In the case

of Pd nanoparticle scattering, the width in the horizontal direction of the scattering image shape generally indicates the size of the nanoparticles, where narrower scattering indicates larger nanoparticles (Small Angle X-ray Scattering Theory Section). Initially, the Pd-TMV samples were highest in scattering intensity, as compared to the Pd-Au sample, indicating that there were substantially more Pd nanoparticles present on the Pd-TMV chip than the Pd-Au chip. As heating progressed, the scattering image shapes became narrower, indicating that the nanoparticles agglomerated and increased in size. At the end of heating, the shapes of the scattering images were highly narrow with an overall decrease in intensity, indicating that the agglomerated Pd nanoparticles were too large to be measured by GISAXS. In summary, these clear changes in the scattering images throughout the heating experiments demonstrate the applicability of *in situ* GISAXS to measuring the changes in the viral-nanoparticle complexes.

4.2.2 Analysis of Scattering Curves

While the changes in the GISAXS images in Figure 4.2 give clear qualitative information on the changes in the system, an in depth analysis using scattering curves acquired from those scattering images provides extensive quantitative information, as shown in Figure 4.3. For this, scattering curve plots were created by making horizontal line-cuts (shown by the black line in Figure 4.2(a)) of all scattering images and plotting intensity as a function of the scattering vector q_{xy} ($q_{xy}=4\pi\sin\theta/\lambda$). Specifically, Figures 4.3(a) to (d) show

overlays of scattering curves from four chip samples throughout heating, allowing us to determine the specific temperature where the scattering pattern undergoes substantial changes, which indicates the onset of major scattering species' destruction.

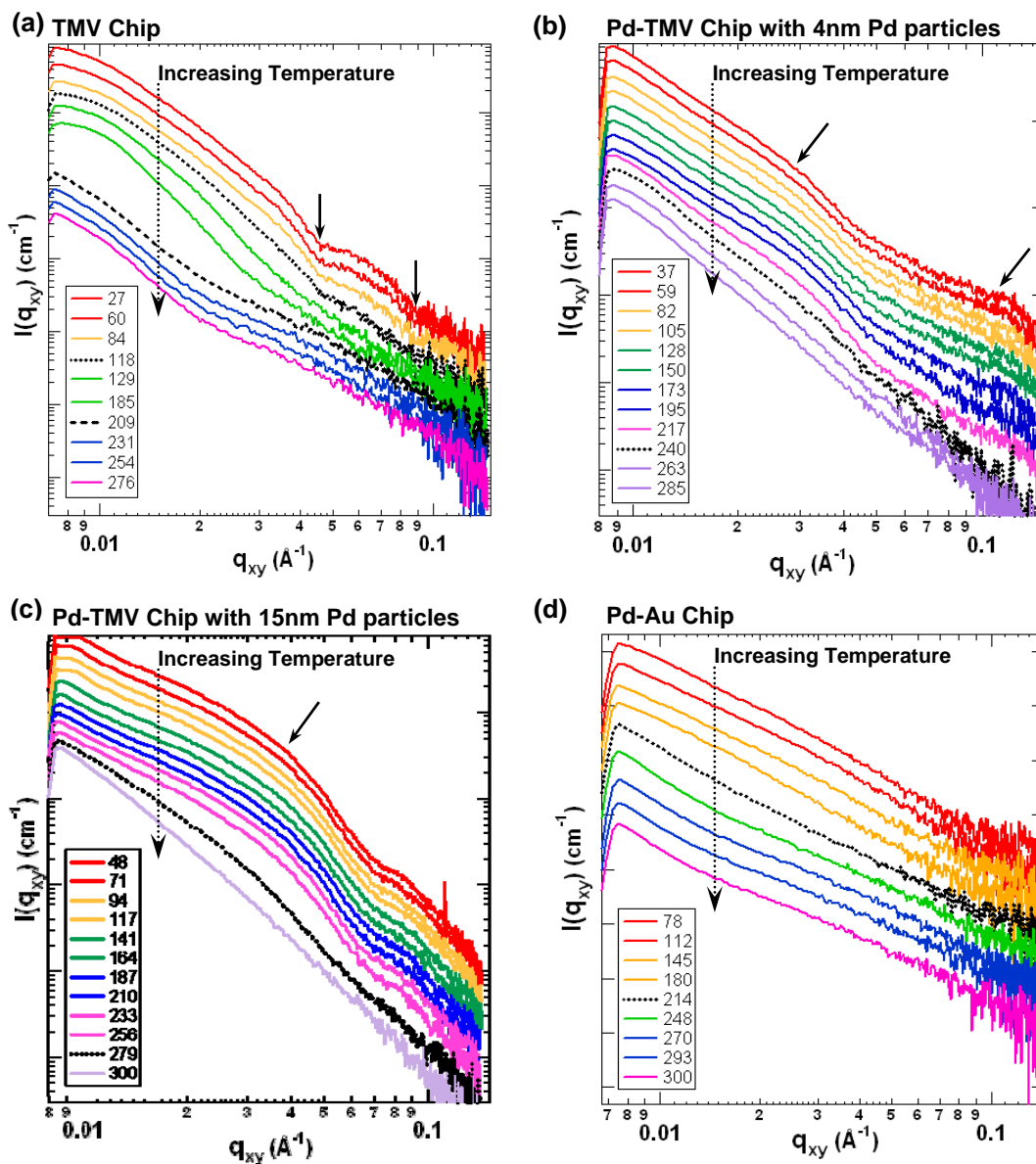


Figure 4.3: Staggered log-log scattering curves of intensity vs. the scattering vector q_{xy} for (a) a TMV chip, (b) a Pd-TMV chip with small (4nm) Pd nanoparticles, (c) a Pd-TMV chip with large (15nm) Pd nanoparticles and (d) a Pd-Au chip.

First, the scattering curves of a TMV chip are shown in Figure 4.3(a). The initial scattering curve of TMV (top red line) shows oscillations at high q_{xy} values (two of the minima are indicated by arrows), characteristic of monodisperse TMV nanotubes.[73] Importantly, these oscillations are observed only when the objects are monodisperse in size, where the oscillation frequency is inversely proportional to the diameter of the object measured (see Small Angle X-ray Scattering Theory section).[70] As heating reached 118°C (black dotted line), the oscillations from the TMV monodispersity were no longer present, however the general curve shape remained the same. This indicates that the TMV tubes were damaged, resulting in TMV cross sections that were not monodisperse, yet the average size of the TMVs remained the same. At 129°C, the curve shape was changed to show a significant signal at even lower q_{xy} , with no oscillations present. The lack of oscillations suggests that the TMVs lost their short distance structure completely, while the increased signal at lower q_{xy} indicates the division of the long tubular shape to shorter pieces. The scattering curve shape changed significantly at 209°C (black dashed line), with the scattering at low q_{xy} decreased, indicating that the TMV nanotubular structure was completely destroyed. TMV is a multi-protein structure, assembled via non-covalent interactions among the protein subunits and with the genomic RNA.[35] While the thermal decomposition of individual covalent chemical linkages may occur at various temperatures,[81-83] we note that these observations via GISAXS represent “structural” changes by the scattering species, which does not appear to occur up to 118°C.

Next, Figure 4.3(b) shows scattering curves of a Pd-TMV chip with small Pd nanoparticles. The bump-like scattering features (indicated by two arrows) in the top curve in the log-log plot of intensity vs. q_{xy} in Figure 4.3(b) demonstrate the presence of both TMV and Pd nanoparticles. The bump-like scattering at $q_{xy}=0.13 \text{ \AA}^{-1}$ is the characteristic scattering feature of polydisperse objects, indicating 4nm Pd nanoparticles. The bump feature at $q_{xy}=0.03 \text{ \AA}^{-1}$, arises from TMV, where the presence of this feature indicates evenly coated nanoparticles on TMV forming a metallic shell. The TMV scattering feature at low q_{xy} is comparable to the initial TMV curve in Figure 4.3(a); however the difference is apparent at high q_{xy} where nanoparticle scattering dominates and the characteristic TMV oscillations are no longer visible. The important difference between TMV and the Pd-TMV complex is its thermal behavior as heating progresses. There was no significant change in scattering from the cross-section of the Pd-TMV complex, which was observed at low q_{xy} , up to 217°C; substantially higher than the temperature where the pure TMV structure began to degrade. The Pd nanoparticle scattering at high q_{xy} also did not change significantly up to 217°C. At 240°C (black dashed line), both signals from the cross-section of the complex and nanoparticles disappear and the scattering curve resembled a straight line in the log-log plot. This straight line represents typical Porod scattering of polydisperse particles that are larger than the detection limit, which is 60nm in this work.[71] Additionally, further Guinier analysis shows that nanoparticle diameter was constant up to 240°C (dotted line) when the scattering image changed significantly, and the overall structure of the Pd-TMV complex changed

drastically (data not shown). Importantly, the disappearance of the TMV feature and the nanoparticle feature occurred at roughly the same temperature, possibly indicating that nanoparticle agglomeration is coupled with TMV structure degradation.

Next, Figure 4.3(c) shows GISAXS scattering curves for a Pd-TMV chip with large Pd nanoparticles. Initially, the scattering curve (top red line) showed a bump at $q_{xy}=0.04 \text{ \AA}^{-1}$ (indicated by an arrow), corresponding to 15 nm diameter particles[64] (See Chapter 2 and Chapter 3). Scattering from the cross-section of the Pd-TMV complex was not observable for this sample because nanoparticle scattering dominated and the TMV scattering features were not observable. This indicated that Pd nanoparticles that were as large as the cross-section of TMV were randomly located on the TMV surface, and that their distribution did not appear to form a homogeneous shell shape. If the nanoparticles were forming a homogeneous shell on TMV, characteristic TMV scattering features, such as oscillations, would be observable.[64] The shapes of the scattering curves measured throughout heating did not change at all until 279°C, indicating that 15 nm particles were present until this temperature. Above 279°C, the signal was no longer present indicating that the 15 nm particles had agglomerated to a size larger than was measurable with this GISAXS setup. Importantly, further Guinier analysis showed that the change in nanoparticle diameter was negligible up to 279°C (dotted line) when the major change in the scattering pattern, and therefore overall structure and particle size, began (data not shown).

Finally, Figure 4.3(d) shows scattering curves of Pd nanoparticles formed on gold chips in the absence of TMV. The first scattering curve (top red line) showed a very broad bump at approximately $q_{xy}=0.03 \text{ \AA}^{-1}$ indicating large and polydisperse nanoparticles. As heating progressed, the bump feature shifted to lower q_{xy} , indicating growth of the nanoparticles. By 214°C (dotted black line), the bump feature had disappeared, indicating that the Pd nanoparticles had grown outside the measureable range.

It is clear from the scattering curves in Figure 4.3 that the TMV structure degrades at a significantly lower temperature than the structure of the Pd-TMV complex. We also observe that the larger nanoparticles formed on TMV are more thermally stable than the smaller particles. Additionally, the Pd particles formed on the gold surface are larger and more polydisperse than both samples of TMV-templated particles, but agglomerate at a lower temperature (214°C) than the TMV templated particles (240°C and 279°C for small and large particles respectively), suggesting that the nanoparticle stability is enhanced by TMV. In summary, the GISAXS analysis using scattering curves in Figure 4.3 shows that we are able to pin-point the specific temperature where substantial degradation of the complexes initiates.

In addition to the line cut plots which provided information about the particle size, the relative amount of particles can also be examined by plotting the

scattering intensity at the bump location, q_{xy}^* , as a function of temperature, as shown in Figure 4.4. For this, the scattering intensity at the nanoparticle bump location for each series of scattering curves for the two Pd-TMV chips (small and large particles) was extracted at $q_{xy}^*= 0.13 \text{ \AA}^{-1}$ and 0.04 \AA^{-1} respectively, and at the metallic shell location ($q_{xy}^*=0.03 \text{ \AA}^{-1}$) for the small particle chip for the data in Figure 4.3(b) and (c). The normalized scattering intensity with respect to the initial intensity was plotted as a function of the temperature.

The normalized intensity in Figure 4.4 is thus proportional to the number fraction of nanoparticles, which remained constant. The data for the small particle sample shows fluctuations in intensity because the signal at high q_{xy} was weak and noisy, as seen in Figure 4.3(b). The disappearance of both particle sizes and the metallic shell structure occurred rapidly at 200°C , which is consistent with the destruction temperature of TMV (shown in Figure 4.3(a)). This result further confirms the outcome of the analysis of linecut plots in Figure 4.3, and suggests the coupling of particle degradation with the destruction of TMV.

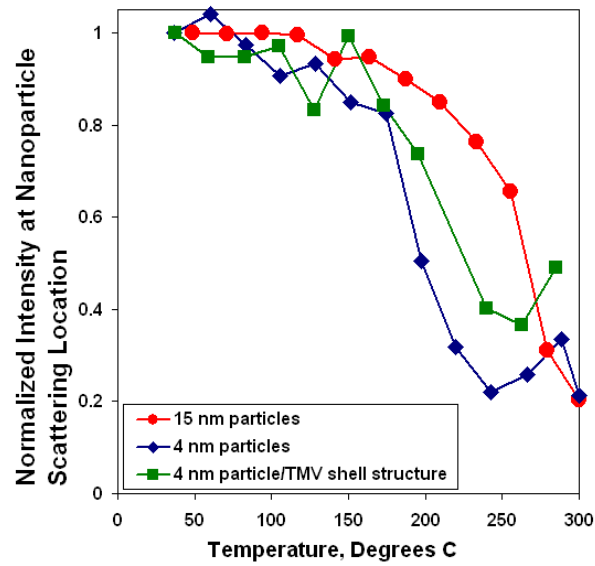


Figure 4.4: Plot of normalized intensity at the nanoparticle bump-like scattering location, q_{xy}^* , vs. temperature for the 15nm particles (red circles), 4nm particles (blue diamonds) and the particle-TMV shell structure for the small particle Pd-TMV chip (green squares).

Importantly, the sintering kinetics of the particles on TMV appears to be quite unique as compared to particles on solid substrates reported in other studies, where the thermal stability of Pd nanoparticles ranged from 100°C to over 300°C.[65, 84, 85] We observed slightly higher thermal stability of the larger particles on TMV as compared to the smaller particles on TMV. The scattering intensity of the smaller particles decreased earlier in heating than the scattering intensity of the larger particles. In other words, the scattering intensity rising from the smaller particles decreased to half of the normalized intensity earlier during heating than for the larger particles, indicating that more small particles agglomerated at a lower temperature than the larger particles.

In general, thermally driven particle aggregation is explained in terms of surface energy calculations, where particles aggregate to reach a more stable thermodynamic state. This can be explained using the Gibbs-Thomson relation (Equation 4.1), where the chemical potential, μ , of a particle depends on the radius of curvature, r_c , of the particle.

$$\mu = \mu_o + \frac{2\gamma\Omega}{r_c} \text{ (Equation 4.1)}$$

Thus, based on the Gibbs-Thomson relation, where Ω is the atomic volume and μ_o is the chemical potential of an infinite size particle, larger particles grow at the expense of smaller particles that have a higher chemical potential. As a result, the driving force for aggregation is the reduction of total surface energy

of the system, which is achieved through the formation of fewer larger particles. Similarly, the Gibbs-Thomson relation can be written in terms of melting temperature as a function of particle diameter, as shown in Equation 4.2.

$$\Delta T_M = T_M - T_M(\infty) = \frac{4\sigma T_M}{d\Delta H_F \rho_S} \text{ (Equation 4.2)}$$

Equation 4.2 (where T_M is the melting temperature, $T_M(\infty)$ is the bulk melting temperature, ρ_S is the density of the particle, ΔH_F is the latent heat of fusion, d is the particle diameter and σ is the liquid-solid interface energy), shows that the melting temperature and particle size are proportional.[86] Based on this explanation, it is expected that the smaller nanoparticles supported on TMV will agglomerate at a lower temperature than the larger particle case.

In conclusion, the observed dynamic changes shown above suggest the coupling of the nanoparticle stability with the stability of the viral nanotemplates. It appears that the thermal stability of the TMV structure is enhanced by the Pd nanoparticles, shown in Figure 4.3(b) where the degradation temperature of TMV is increased to 240°C from 209°C. Similarly, the stability of the Pd nanoparticles is greatly enhanced by the presence of TMV, as shown by the higher thermal stability of the particles on TMV (Figure 4.3(b), (c) and Figure 4.4) as compared to the larger (and theoretically more thermally stable) particles on gold (Figure 4.3(d)). In other words, the viral-metal nanoparticle complexes start to degrade at

the TMV structure's degradation temperature as shown in Figure 4.4, but the stability of both the TMV structure and the nanoparticles are significantly enhanced by the viral-metal complex; 240°C and 279°C in Figures 4.3(b) and (c) respectively vs. 209°C and 214°C in Figures 4.3(a) and (d) respectively.

4.2.3 AFM Examination of Degraded Surfaces

Next, we physically examined the destruction of the Pd-TMV complex and aggregation of the Pd nanoparticles via Atomic Force Microscopy (AFM) to confirm the final observations made via GISAXS, as shown in Figure 4.5. For this, all chips were examined using tapping mode AFM after the heating was complete without further rinsing or sample treatment.

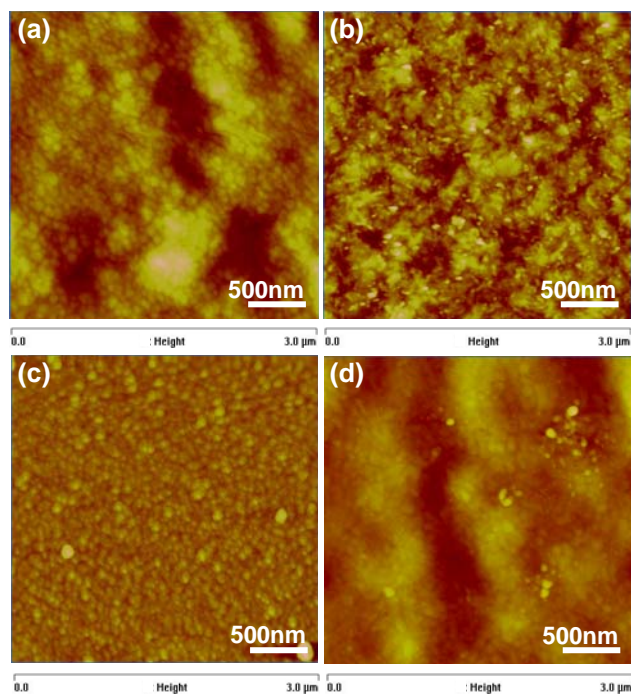


Figure 4.5: AFM images of (a) TMV chip, (b) Pd-TMV chip with small nanoparticles, (c) Pd-TMV chip with large nanoparticles and (d) a Pd-Au chip after heating.

First, Figure 4.5(a) shows an AFM image of a TMV chip after heating. The surface resembles a clean gold chip, where the mildly rough granular curvature of the gold surface is visible. Importantly, the clear tubular structures of the surface bound TMV's are no longer visible after the heating experiment, in contrast to the samples prior to heating (Figure 3.3(a)) indicating the disappearance of the TMV's through heating. Next, Figures 4.5(b) and (c) show the surfaces of the Pd-TMV chips with small and large particles respectively, after heating to 300°C. Both surfaces appear densely covered with small and large randomly organized particles. Importantly, there are no distinct nanotubular structures of TMV's visible on either surface as in Figures 3.3(b,c) before heating, clearly indicating the destruction of the Pd-TMV complexes. It is evident from these AFM results that all viruses and viral-nanoparticle complexes are destroyed below 300°C. Finally, Figure 4.5(d) shows an AFM image of a Pd-Au chip after heating. The surface of the Pd-Au chip resembles the surface of a clean gold chip, with few clusters of large particles randomly dispersed on the surface. The surface of the Pd-Au chip appears to have significantly less agglomerated particles than the Pd-TMV chips, as expected by the significantly fewer Pd nanoparticles initially formed on the chip as compared to the Pd-TMV chips.[67] Importantly, it is clear that in all Pd samples, the nanoparticles agglomerated during heating, further confirming the GISAXS results and the disappearance of scattering species in the GISAXS-measurable range. In conclusion, the AFM images in Figure 4.5 indicate the thermal degradation of the virus and viral-

nanoparticle complexes, confirming GISAXS-based results shown in Figures 4.2 through 4.4.

4.3 Conclusions

In this chapter, we examined the thermal stability of viral-nanoparticle complexes assembled on solid substrates via *in situ* GISAXS to monitor subtle dynamic changes at the nanoscale. The GISAXS images clearly showed that the samples changed significantly over the course of the heating experiments, and that these changes were readily detectable with GISAXS. The GISAXS curves allowed us to pin-point the temperatures at which each sample was destroyed. First, it was observed that TMV degraded at a higher temperature (about 200°C) than previously reported for TMV in aqueous solution, and its thermal stability was further enhanced by the Pd nanoparticles formed on the TMV surface. Similarly, it was shown that the thermal stability of the Pd nanoparticles were greatly enhanced by TMV, as the degradation temperature of the particles were increased from 214°C on gold chips to 240°C and 279°C for small and large particles on TMV, respectively. Also, the degradation of the TMV and Pd nanoparticles appeared to be coupled since the particles began agglomerating at the TMV degradation temperature. This was shown by the drop in intensity at the nanoparticle bump location in the Pd-TMV scattering curve plots when the samples were heated to the TMV degradation temperature, 209°C in this case. Further *ex situ* AFM examination of the degraded samples (Figure 4.5) showed

clear disappearance of TMV's nanotubular structures and the presence of very large particles, confirming our GISAXS-based observations. While we focused on reporting major structural changes in this study, detailed nanoparticle size change can also be readily examined via Guinier analysis.[64] Specifically, no notable change in the particle diameter at sub-nanometer scale were observed until the major structural changes started to occur in all the samples examined. Combined these results demonstrate the applicability of the *in situ* GISAXS method to monitor subtle dynamic changes in the Pd-TMV complexes over the course of heating, and provide insights on the thermal stability of such hybrid nanomaterials. We believe that the methodology and results reported here represent a significant first step toward understanding dynamic behaviors of viral-inorganic hybrid materials and nanodevices, and envision more future endeavors in nano-bio and functional hybrid materials research for a wide range of applications such as batteries, sensors, catalysts and nanoelectronics.

5 *IN SITU* SAXS ANALYSIS OF THE PALLADIUM NANOPARTICLE GROWTH MECHANISM IN THE ABSENCE OF TMV1CYS NANOTEMPLATES

Our approach to the controlled fabrication of palladium (Pd) nanoparticles exploits the high density thiol functionality on TMV1cys nanotemplates. Our previous study[64] (Chapter 3) showed that particle size is tunable based on simple reaction parameters, however in order to achieve predictable Pd nanoparticle growth, we must understand how Pd precursor is reduced to form Pd particles using sodium hypophosphite reducer. Therefore, an in depth understanding of Pd nanoparticle growth in the *absence* of the TMV1cys templates would enable us to better understand the electroless reduction of Pd precursor using sodium hypophosphite, and to determine the role of TMV1cys in particle formation (described later in Chapter 6). Additionally, a detailed understanding of Pd particle growth in pristine conditions, in the absence of stabilizing agents, will provide valuable insight to a broader range of systems in various research areas.

Despite the fact that Pd nanoparticles have attracted significant attention due to their catalytic properties,[1] few *in situ* growth studies have been conducted to further understand the fundamental mechanism of Pd nanoparticle growth. Moreover, capping agents or support materials are often used to keep the

nanoparticles well-dispersed,[14-16] thus Pd particle growth studies in pristine conditions without such interferences are lacking.

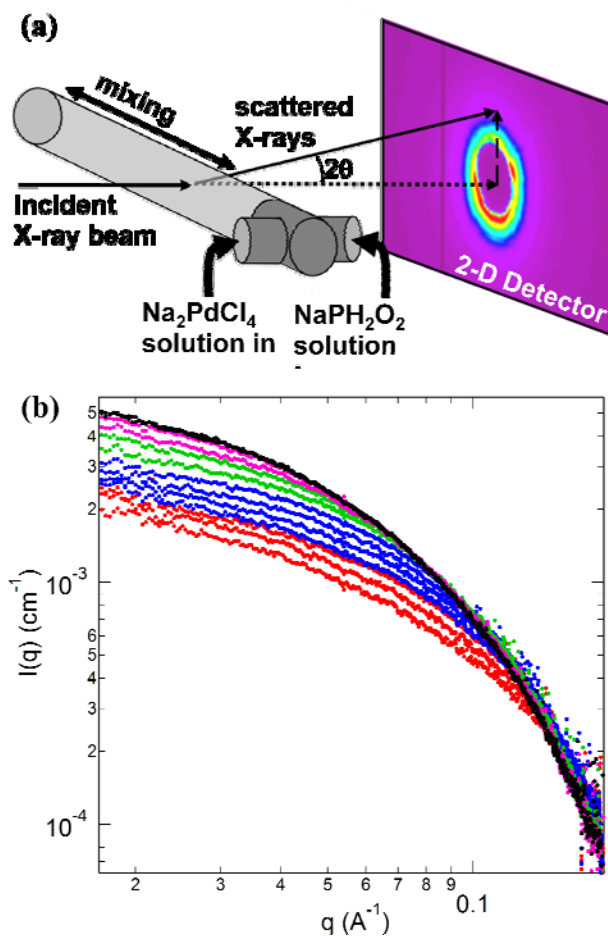


Figure 1: (a) Schematic diagram of *in situ* SAXS setup. Pd precursor (Na_2PdCl_4) and sodium hypophosphite (NaPH_2O_2) solutions were fed into a quartz capillary and constantly mixed, forming Pd nanoparticles. The incident X-ray beam penetrated the quartz capillary, and the scattered rays were recorded at low angles on a 2-D CCD detector. (b) Typical *in situ* scattering curves acquired by making a line cut of intensity (inset) and plotting intensity as a function of the scattering vector q . Curves shown are background subtracted scattering curves, where the scattering intensity from water has been subtracted. Colored curves represent SAXS measurements made during the full measured Pd nanoparticle growth period (10 minutes), where time progresses in the order of red, blue, green, pink and black.

In this chapter, we thoroughly examine the growth of Pd nanoparticles through the chemical reduction of Pd precursor with a mild reducing agent (similar to the common autocatalytic process of “electroless plating”)[62, 63] via *in situ* SAXS, as shown in the schematic diagram of Figure 1(a). The representative background subtracted SAXS curves in Figure 1(b), obtained from the scattering images, enables an in depth analysis of the nanoscale system, resulting in statistically meaningful information on the particle size and shape.[70, 78, 87] Invariant calculations show that the amount of scattering Pd species converted from non-scattering precursor increased with increasing Pd precursor concentration. Furthermore, final particle diameter consistently increased with increasing Pd precursor concentration, and with less dependence on reducing agent concentration. These observations clearly indicate rapid initial nucleation, followed by growth through Pd precursor conversion to Pd particles for the majority of Pd particle growth in this system. Slight further growth by agglomeration (i.e. merging of a few individual particles into larger individual particles that are still within the detection range and soluble) and then particle aggregation (i.e. clustering and precipitation of particles to form larger clumps that are outside the 1-50nm detection range) then ensued in some cases. Further investigations via *ex situ* TEM verified the SAXS-based size estimations, while X-ray Photoelectron Spectroscopy (XPS) results (Supporting Information) elucidated the difference in chemical state of particles formed in varying conditions.

Based on these findings, we propose a four-step Pd particle growth mechanism: (1) Rapid formation of nuclei initiated by the hypophosphite reducer, (2) further growth through the conversion of precursor to Pd particles, (3) slight particle growth by agglomeration of particles formed in Step 2 to form larger individual particles, and finally (4) aggregation of particles. We envision that the results and methodology presented here could lead to an in depth fundamental understanding of Pd nanoparticle growth in a wide variety of systems.

5.1 Materials and Methods

5.1.1 Materials

Sodium tetrachloro-palladate (II) (Na_2PdCl_4) was used as the Pd precursor for Pd nanoparticle formation (Sigma-Aldrich, St. Louis, MO). Precursor reduction was conducted using sodium hypophosphite (Sigma-Aldrich)

5.1.2 Pd Nanoparticle Formation

Pd nanoparticles were formed by reducing Pd precursor with sodium hypophosphite at neutral pH. Equal volumes (30 μl each) of the precursor and the reducer were loaded into separate tubing, and then mixed by flowing the two solutions through a Y-shaped connector into a quartz capillary. SAXS patterns were recorded every three seconds, where the initial measurement was recorded

as the two solutions mixed in the capillary. The precursor/reducer solution was mixed throughout particle growth by flowing the solution in and out of the capillary.

5.1.3 *In situ* Small-Angle X-ray Scattering

SAXS measurements were conducted at the Advanced Photon Source (Argonne National Lab, Argonne, IL) 12 ID-C beamline. The incident X-rays, with energy of 12 keV, were irradiated on the sample in a quartz capillary. The scattered rays at small angles (less than 2°) were recorded on a 2-D CCD detector, as shown in Figure 1(a), with a sample to detector distance of approximately 2 meters. Measurements were recorded every three seconds for ten minutes total. The X-ray exposure time was 0.1 seconds per measurement, thus we neglect the influence of X-ray induced particle formation. The background scattering curve from water was then subtracted from all data curves prior to all further SAXS calculations.

5.1.4 Transmission Electron Microscopy (TEM)

Pd nanoparticles were formed by mixing precursor and reducer solutions for ten minutes under constant mixing by pipette. 5 μ l of solution was placed on a copper TEM grid (Electron Microscopy Sciences, Hatfield, PA), and allowed to sit for two minutes. The grid was then placed on filter paper to wick away the

liquid. TEM samples were probed with a JEOL-2100 High Resolution TEM at the Center for Nanoscale Systems (CNS) at Harvard University.

5.1.5 Inductively Coupled Plasma (ICP)

Pd nanoparticles were prepared as described above for TEM samples. Pd particles were then separated from the remaining solution by ultracentrifugation at 35,000 RPM for one hour at 4°C. Concentrated nitric acid (Sigma Aldrich) was added to the supernatants to a final concentration of 5%. The samples were then examined with Inductively Coupled Plasma (ICP) (Leeman Labs Prodigy ICP). The reduction yield was calculated by subtracting the amount of Pd ions measured in the remaining supernatant from the original concentration of Pd precursor.

5.1.6 X-ray Photoelectron Spectroscopy

Pd nanoparticles were formed as described above for the TEM sample preparation. 200 μ l of solution was placed on a clean SiO₂ chip, and dried for one week to allow particles to adsorb to the chip surface. The chips were then washed thoroughly with deionized water for 20 minutes, and dried with ultrapure Nitrogen gas. The chips were placed under high vacuum and probed using an SSX-100 ESCA X-ray Photoelectric Spectrometer at the Center for Nanoscale Systems (CNS) at Harvard University.

5.2 Results and Discussion

5.2.1 Pd Precursor Conversion

As shown in Figure 5.2, we first employed the Invariant parameter (Q) to examine the conversion of palladium (Pd) precursor to Pd nanoparticles. Q was calculated from the scattering intensity as a function of q , as described by Equation 2.9 in the SAXS Theory Chapter, 2.3.3. Figure 5.2 shows the change in Q over time for particles formed in 2.5mM and 15mM sodium hypophosphite. The absolute scattering intensity was not measured in this work; however the same sample volume was used for all measurements. Thus Q represents the relative amount of scattering Pd (particles in this case) converted from dissolved Pd precursor (which does not contribute to the SAXS signal upon solution background subtraction) and serves as a comparison between the amounts of Pd particles formed in each condition.

Generally, all samples show a rapid initial increase in Q within a few seconds, indicating fast conversion of Pd precursor molecules to scattering Pd. We attribute this rapid initial conversion to the nucleation step of nanoparticle formation. Next, all samples show a slower increase in Q (3 to 200 seconds, shown in the inset of Figures 5.2(a) and (b)) indicating slower conversion of precursor to scattering Pd within the detection range of this SAXS setup. All samples reached a maximum Q value around or before 200 seconds, indicating

that conversion of precursor to scattering Pd particles was complete within 200 seconds. However, completion of the conversion of precursor did not indicate the completion of the growth of the particles in all cases, as shown later in Figures 5.5 and 5.10. Finally, in the case of high Pd precursor concentration samples, Q decreased after reaching a maximum value, indicating a decrease in scattering species present in the scattering volume that is in the path of the X-ray (e.g. 5mM Pd precursor concentration sample in Figure 5.2(b), shown as solid squares). This decrease in Q for higher Pd precursor concentration samples (5mM and 1.5mM) is due to the aggregation of particles forming large “clumps” on the capillary walls that were observable by eye and were significantly larger than the measureable size limit of this SAXS setup. In order to combat this potential interference, the quartz capillary was changed after each sample with noticeable amounts of Pd stuck to the capillary walls. Comparing samples with the same Pd precursor concentration and different hypophosphite concentrations, the speed of conversion did not appear to be drastically affected by hypophosphite concentration, as shown by the insets in Figure 5.2(a) and (b). However, there appears to be a faster increase in Q (or steeper slope) for higher Pd precursor concentration samples. Estimated slopes for Pd precursor concentrations increase with increasing Pd precursor concentration within each hypophosphite series, as shown in Table 5.1 (based on a linear regression fit for the time range with the greatest change in Invariant, Figure 5.2).

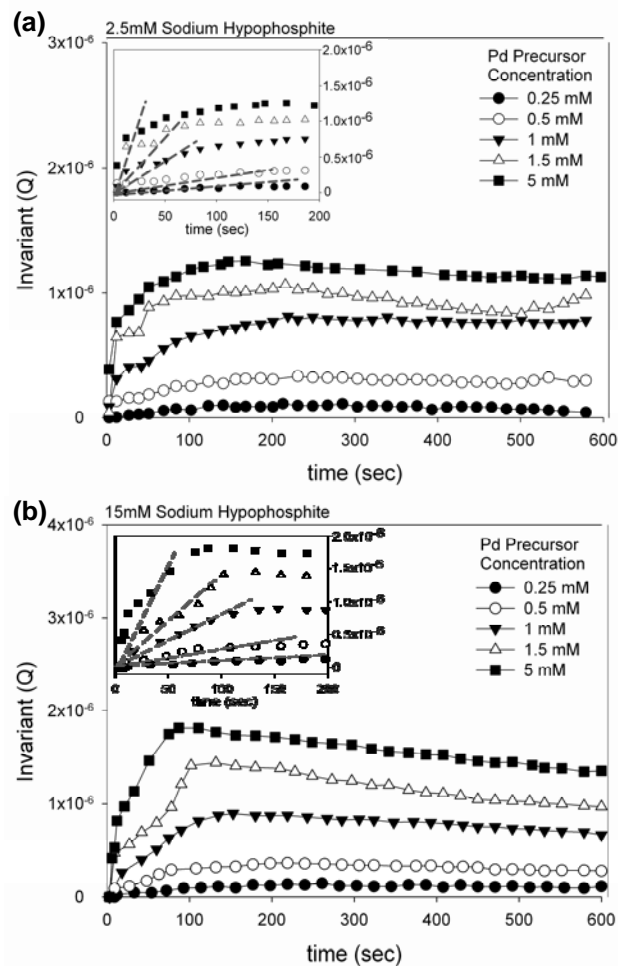


Figure 5.2: Plot of Invariant (Q) versus time for samples prepared in (a) 2.5mM or (b) 15mM sodium hypophosphite with 0.25mM (closed circles), 0.5mM (open circles), 1mM (closed triangles), 1.5mM (open triangles) and 5mM (closed squares) Pd precursor. Insets: Magnified plots in 0-200 second range showing approximate slopes of early growth for each sample.

Hypophosphite Concentration (mM)		2.5	15
Pd Precursor Concentration (mM)	Time Range	Slope	Slope
0.25	0-186 sec	5×10^{-10}	2×10^{-9}
0.5	0-177 sec	3×10^{-9}	7×10^{-9}
1	0-111 sec	5×10^{-9}	2×10^{-8}
1.5	0-102 sec	1×10^{-8}	4×10^{-8}
5	0-87 sec	2×10^{-8}	7×10^{-8}

Table 5.1: Approximate slopes of early conversion, calculated using a linear regression fit for the time range with the greatest change in Invariant in Figure 5.2.

Next, we examined the relationship between Pd precursor concentration and maximum precursor conversion, as shown in Figure 5.3. The maximum Invariant (Q_{max}) from samples shown in Figure 5.2 were calculated (see SAXS Theory Section, 2.3.3) and plotted versus Pd precursor concentration. Figure 5.3 shows that the amount of precursor converted to scattering Pd species (nanoparticles in this case) increased with increasing Pd precursor concentration. At lower Pd precursor concentrations (below 5mM Pd precursor) Q_{max} increased linearly with increasing Pd precursor concentration in log-log scale, while the hypophosphite concentration showed little influence. However, at high Pd precursor concentration (5mM) Q_{max} was lower at 2.5mM hypophosphite than at 15mM hypophosphite, indicating lower conversion of Pd precursor to Pd particles. This phenomenon was confirmed via Inductively Coupled Plasma (ICP) measurements of the amount of Pd ions present in the supernatant after particle formation (See Figure 5.4). All samples tested exhibited near 100% reduction of Pd ions, with the exception of the 5mM Pd precursor sample prepared in 2.5mM hypophosphite, where approximately 80% reduction of Pd ions was measured. Thus, for low Pd precursor concentration samples, regardless of the concentration of hypophosphite, the following relationship can be deduced from Figure 5.3:

$$\ln(Q_{max}) = k \ln([Pd]_0) + C_1 \quad (\text{Equation 5.1})$$

where k is the slope, $[Pd]_0$ is the initial dissolved Pd precursor concentration, and C_1 is the intercept. Therefore, we obtain the relationship in Equation 5.2:

$$Q_{\max} = C_2 \cdot [Pd]_0^k \quad (\text{Equation 5.2})$$

where $k \approx 1$ and C_2 is the factor relating the initial amount of Pd precursor concentration to the scattering intensity. This nearly linear relationship, determined using Q_{\max} and confirmed with ICP, indicates that the amount of Pd precursor converted depends on the initial amount of Pd precursor used, and is less related to hypophosphite concentration at low Pd precursor concentrations. Thus, we hypothesize that Pd precursor conversion may be driven by the autocatalytic nature of Pd, consistent with previous reports in other chemical reduction (i.e. electroless deposition) systems (discussed further in the Discussion Section).[63, 88] Meanwhile, the measured Q_{\max} values for both 5mM Pd precursor samples (two right-most points in Figure 5.3) are lower than the expected maximum value, due to the apparent aggregation and “clumping” of the particles, as well as the lower measured conversion (Figure 5.4) of the sample prepared at 2.5mM hypophosphite, thus neither fit the expected linear relationship.

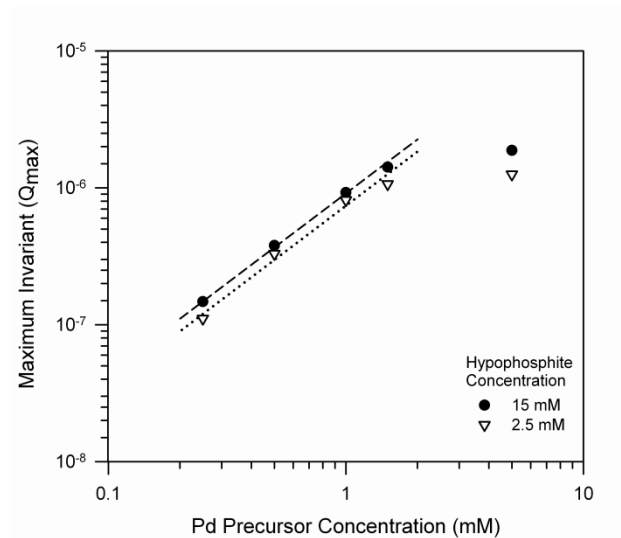


Figure 5.3: Maximum Invariant (Q_{max}) vs. Pd precursor concentration in log-log scale for 15mM hypophosphite series (closed circles) and 2.5mM hypophosphite (open triangles).

Inductively Coupled Plasma (ICP) was utilized to investigate the extent of reduction of palladium (Pd) precursor ions by measuring the amount of Pd ions remaining in the supernatant after particle formation and separation, as shown in Figure 5.4. For this, Pd nanoparticles were formed by mixing Pd precursor and sodium hypophosphite reducer, and then mixing by continuous pipetting for ten minutes (Materials and Methods, Section 5.1.5). The Pd particles were then removed from the solutions by ultra-centrifugation, and the supernatant examined using ICP. The concentration of Pd ions remaining in the solution was measured, and subtracted from the initial Pd precursor concentration to give the amount of Pd precursor ions converted to Pd particles, as shown in Figure 5.4.

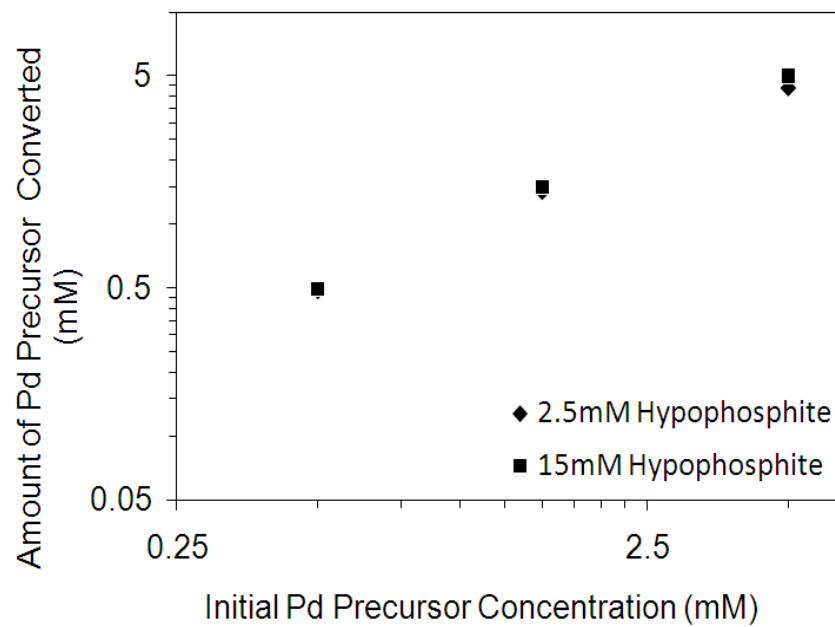


Figure 5.4: Amount of Pd precursor converted from Pd precursor ions to Pd particles for samples prepared in 2.5mM (diamonds) and 15mM (squares) hypophosphite.

The chemical reduction of Pd precursor by sodium hypophosphite is known to proceed with approximately 35% efficiency due to side reactions that produce elemental phosphorus and hydrogen (Equations 5.4-5.10, Section 5.2.3). Therefore, it is expected that full reduction of Pd precursor by hypophosphite will occur when hypophosphite is in excess of Pd precursor by approximately three times.[63] First, all samples prepared in sufficient hypophosphite (all 15mM hypophosphite samples, and 0.5mM Pd precursor with 2.5mM hypophosphite) show full conversion of Pd precursor ions to Pd particles, as no significant amount of Pd ions were measured in solution after particle formation. Importantly, samples prepared with 1.5mM or 5mM Pd precursor with 2.5mM hypophosphite, where hypophosphite concentration was less than sufficient, showed higher than expected reduction yields; 95% (1.43mM converted out of 1.5mM Pd precursor) and 88% (4.4mM converted out of 5mM Pd precursor) as compared to the expected 58% and 17.5% conversion, respectively.

In summary, the examination of the Q parameter in Figures 5.2 through 5.4 provided insight into the conversion of dissolved, non-scattering precursor to scattering Pd nanoparticles. We observed that the initial conversion of precursor to particles was very rapid, suggesting fast nucleation, as shown in Figure 5.2. Conversion of precursor to scattering species then became slower, followed by a decrease in Q in some cases indicating aggregation of particles outside of the measureable size range of this SAXS setup. Figure 5.3 shows the relationship between the maximum conversion (Q_{max}) of Pd precursor to Pd nanoparticles and

the concentration of reducer or precursor. Q_{max} increased linearly (in log-log scale) with increasing initial Pd precursor concentration (at lower Pd precursor concentrations) with no significant relationship to hypophosphite concentration, indicating that Pd precursor conversion could be driven by the autocatalytic nature of Pd. Finally, ICP measurements showed that most samples exhibited near 100% conversion of Pd precursor ions to Pd particles.

5.2.2 Analysis of Pd Nanoparticle Size

Next, as shown in Figure 5.5, average Pd nanoparticle diameter was monitored throughout particle growth using *in situ* SAXS. For this, scattering curves were obtained from continually measured scattering images as shown in Figure 5.1(b). The average diameter of Pd particles was then calculated using the Guinier analysis (SAXS Theory Section, Chapter 2). Figure 5.5 shows the increase in the average diameter of particles formed in 2.5mM and 15mM sodium hypophosphite at various Pd precursor concentrations for 600 seconds.

First, Figure 5.5(a) shows the increase in average diameter of Pd nanoparticles in 2.5mM hypophosphite. Pd particles prepared in higher Pd precursor concentrations (1mM, 1.5mM and 5mM) grew to a larger final size than particles formed in lower Pd precursor concentrations (0.25mM and 0.5mM). Measurements prior to 100 seconds were unstable, presumably because the low amounts of small particles were undetectable.

Next, Figure 5.5(b) shows the growth of Pd nanoparticles formed in 15mM hypophosphite. Similar to the results shown in Figure 5.5(a), the lower Pd precursor concentration samples (0.25mM and 0.5mM) appeared to reach their maximum diameter earlier than the samples prepared with higher Pd precursor concentrations (1mM, 1.5mM and 5mM). The measurements of the sample prepared with 0.25mM precursor fluctuated throughout growth, largely due to the low amount of scattering species present. However, the average particle size remained generally constant after 200 seconds. In contrast, the samples prepared with higher Pd precursor concentration (1mM, 1.5mM and 5mM) did not reach their maximum diameter until approximately 400 seconds.

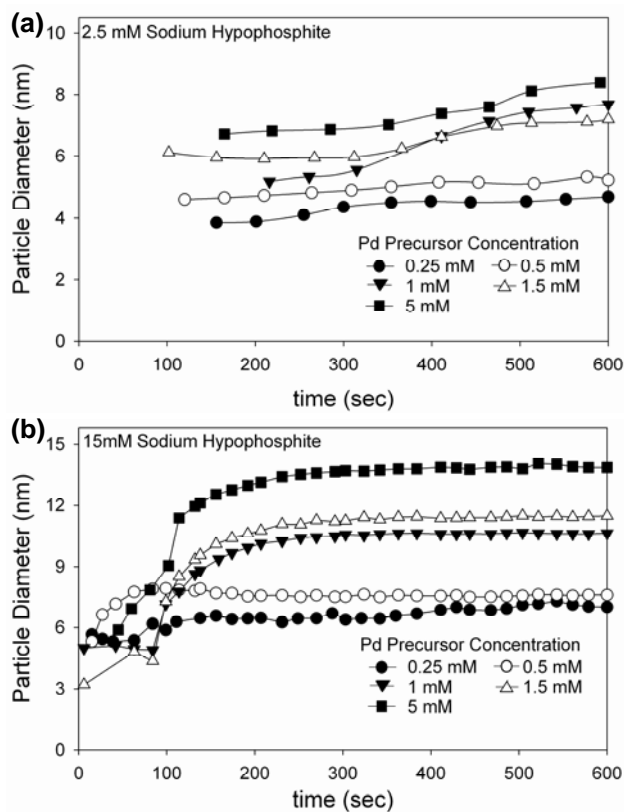


Figure 5.5: Change in particle diameter as a function of time for particles formed in (a) 2.5mM or (b) 15mM sodium hypophosphite and 0.25mM (closed circles), 0.5mM (open circles), 1mM (closed triangles), 1.5mM (open triangles) and 5mM (closed squares) Pd precursor.

In both Figures 5.5(a) and (b), there were minor increases in the nanoparticle diameter after reaching a maximum Invariant, (200 seconds or less) especially in the case of high Pd concentration samples. This could be partly due to the agglomeration of smaller particles to form larger particles by oriented attachment. In contrast to the classical mechanism of atom/molecule mediated growth of a single crystal, oriented attachment involves the fusion of several nanoparticles to form a larger distinct particle.[89] In the case of oriented attachment, the total converted Pd precursor (thus Q) does not change; only the size of the particles changes due to smaller particles combining to form larger ones. Nonetheless, it is apparent that this process is not the major growth process since the resulting size change is minor.

As shown in Figure 5.6, we next summarize the relationship between Pd precursor concentration and average nanoparticle diameter. For this, the maximum average particle diameter of each sample shown in Figure 5.5, calculated via Guinier analysis, was plotted versus Pd precursor concentration in log-log scale. First, Figure 5.6 shows that, in general, the average particle diameter increased with increasing Pd precursor concentration. Second, particle diameter was consistently larger for particles prepared in higher concentrations of sodium hypophosphite.

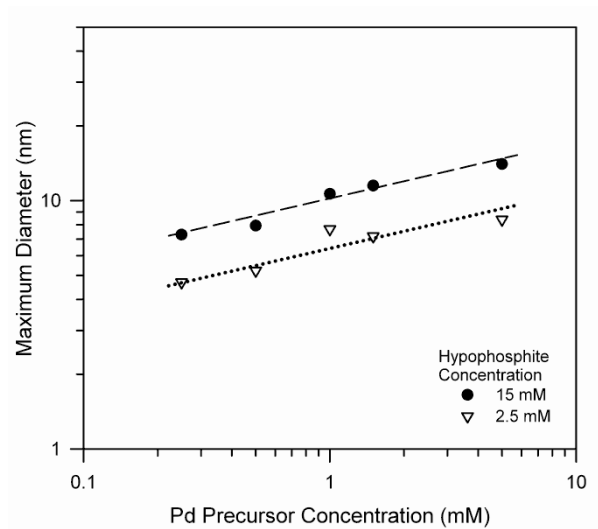


Figure 5.6: Maximum particle diameter, calculated via Guinier analysis, versus Pd precursor concentration, for 15mM hypophosphite (closed circles) and 2.5mM hypophosphite (open triangles) series.

The relationship between diameter and Pd precursor concentration is significant within each hypophosphite series, and is approximately linear in log-log scale, with the two reducer conditions having similar slopes which are about 1/3, resulting in the relationship in Equation 5.3:

$$[Pd]_0 = C_3 \cdot R_{max}^3 \quad (\text{Equation 5.3})$$

where C_3 is a constant that varies with hypophosphite concentration, and R_{max} is the final particle radius. Additionally, we observe that particle size is also influenced by hypophosphite concentration, where higher hypophosphite concentration resulted in larger particle diameter.

It is clear from Figures 5.5 and 5.6 that the Pd particle diameter increased with increasing Pd precursor concentration within each series of hypophosphite concentration, and with higher hypophosphite concentration. Figure 5.5 clearly shows that Pd particles reached a maximum earlier in the experiment for high hypophosphite concentration samples, as compared to low hypophosphite samples. Additionally, Figure 5.5 shows that the majority of particle growth occurs simultaneously with the increase in Invariant (200 seconds or earlier), and that minor growth occurs in some cases after conversion as concluded (200 seconds or later). The strong correlation between particle size and Pd precursor concentration, as shown in Figure 5.6 and by the relationship in Equation 5.3, indicates that particle growth could be driven by the autocatalytic nature of Pd.

To further understand the effect of precursor and reducer concentration on particle size, the final particle size distributions were calculated, and described in Section 2.3, as shown in Figure 5.7.

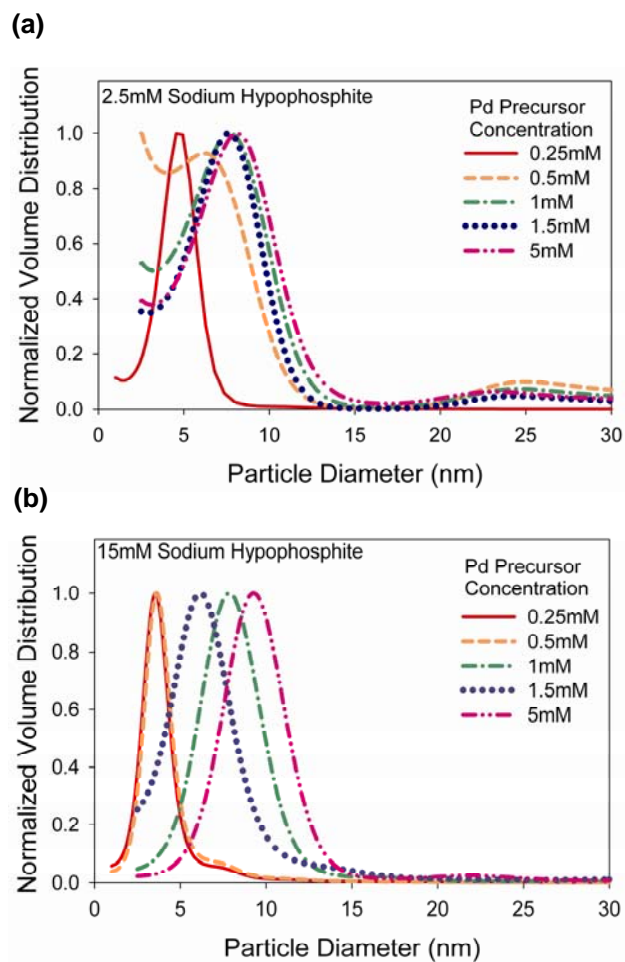


Figure 5.7: Final Pd nanoparticle size distributions calculated using Irena software at the end of particle growth for particles formed in (a) 2.5mM or (b) 15mM hypophosphite.

Figure 5.7 shows normalized particle volume distributions calculated from the final SAXS measurement for each sample. First, it is apparent from Figure 5.7 that the size distributions of Pd nanoparticles are more uniform at lower Pd precursor concentrations for all sodium hypophosphite concentrations. In addition, it is clear that particle size increases with increasing Pd precursor concentration, consistent with results shown in Figure 5.3 calculated using the Guinier method.

Upon closer inspection, Figure 5.7(a) shows size distributions of Pd nanoparticles formed in 2.5mM hypophosphite. The lowest Pd precursor concentration (0.25 mM) resulted in highly uniform 5nm particles, whereas all other Pd precursor concentrations resulted in polydisperse particles. Next, Figure 5.7(b) shows size distributions of particles formed in 15mM hypophosphite. The two lowest Pd precursor concentrations (0.25mM and 0.5mM) resulted in small and uniform particles approximately 4nm in diameter, whereas higher Pd precursor concentrations resulted in larger and more polydisperse particles. The polydisperse nature of the larger nanoparticles indicates that Ostwald Ripening type growth is not present in the conditions examined in this study because Ostwald Ripening growth typically results in large and monodisperse particle populations.³

Combined, these results show that the Pd particles became smaller and more uniform at lower Pd precursor concentration, and that hypophosphite

concentration did not have a significant effect on the size distribution. Additionally, this result shows that we do not observe Ostwald Ripening growth (within the time, temperature and concentration ranges studied) where larger particle sizes are typically more monodisperse. Importantly, the size distribution simulations shown here correlate well with the Guinier analysis results employed for Figures 5.5 and 5.6.

Combined, the SAXS results presented in Figures 5.2 through 5.7 provide significant insight into the growth of Pd nanoparticles in this system. First, the Invariant results indicate that Pd precursor is rapidly converted to Pd nanoparticles, and that conversion is complete within 200 seconds. Maximum Invariant increased with increased Pd precursor concentration at low Pd precursor concentrations, with little effect from hypophosphite concentration, suggesting that hypophosphite plays a lesser role in the amount of Pd converted. Particle size was also strongly related to initial Pd precursor concentration, where larger particles were formed in higher Pd precursor concentrations. Hypophosphite concentration also influenced Pd particle size, where higher hypophosphite concentration resulted in larger particles.

The validity and accuracy of the size estimates,[55] calculated with the Guinier Analysis (Figures 5.5, 5.6) and simulated size distributions via Irena software (Figure 5.7), were further confirmed using *ex situ* Transmission Electron Microscopy (TEM), as shown in Figure 5.8. For this, Pd nanoparticles were

prepared by mixing Pd precursor and reducer by continuous pipetting and then analyzed with TEM. First, Figure 5.8(a) shows Pd particles formed in 1mM Pd precursor and 2.5mM hypophosphite. The particles ranged from 6nm to 11nm in diameter, which correlates well with the SAXS-based estimates shown in Figures 5.5(a) and Figure 5.7(a). Next, Figure 5.8(b) shows particles formed with 1.5mM Pd precursor and 15mM hypophosphite, where the 6nm diameter particles correspond to the SAXS-based size estimates presented in Figures 5.5(b) and 5.7(b). Figure 5.8(c) shows uniform 8nm particles formed with 5mM Pd precursor and 2.5mM hypophosphite that are faceted, yet generally spherical in overall shape. Finally, Figure 5.8(d) shows particles formed with 5mM Pd precursor and 15mM hypophosphite. These particles are 8nm in diameter, validating the *in situ* SAXS-based measurements presented in Figures 5.5(b) and 5.7(b).

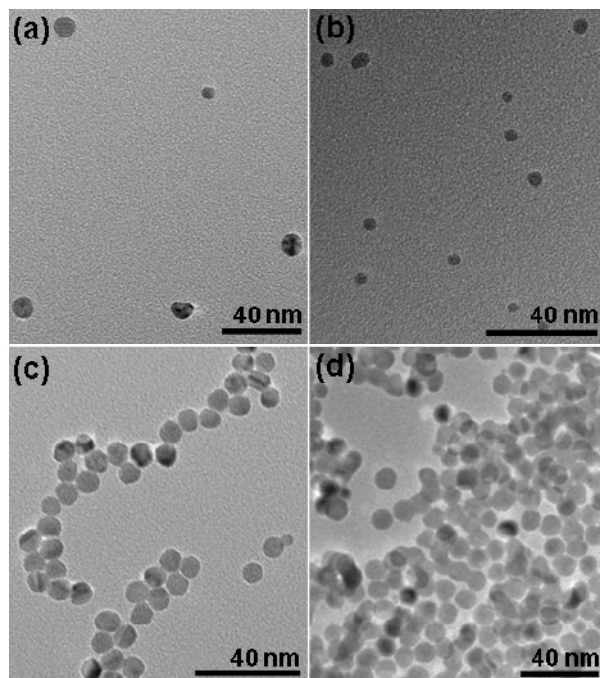


Figure 5.8: TEM images of Pd nanoparticles formed by (a) 1mM Pd precursor and 2.5mM hypophosphite, (b) 1.5mM Pd precursor and 15mM hypophosphite, (c) 5mM Pd precursor and 2.5mM hypophosphite, (d) 5mM Pd Precursor and 15mM hypophosphite.

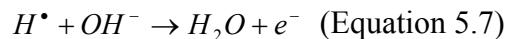
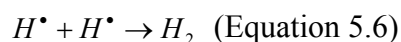
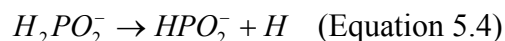
All scale bars represent 40nm.

In summary, these results demonstrate that Pd particle formation is reproducible under the conditions employed in this study, and that our SAXS-based size calculations are accurate depictions of the particle size.

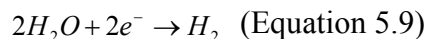
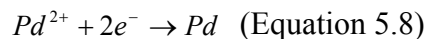
5.2.3 Proposed Four-Step Particle Growth Mechanism

The chemical reduction of metal precursors to form metal nanoparticles or nanofilms (i.e. electroless deposition), is widely known to be an inherently autocatalytic process initiated by the reducing power of the chemical reducer.[63] When sodium hypophosphite in particular is utilized as the reducer in Pd precursor reduction, the reaction is regarded to proceed with limited efficiency (35%) due to side reactions that form elemental hydrogen and phosphorus, as shown in Equations 5.4-5.10.[80]

Anodic Processes:



Cathodic Processes:



According to Equations 5.4-5.10, complete reduction of Pd precursor by hypophosphite can be expected when the hypophosphite concentration is approximately three times that of the Pd precursor concentration. Thus, the ratio of Pd precursor concentration to reducer concentration plays a significant role in the reduction yield, as shown by the ICP results in Figure 5.4. Figure 5.4 shows that complete reduction is observed for samples prepared with hypophosphite in three-times excess of the Pd precursor; specifically, all samples prepared in 15mM hypophosphite and the samples prepared with 0.5mM Pd precursor and 2.5mM hypophosphite. Importantly, higher conversion than expected is observed for several samples where the ratio of hypophosphite to Pd precursor is less than three. Specifically, near 100% conversion was observed for samples prepared in 1.5mM Pd precursor with 2.5mM hypophosphite and 80% conversion for 5mM Pd precursor in 2.5mM hypophosphite where the expected reduction yields were 53% and 16% respectively. This result clearly shows that direct reduction of Pd precursor by hypophosphite reducer cannot be the only reduction mechanism occurring in the system, and that further reduction of Pd precursor ions may be occurring on the surface of the Pd particles.

The ratio of Pd precursor concentration to reducer concentration plays a role in the metallic composition of the Pd nanoparticles. X-ray Photoelectron Spectroscopy (XPS) was conducted to further investigate the chemical states of the Pd particles, as shown in Figure 5.9. For these measurements, Pd nanoparticles were formed by combining Pd precursor and hypophosphite

reducer, (as described in the Materials and Methods Section, 5.1.6), then drying the droplets on a clean SiO₂ chip. The chips were thoroughly rinsed and dried, then probed using an SSX-100 ESCA X-ray Photoelectric Spectrometer.

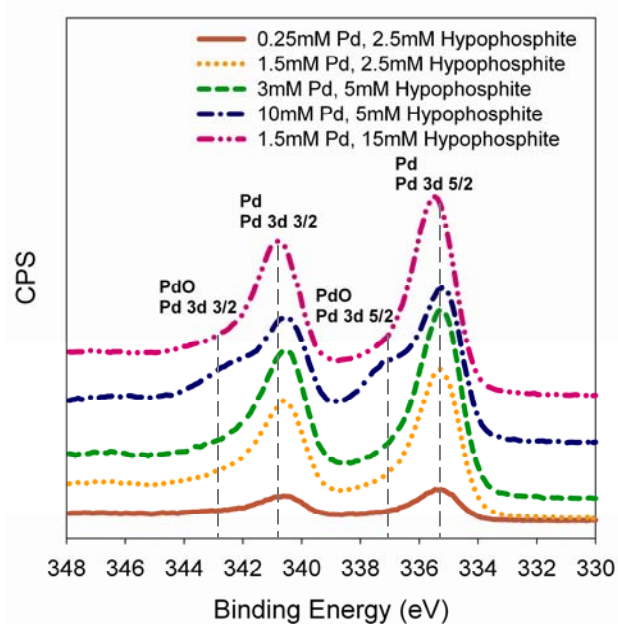


Figure 5.9: XPS analysis of Pd nanoparticles formed by (orange solid line) 0.25mM Pd precursor and 2.5mM hypophosphite, (yellow dotted line) 1.5mM Pd precursor and 2.5mM hypophosphite, (green dashed line) 3mM Pd precursor and 5mM hypophosphite, (blue dash-dot line) 10mM Pd precursor and 5mM hypophosphite, and (pink dash-dot-dot line) 1.5mM Pd precursor and 15mM hypophosphite.

First, the sample prepared in 0.25mM Pd precursor and 2.5mM hypophosphite (bottom orange solid line) shows two low peaks at 335eV and 341eV corresponding to Pd⁰. The low concentrations of precursor and reducer in this sample resulted in a low amount of particles, as described in Figure 5.2, and thus, low peaks in the XPS spectrum. Next, 1.5mM Pd precursor and 2.5mM hypophosphite (yellow dotted line) and 3mM Pd precursor and 5mM hypophosphite (green dashed line) resulted in strong peaks at 335 and 341eV. Pd precursor was in excess in both of these samples (yellow dotted line and green dashed line), however the spectra indicate that the composition of the particles was predominantly Pd⁰. The next sample examined was prepared with 10mM Pd precursor and 5mM hypophosphite (blue dash-dot line). The XPS spectra show two peaks at 335 and 341eV indicating the presence of Pd⁰; however, two shoulders are present at 337 and 343eV indicating the presence of PdO.⁴ Lastly, the sample prepared with 1.5mM precursor in 15mM hypophosphite showed a spectrum with two strong peaks at 335 and 341eV, characteristic of Pd⁰. This result was expected since hypophosphite was in significant excess for this sample, enabling the full reduction of the Pd ions. In summary, the XPS results shown in Figure 5.9 indicate that the particles prepared with sufficient or slightly lower reducer content yield predominantly fully reduced metallic Pd particles, whereas samples prepared with significant excess of Pd precursor may lead to the presence of PdO.

Based on the SAXS data presented in Figures 5.2-5.6 and Equations 5.1-5.3, we next estimate the relative number of Pd particles formed in the low Pd precursor concentration (0.25-1.5mM) conditions. Specifically, the relationship between Q and the number of converted Pd atoms can be written as Equation 5.11 assuming particle monodispersity;

$$Q = C_0(\Delta\rho)^2 NV = C_0(\Delta\rho)^2 [Pd] / n \text{ (Equation 5.11)}$$

where C_0 a constant relating the electron density to the scattering intensity, N is the number of Pd particles, V is the volume of each particle, $[Pd]$ is the number of converted Pd atoms in the form of Pd particles, and n is the number density of Pd atoms. The relationships shown in Equations 5.12 and 5.13 were determined independently from Equations 5.4 and 5.11 and from Equations 5.5 and 5.11, respectively.

$$[Pd] = n[Pd]_0 C_0 C_2 / (\Delta\rho)^2 \text{ (Equation 5.12)}$$

$$[Pd] = n[Pd]_0 N C_0 / C_3 \text{ (Equation 5.13)}$$

From Equations 5.12 and 5.13, one obtains the relationship in Equation 5.14.

$$N = C_2 C_3 / (\Delta\rho)^2 \text{ (Equation 5.14)}$$

The relationship shown in Equation 5.14 allows us to estimate the number of particles formed in the system based on constants from Figures 5.3 and 5.6, which varies with hypophosphite concentration. From Equation 5.14 and the values of C_2 and C_3 acquired from Figures 5.3 and 5.6, respectively, we estimate that the ratio of the number of particles formed in 15mM hypophosphite versus 2.5mM hypophosphite is approximately 1:4. This ratio indicates that although Q is equivalent for samples prepared in different concentrations of hypophosphite, as discussed in Figure 5.3, there were more particles formed in 2.5mM hypophosphite than in 15mM hypophosphite. This important relationship explains why the amount of converted Pd precursor is consistent despite the distinct particle size difference between the two series. In other words, the conversion of the higher number of small particles formed in 2.5mM hypophosphite is equivalent to the lower amount of larger particles formed in 15mM hypophosphite. Although the absolute number of particles formed was not measured with SAXS in this study, this could be accomplished by measuring the relationship between incident photons and the scattering intensity measured by the CCD detector, i.e. the constant C_0 . The relationships presented here assume particle monodispersity and provide simply an estimate of particle number for comparison between samples. However, the mathematical relationship presented here provides insight into the number of particles formed in the system under different reducer conditions without having measured the absolute particle number.

Next, if we assume that the densities of all Pd particles are the same for both hypophosphite series; this result indicates two findings for the low Pd precursor concentration cases (0.25-1.5mM). (1) The number of Pd particles is constant, regardless of initial Pd precursor concentration, as long as the concentration of hypophosphite is the same. This is consistent with the nucleation stage of growth and with the type of growth process observed, in that hypophosphite is the driving force in nucleation, whereas Pd precursor concentration is the key parameter affecting particle growth. (2) The number of Pd particles decreases with increasing hypophosphite concentration, which provides further insight into how the reduced Pd atoms form nuclei.

Based on these findings, we can take a closer look at the formation of the Pd nuclei. If all of the initial hypophosphite-reduced Pd atoms behave as nuclei, there should be a higher number of particles for the higher hypophosphite concentration series. However, *higher* hypophosphite concentration resulted in a *lower* number of particles or nuclei, suggesting that there was significant clustering of the hypophosphite-reduced Pd atoms at the very early stage of growth. Thus, we hypothesize that initial Pd nuclei were formed by the rapid clustering of Pd atoms.

Based on the SAXS and ICP results shown in Figures 5.2 through 5.6, we propose a mechanism for the growth of Pd nanoparticles through the chemical reduction of Pd precursor with sodium hypophosphite under pristine conditions

without supports or capping agents. As shown in Figure 5.10, our proposed mechanism begins with the rapid initial reduction of Pd precursor by the reducer, forming nuclei composed of hypophosphite-reduced Pd atoms. This nucleation step is followed by the further growth of Pd particles through conversion of Pd precursor ions to Pd particles, then slight further growth by agglomeration of already-formed particles, and finally the aggregation and sedimentation of these particles.

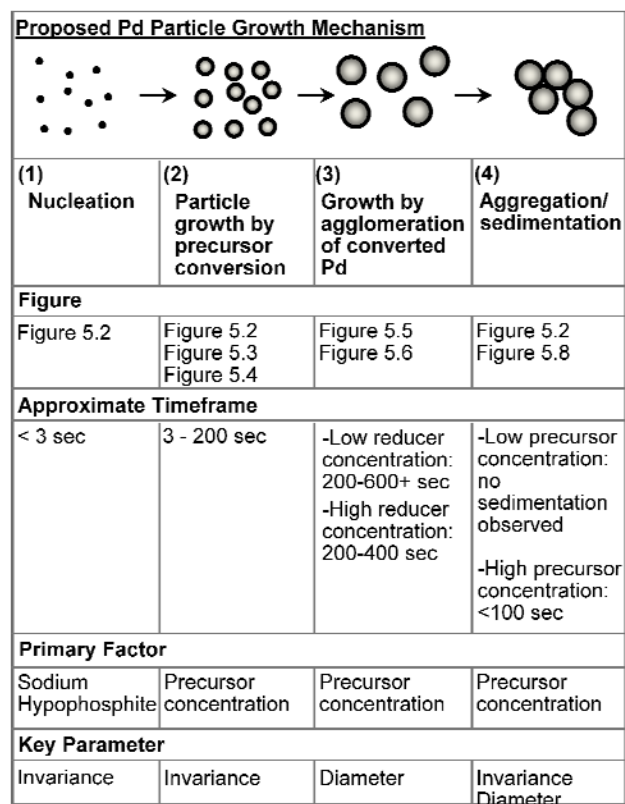


Figure 5.10: Proposed Four-step Pd Nanoparticle Growth Mechanism: (1) nucleation, (2) particle growth by conversion of Pd precursor, (3) slight further growth by agglomeration of Pd nanoparticles and (4) aggregation/sedimentation.

First, the rapid formation of initial particle nuclei (Step 1) is inferred based on the rapid increase in the Invariant (Q) for all samples within a few seconds (Figure 5.2). Also, the lower number of Pd particles for higher reducer concentration samples indicates that Pd atoms agglomerate to form Pd nuclei (Figure 5.5). Although the size of the nuclei was not easily measured with this setup due to the rapid initial formation and low initial amount of particles, we hypothesize that the formation of nuclei is driven primarily by sodium hypophosphite, since no particles were formed in the absence of sodium hypophosphite (data not shown).

Next, we observe the growth of Pd particles (Step 2) through the reduction of Pd precursor ions to Pd nanoparticles. We hypothesize that this step is driven by the known autocatalytic nature of Pd and the electroless deposition process, based on the Q measurements, where conversion increased until reaching a maximum before 200 seconds, regardless of the hypophosphite concentration (Figure 5.2). We observe higher conversion (Q_{max}) of precursor to Pd particles with higher Pd precursor concentration (Figure 5.3). This hypothesis was further confirmed via ICP measurements, where reduction of Pd precursor was significantly higher than expected for direct reduction by hypophosphite based on the 35% efficiency of the chemical reduction mechanism (Equations 5.4-5.10). Also, the most significant change in particle size occurs during this period of time (prior to 200 seconds) (Figure 5.5), where the final size increases with increasing Pd concentration (Figure 5.6). This key growth step may be driven by the known

autocatalytic nature of Pd, where Pd precursor molecules may attach to Pd nuclei and then are reduced on the particle surface. The reduced Pd atom may then become part of the growing facet of the particle.[88]

We next observed the growth of Pd particles through the agglomeration (i.e. the formation of individual particles from several particles) of previously formed particles (Step 3). Growth of the Pd nanoparticles (Figure 5.5) continued after conversion had ceased in most cases (Figure 5.2). Since no new scattering material (in this case, Pd particles) was being formed during this stage (no increase in Q), growth of particles is attributed to the agglomeration of smaller Pd particles to form larger particles. Although the particle size increase through agglomeration was minor even for the highest Pd precursor concentration samples and occurred very slowly as compared to the initial nucleation process, it indicates that there is additional growth possible in later stages. We attribute this agglomerative growth to oriented attachment, rather than Ostwald Ripening (5.7). We hypothesize that sodium hypophosphite does not play a significant role in the acceleration of this stage, where we observe that the maximum particle diameter is reached earlier in formation (i.e. less than 200sec) for higher hypophosphite concentration samples (Figure 5.5). Additionally, for some samples in the low hypophosphite concentration series (Figure 5.5(a)), the maximum particle diameter was not reached within our measurement timeframe.

Finally, in high Pd precursor concentration samples, we observed the aggregation (clustering of many individual particles into an insoluble form) and sedimentation of the Pd nanoparticles (Step 4, Figure 5.2). First, we observed (by eye) large particle “clumps” in the capillary and stuck to the capillary walls at the end of the experiment for high Pd precursor concentration samples, as well as with TEM (Figure 5.8). Also, the “clumping” of particles was confirmed by the decrease in Q after 100 seconds for high Pd precursor concentration samples (Figure 5.2). As confirmed by TEM studies (Figure 5.8) and by the particle size measurements (Figures 5.5-5.6), the aggregates consisted of individual particles that had retained their size and shape, indicating that both later stage events do not significantly alter the size and number of particles.

5.3 Conclusions

In comparison to other well known growth mechanisms, we found the most similarity to the Finke-Watzky Four-Step Mechanism for select transition metals in certain conditions,[90] where the authors observed particle growth beginning with the initial formation of nuclei, followed by autocatalytic growth, bimolecular aggregation and finally autocatalytic agglomeration. However, in contrast to the Finke-Watzky Mechanism where particle nucleation was slow and measureable, we observed extremely rapid particle nucleation (within 3 seconds). Although we similarly observed two types of growth, we note that agglomeration is not a significant growth process in our system. In comparison to the well

known Ostwald Ripening mechanism, we postulate that particle growth in our system does not follow this mechanism. Specifically, Ostwald Ripening growth involves the formation of larger particles at the expense of smaller particles, resulting in increased uniformity for larger particle populations as compared to smaller particles, which is in direct contrast to our observations.

In this chapter, we present the thorough examination of the growth of Pd nanoparticles in pristine conditions using *in situ* SAXS, and infer a possible four-step growth mechanism consisting of rapid nucleation and particle growth followed by slight growth by agglomeration and then aggregation/sedimentation. Combined, the results presented show that *in situ* SAXS can be employed to thoroughly examine rapid and dynamic nanoscale phenomena in pristine conditions and that valuable fundamental information such as size, size distribution and conversion can be readily extracted. We envision that the particle growth mechanism and key parameters identified here may be useful in the tailoring and control of nanoparticle sizes and their distributions in a wide range of systems.

6 *IN SITU* SAXS ANALYSIS OF PALLADIUM

NANOPARTICLE GROWTH ON TMV1CYS TEMPLATES

One of the key goals in nanotechnology is the precise and controllable fabrication of nanoscale structures with tunable functionality. Biological supramolecules, viruses in particular, have gained significant attention as templates for nanoscale material fabrication toward a variety of applications, ranging from quantum dots to catalytic nanoparticles. TMV in particular has been extensively enlisted as a template for various nanoparticle syntheses, however these studies have been limited to demonstration based on *ex situ* TEM, and as a result there is limited fundamental knowledge on the utility and role of the viral templates on the particle growth. Therefore, a critical need exists in unraveling the role of viral templates in particle growth, leading toward a fundamental understanding and more efficient utilization of these templates for facile nanoparticle design and synthesis strategies.

Although previous works have elucidated several important reaction parameters that affect particle formation on these viral nanotemplates, these studies have been limited to *ex situ* demonstrations of particle formation. In contrast, our approach harnesses *in situ* SAXS to thoroughly examine the growth of Pd nanoparticles on the surface of TMV1cys nanotemplates, and to elucidate the role of TMV1cys in particle formation. In this chapter, we examine the

growth of palladium (Pd) nanoparticles on TMV1cys templates via *in situ* SAXS. Specifically, Pd precursor solution (Na_2PdCl_4) and sodium hypophosphite (NaPH_2O_2) reducer solution containing TMV1cys were co-flown and mixed in a quartz capillary, and the 2-D SAXS images recorded throughout particle growth, as shown in the schematic diagram of Figure 6.1(a).

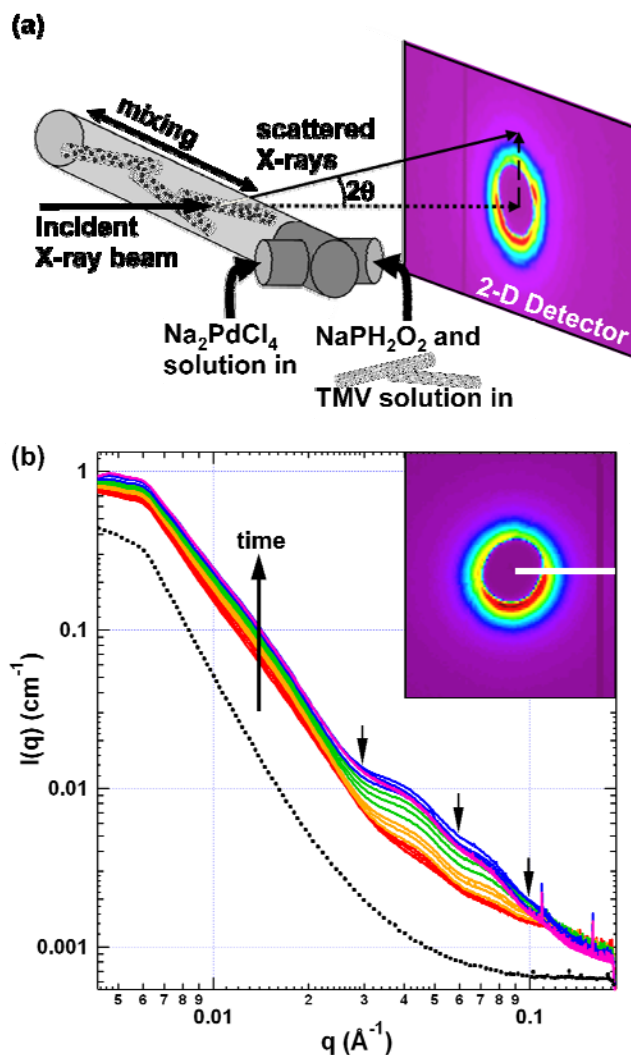


Figure 6.1: (a) Schematic diagram of *in situ* SAXS setup. Pd precursor solution (Na_2PdCl_4) and sodium hypophosphite (NaPH_2O_2) solution containing TMV1cys are fed into a quartz capillary and constantly mixed, forming Pd nanoparticles. The incident X-ray beam penetrates the quartz capillary, and the scattered rays are recorded at low angles on a 2-D CCD detector. (b) Typical *in situ* scattering curves of Pd nanoparticle growth on TMV1cys, acquired by making a line cut of intensity (inset) and plotting intensity as a function of the scattering vector q .

The SAXS images were then analyzed by making a linecut of intensity (shown by the white line in Figure 6.1(b) inset) and plotting the intensity as a function of the scattering vector, to create scattering curve plots. The representative scattering curves, shown in Figure 6.1(b), enable the in-depth examination of the dynamic behavior of TMV-templated nanoparticle formation. The *in situ* SAXS results show that TMV1cys provides templating sites for Pd nanoparticle growth as no particle growth was observed in the bulk solution. Additionally, Pd particles were smaller when formed on the TMV1cys templates as compared to the larger particles formed in the absence of TMV1cys templates. Finally, the coating density of Pd particles on the TMV1cys surfaces was tunable based on Pd precursor concentration with minimal influence by the reducer concentration. The results shown in this paper elucidate the fundamental role and utility of viral templates for smaller and uniform Pd nanoparticle formation. We envision that the results presented here will be valuable in furthering the fundamental understanding of how to control and tailor these nanoscale entities for a wide range of applications.

6.1 Materials and Methods

6.1.1 Materials

Sodium tetrachloro-palladate (II) (Na_2PdCl_4) was used as the Pd precursor for Pd nanoparticle formation (Sigma-Aldrich, St. Louis, MO). Precursor reduction was conducted using sodium hypophosphite (Sigma-Aldrich).

TMV1cys was generously provided by Dr. James Culver at the University of Maryland Biotechnology Institute, Center for Biosystems Research.

6.1.2 Pd Nanoparticle Formation on TMV1cys

Pd nanoparticles were formed by reducing Pd precursor with sodium hypophosphite in the presence of TMV1cys. Equal volumes (30 μ l each) of the precursor solution and the reducer solution, which contained 300 μ g/ml TMV1cys, were loaded into separate tubing, and then mixed by flowing the two solutions through a Y-shaped connector into a quartz capillary. SAXS patterns were recorded every three seconds, where the initial measurement was recorded as the two solutions mixed in the capillary. The precursor/reducer/TMV1cys solution was mixed throughout particle growth by flowing the solution in and out of the capillary.

6.1.3 *In situ* Small-Angle X-ray Scattering

SAXS measurements were conducted at the Advanced Photon Source (Argonne National Lab, Argonne, IL) 12 ID-C beamline. The incident X-rays, with energy of 12 keV, were irradiated on the sample in a quartz capillary. The scattered rays at small angles (less than 2 $^{\circ}$) were recorded on a 2-D CCD detector, as shown in Figure 6.1(a), with a sample to detector distance of approximately 2 meters.

6.1.4 Transmission Electron Microscopy (TEM)

Pd nanoparticles were formed by mixing precursor solution and reducer solution containing 300 $\mu\text{g/ml}$ TMV1cys for ten minutes under constant mixing by pipette. 5 μl of solution was placed on a copper TEM grid (Electron Microscopy Sciences, Hatfield, PA), and allowed to sit for two minutes. The grid was then placed on filter paper to wick away the liquid. TEM samples were probed with a JEOL-2100 High Resolution TEM at the Center for Nanoscale Systems (CNS) at Harvard University.

6.2 Results and Discussion

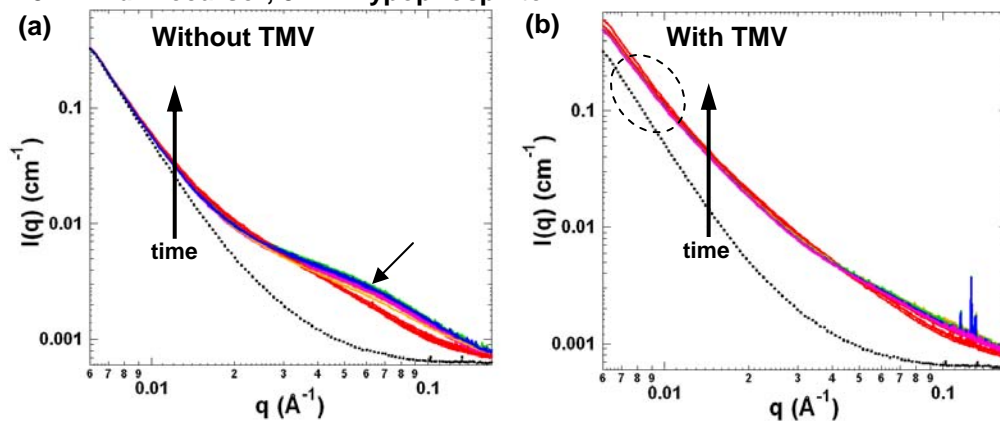
6.2.1 Comparison of Pd Nanoparticle Growth in the Presence and Absence of TMV1cys

First, Figure 6.1(b) shows characteristic *in situ* scattering curves for palladium (Pd) nanoparticle formation on the TMV1cys templates. For this, a linecut of intensity (Figure 6.1(b) inset) is made, then intensity is plotted versus the scattering vector, q , where $q = \frac{4\pi \sin \theta}{\lambda}$. First, the dotted black line shows background scattering from water and TMV1cys. Typically, the scattering curve of TMV exhibits oscillation features,[73] which are characteristic of monodisperse scattering objects;[70] in this case the monodisperse cross section of TMV. However, the oscillations are not visible in the background scattering

curve because the concentration of TMV1cys used in this experiment was very low (300 μ g/ml as compared to 5mg/ml used in Reference [91]).

The colored curves represent measurements made during Pd particle formation on TMV1cys. First, the bottom red line (first measurement made 3 seconds after mixing) increases in intensity from the background scattering curve, indicating a higher amount of scattering material present. Slight oscillations are visible early in growth, however as time progressed these oscillations became more apparent (minima shown by the three small arrows). The distinct oscillations observed for the later measurements (green, blue and pink) arise from the coating of TMV1cys with Pd particles, and indicate three important conclusions. First, particle formation occurs only on the TMV1cys surface and not in the bulk solution, otherwise a broad particle scattering feature would be observed (as observed later in the absence of TMV in Figure 6.2(a) and (c)). Second, the Pd particles on TMV1cys are highly uniform; otherwise the TMV structure would lose its monodispersity, thus scattering curve oscillations would disappear. Finally, the Pd particles are very small (\leq about 5nm), otherwise the spherical particle scattering would dominate over the TMV rod scattering and the oscillations would no longer be visible. In summary, the representative scattering curve plot shown in Figure 6.1(b) indicates that *in situ* SAXS can be enlisted to examine the dynamic behavior of TMV-templated Pd nanoparticle formation.

1.5mM Pd Precursor, 5mM Hypophosphite



5mM Pd Precursor, 2.5mM Hypophosphite

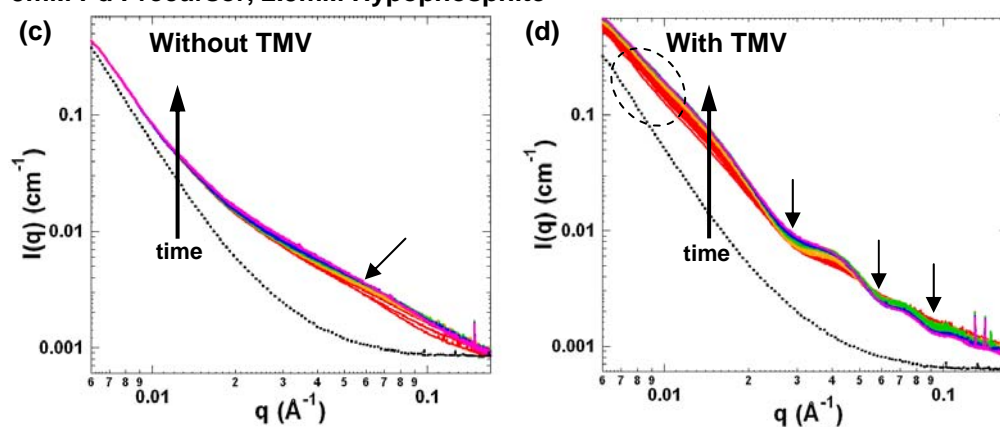


Figure 6.2: Comparison of *in situ* SAXS curves for particles formed in 1.5mM Pd precursor and 5mM hypophosphite (a) without TMV1cys and (b) with TMV1cys, and in 5mM Pd precursor and 2.5mM hypophosphite (a) without TMV1cys and (b) with TMV1cys.

As shown in the *in situ* SAXS curve plots of Figure 6.2, we next demonstrate that Pd nanoparticle growth is significantly different in the presence of TMV1cys templates. Scattering curve plots of four samples (particles formed in two conditions, both in the presence and absence of TMV1cys) were created by making a linecut of intensity (Figure 6.1(b), inset) and plotting intensity, $I(q)$, versus the scattering vector, q , for all measurements during particle growth (600 seconds).

First, Figure 6.2(a) shows scattering curves of Pd nanoparticles formed in 1.5mM Pd precursor in the absence of TMV1cys. The black dotted line represents background scattering from water. As time progressed, the scattering intensity increased, indicating an increase in the amount of scattering species present. A bump-like scattering feature is observed (denoted by an arrow), indicating the presence of polydisperse scattering objects, Pd nanoparticles in this case. The location of this bump feature, q^* , is related to the size of the particles, where diameter can be estimated using the Bragg equation: $d=2\pi/q^*$. [71] Here, we observe a bump feature centered at $q^*=0.07\text{\AA}^{-1}$, indicating approximately 9nm diameter particles.

In comparison, Figure 6.2(b) shows scattering curves of Pd nanoparticles formed with 1.5mM Pd precursor in the presence of TMV1cys templates. First, the black dashed line represents background scattering from water and TMV1cys, where no characteristic TMV scattering oscillations are observed due to the dilute

TMV1cys concentration used. The increased intensity of the scattering curve at low q (denoted by the dashed circle) indicates the formation of an atomic layer coating of Pd on the TMV templates. We draw this conclusion because the characteristic TMV scattering curve is typically higher in intensity at low q ; thus the presence of this scattering feature indicates that the TMVs are "visible" to SAXS and must be coated with Pd. However, the lack of oscillations (as observed in Figure 6.1(b)) indicates that there is very little Pd on the TMV templates. Additionally, we do not observe significant growth of particles in the bulk, because there is no bump-like scattering feature, as observed in the sample without TMV1cys in Figure 6.2(a).

Next, Figure 6.2(c) shows scattering curves for Pd nanoparticles formed in 5mM Pd precursor in the absence of TMV1cys. Pd particles formed over time, as evidenced by the increase in intensity during growth and the formation of a bump-like scattering feature. In this sample, the bump feature (denoted by an arrow) is centered at $q^*=0.05\text{\AA}^{-1}$, indicating the presence of approximately 12nm particles.

Finally, Figure 6.2(d) shows *in situ* scattering curves for Pd nanoparticles formed on TMV1cys with 5mM Pd precursor. The first measurement recorded (shown in red, measured 3 seconds after mixing) shows clear oscillations, where the minima are denoted by arrows. The presence of these oscillations indicates that the TMV1cys surface is coated with highly scattering Pd particles, since uncoated TMV did not produce scattering curve oscillations at the concentration

(300 μ g/ml) employed in this study. Similar to Figure 6.2(b), the increased intensity at low q , shown by the dashed circle, indicates that particles formed on the TMV templates and not in solution. As time progressed, the overall scattering intensity increased, indicating the formation of more Pd particles on the TMV1cys templates, and the minima locations shifted slightly to lower q . As shown in the scattering curve simulations in Figure 6.6 (Section 6.2.3), this shift in oscillation minima location is due to an increase in the rod diameter, thus an increase in Pd particle size. As described in Figure 6.1(b), in order for the oscillations to be visible, the Pd particles on the TMV1cys surface must be (1) relatively uniform and (2) small (5nm or less). Additionally, it is clear that Pd particles do not grow significantly in the bulk solution, as evidenced by the lack of a bump-like scattering feature (observed in Figures 6.2(a) and (c)) which would diminish the TMV's characteristic oscillations.

Combined, these results demonstrate that the growth of Pd nanoparticles is significantly different in the presence of TMV1cys. We observe large particles formed in solution in the absence of TMV; 9nm and 12nm particles for 1.5mM and 5mM Pd precursor, respectively. In contrast, we observe light coating of Pd (size less than is measureable with SAXS, approximately 1nm) on TMV1cys at low Pd precursor concentration, and the formation of small uniform particles on the surface of TMV1cys at higher Pd precursor concentration. Importantly, it is clear that the Pd nanoparticle growth mechanism is significantly different in the presence of TMV1cys, as we observe no Pd particle growth in the bulk solution

when TMV1cys is present. In other words, the *in situ* SAXS results in Figure 6.2 confirmed that TMV1cys does provide template sites for Pd nanoparticle growth.

6.2.2 Effect of Reaction Parameters on Pd Nanoparticle Growth

We next examine the effect of two parameters on Pd particle growth on TMV1cys templates; Pd precursor concentration in Figure 6.3 and sodium hypophosphite concentration in Figure 6.4. First, staggered *in situ* SAXS curves of Figures 6.3(a) to (c) show Pd nanoparticle formation with varying Pd precursor concentration (1-5mM) with identical hypophosphite (5mM) and TMV1cys (300 μ g/ml) concentrations.

The first scattering curve (bottom red curve, 3 seconds) in Figure 6.3(a) shows a slight overall change of curve shape as compared to the background scattering curve (dotted line) indicating the formation of a small amount of scattering material. Throughout growth, the shape of the scattering curves remained unchanged, indicating that no significant growth occurred after 3 seconds. As shown in the scattering curve simulations in Figure 6.7 (Section 6.2.3), when the amount of Pd on the TMV templates increases, the TMV scattering intensity also increases, resulting in more oscillations visible over the background scattering from water. In this case, the scattering curve shape resembled that of TMV and not the background; however no oscillations were observable at any time points, indicating that the TMV's were not highly

scattering, and thus not densely coated with Pd. Additionally, measureable particles were not formed in the bulk solution, as evidenced by the lack of bump-like nanoparticle scattering features as in Figures 6.2(a) and (c).

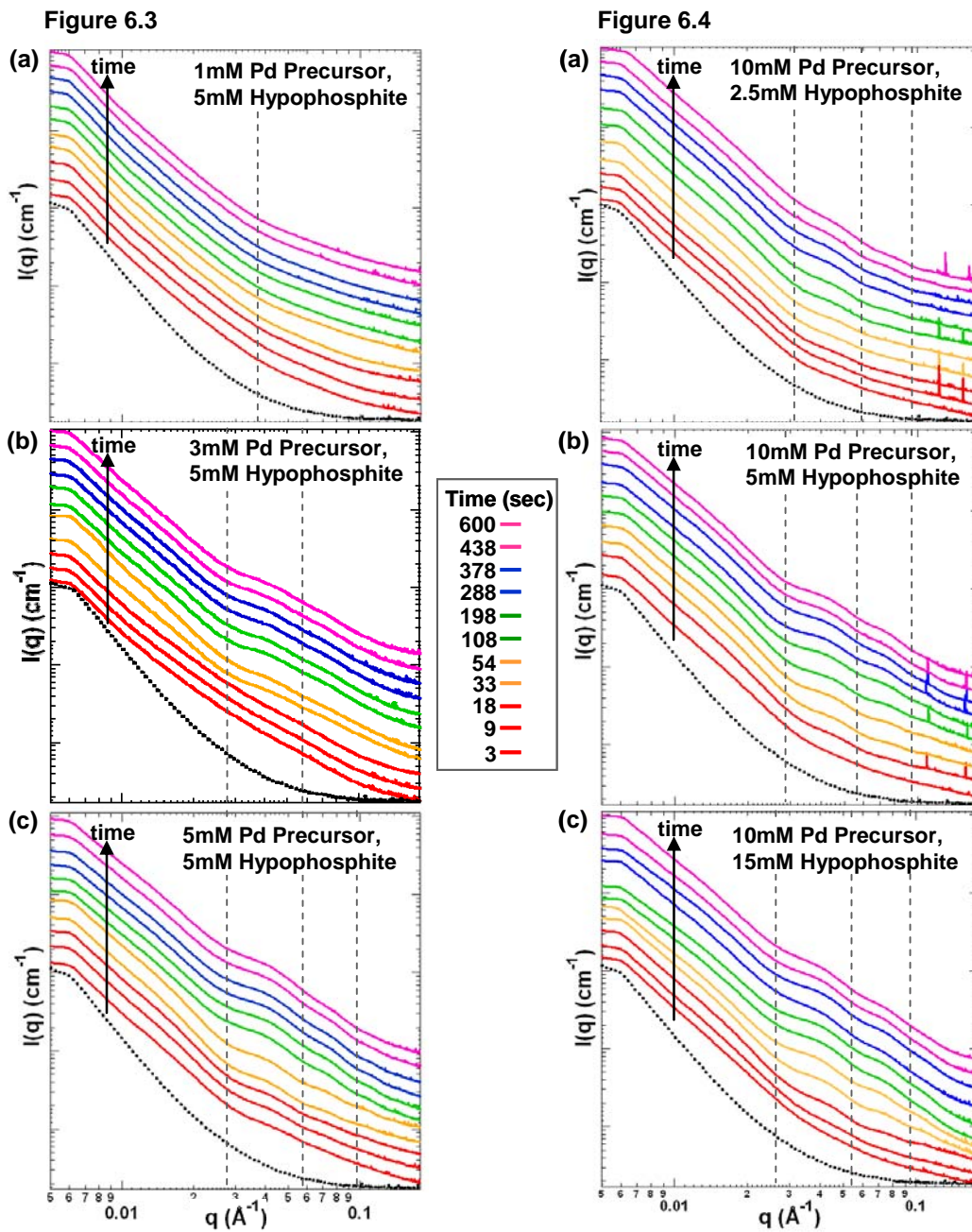


Figure 6.3: Staggered *in situ* SAXS curves for Pd nanoparticles formed on TMV1cys in 5mM hypophosphite and (a) 1mM, (b) 3mM, or (c) 5mM Pd precursor.

Figure 6.4: Staggered *in situ* SAXS curves for Pd nanoparticles formed on TMV1cys in 10mM Pd precursor and (a) 2.5mM, (b) 5mM, or (c) 15mM hypophosphite.

Next, Figure 6.3(b) shows Pd nanoparticle formation on TMV1cys in 3mM Pd precursor. Similar to Figure 6.3(a), early time points (3-18 seconds) show a slight change in curve shape from the background curve, indicating the formation of scattering material. However, after 33 seconds, more oscillation features appear, with two visible minima located at approximately 0.028 and 0.06 \AA^{-1} , indicated by the dashed vertical lines. These defined minima, with a slight shift in location, indicate that Pd particles have formed on the TMV templates and do not grow significantly after 33 seconds.

Finally, Figure 6.3(c) shows Pd nanoparticle growth on TMV1cys using 5mM Pd precursor and 5mM hypophosphite. In this case, one oscillation minima at 0.03 \AA^{-1} (shown by the left-most dashed line) is observable for the first measurement point (3 seconds). As time progressed, more oscillations became visible at 0.028, 0.06 and 0.1 \AA^{-1} , and became more defined, indicating that the TMV templates became more densely coated with Pd nanoparticles. Additionally, the location of the oscillation minima shifted slightly to lower q throughout growth, indicating an apparent increase in the rod diameter (i.e. shift of minima locations shown in the simulated scattering curves of Figure 6.6, Section 6.2.3), thus growth of the Pd nanoparticles.

Combined, the results in Figure 6.3 show that Pd precursor concentration affects the coating of Pd nanoparticles on the surface of the TMV templates. The appearance of more defined oscillations at higher Pd precursor concentrations

indicates that the TMV templates are more densely coated with scattering Pd at higher Pd concentrations. Additionally, it is clear that particle growth occurred more rapidly at higher Pd precursor concentration, as shown by the appearance of oscillations earlier in growth. Importantly, the size of the Pd nanoparticles formed in the 3mM and 5mM samples were nearly identical, as evidenced by the similar locations of the oscillation minima.

Figure 6.4 shows staggered *in situ* scattering curve plots for samples prepared in various hypophosphite concentrations with identical Pd precursor (10mM) and TMV1cys (300 μ g/ml) concentrations. First, Figure 6.4(a) shows staggered scattering curve plots of Pd nanoparticles formed on TMV1cys in 2.5mM hypophosphite. Similar to the scattering curves in Figure 6.3(c), oscillations began to appear within 3 seconds, as shown by the vertical dashed lines, indicating the rapid formation of Pd particles on TMV1cys templates. The three visible oscillation minima, at 0.03, 0.06 and 0.1 \AA^{-1} , became more defined during growth, indicating that the coating of Pd particles on TMV became denser.

Next, scattering curve plots for Pd nanoparticles formed in 5mM hypophosphite are shown in Figure 6.4(b). As with Figure 6.4(a), three oscillation minima are observable at approximately 0.028, 0.058 and 0.1 \AA^{-1} within 18 seconds indicating rapid formation of Pd particles on the TMV1cys templates. The slight shift in minima location, as compared to Figure 6.4(a), indicates that the rod diameter is larger, as shown by the rod diameter simulations

in Figure 6.6 (Section 6.2.3). This increase in rod diameter thus indicates an increased Pd nanoparticle size.

Finally, Figure 6.4(c) shows scattering curve plots for Pd nanoparticles formed on TMV1cys with 15mM hypophosphite. The scattering curves show distinct oscillation minima at approximately 0.026, 0.055 and 0.1 \AA^{-1} ; which are shifted slightly as compared to Figures 6.4(a) and (b). This indicates that Pd particles are slightly larger in this sample, as compared to those at lower hypophosphite concentration.

It is clear from the results in Figure 6.4 that hypophosphite concentration plays a minor role in particle growth, slightly influencing the particle size. The clear shift in minima location to lower q with increasing hypophosphite concentration indicates an increase in particle size, however it is important to note that this shift is slight, and as a result the particle size difference is minimal. Finally, hypophosphite concentration plays no significant role in the amount of Pd coated on the TMV1cys templates, as shown by the similarly distinct oscillation minima in all three samples.

Finally, we confirm the *in situ* SAXS-based observations in Figures 6.1-6.4 using *ex situ* Transmission Electron Microscopy (TEM) as shown in Figure 6.5. For this, Pd nanoparticles were formed on TMV1cys templates by mixing equal volumes of Pd precursor solution and hypophosphite solution containing

300 $\mu\text{g/ml}$ TMV1cys with continuous pipetting. 10 μl of the solution was then allowed to sit on a TEM grid, then the water wicked away with filter paper and the sample examined via TEM.

First, Figure 6.5(a) shows Pd nanoparticles formed on TMV1cys using 1.5mM Pd precursor and 15mM hypophosphite. The TEM image clearly shows that a few small particles were formed on the TMV templates at this low concentration of Pd precursor. Next, Pd nanoparticles formed on TMV1cys in 3mM Pd precursor and 15mM hypophosphite are shown in Figure 6.5(b). A denser coating of Pd nanoparticles is clearly observable, as compared to the few particles on TMV1cys at lower Pd precursor concentration in Figure 6.5(a). Figure 6.5(c) shows the increased coating of Pd nanoparticles on TMV1cys templates, compared to Figures 6.5(a) and (b), when formed in 5mM Pd Precursor and 5mM hypophosphite, as shown previously in Figure 6.3(c).

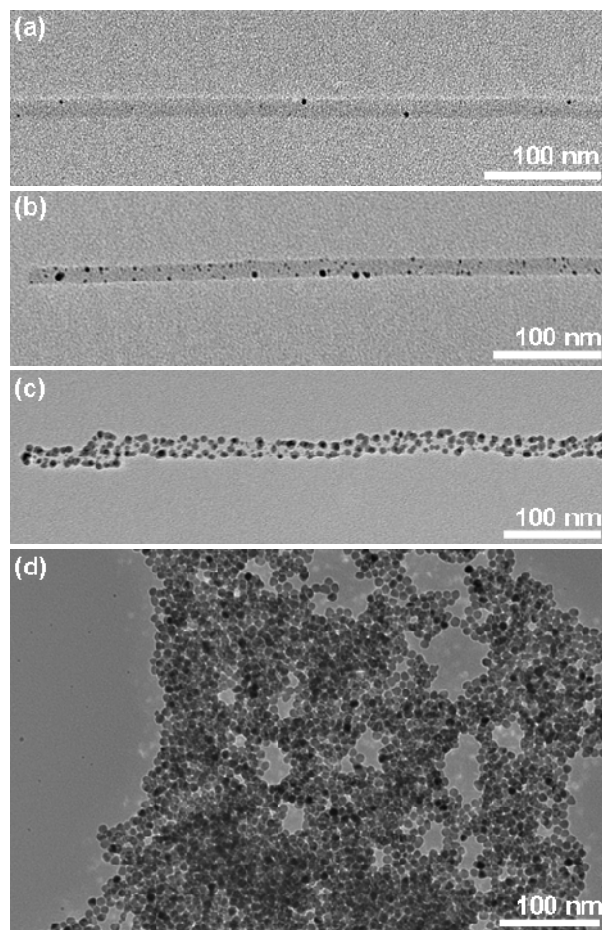


Figure 6.5: Transmission Electron Microscopy (TEM) images of Pd nanoparticles formed on TMV1cys in (a) 1.5mM Pd precursor, 15mM hypophosphite, (b) 3mM Pd precursor, 15mM hypophosphite, and (c) 5mM Pd precursor, 5mM hypophosphite. (d) TEM image of Pd nanoparticles formed in the absence of TMV1cys in 5mM Pd precursor, 5mM hypophosphite.

It is clear from these results that the amount of Pd nanoparticles formed on the TMV1cys templates is tunable based on Pd precursor concentration; where higher Pd precursor concentration resulted in higher density of Pd nanoparticles formed on the TMV templates (as observed with SAXS in Figure 6.3). The TEM images also show that particles formed on the TMV templates were 5nm or less in diameter, as observed using SAXS (Figure 6.1(b)). Importantly, very few Pd nanoparticles were formed in the bulk solution, further confirming the SAXS-based observations (Figures 6.1 and 6.2).

Finally, we confirm the difference in Pd particle formation in the absence of TMV1cys using *ex situ* TEM. For this, Pd nanoparticles were made by mixing equal volumes of 5mM Pd precursor and 5mM hypophosphite by continuous pipetting. As compared to the identical growth conditions in the presence of TMV templates shown in Figure 6.5(c), Pd particles grown in the absence of TMV are significantly larger; 12nm vs. 5nm or less on TMV1cys. Importantly, this result confirms that the TMV templates play a significant role in the formation of Pd nanoparticles, as shown in Figure 6.2. Additionally, Pd nanoparticles formed in the absence of TMV templates aggregated significantly, as opposed to those grown on the TMV templates which were well dispersed on the TMV surface.

Although we have previously demonstrated the utility of Pd nanoparticles formed on these TMV templates [48], these results confirm our SAXS based observations

of Pd nanoparticle coating behavior in Figures 6.3 and 6.4, and demonstrate that the TMV templates play a significant role in Pd nanoparticle formation.

6.2.3 Simulated Effect of Reaction Parameters on Pd Nanoparticle Growth

In order to better interpret our SAXS observations, we simulated theoretical conditions based on our hypotheses and compare the theoretical scattering behavior to our real data. First, we simulated scattering curves of hypothetical TMV's coated with different thicknesses of Pd nanoparticles. For this, we modeled scattering curves of rod-shaped particles with varying cross sectional diameter, as shown in Figure 6.6. The scattering curves were created using the model equation for monodisperse rod-shaped particles,[71] as shown in Equation 6.1; where $I(q)$ is the scattering intensity, q is the scattering vector, r_{rod} is the radius of the rod, r_{TMV} is the radius of the TMV rod, d is the thickness of the Pd particle coating, and J_1 is the Bessel function of the first kind.

$$I(q) = 2\pi r_{rod}^2 \frac{J_1(qr_{rod})}{(qr_{rod})}$$

(Equation 6.1)

$$r_{rod} = r_{TMV} + d$$

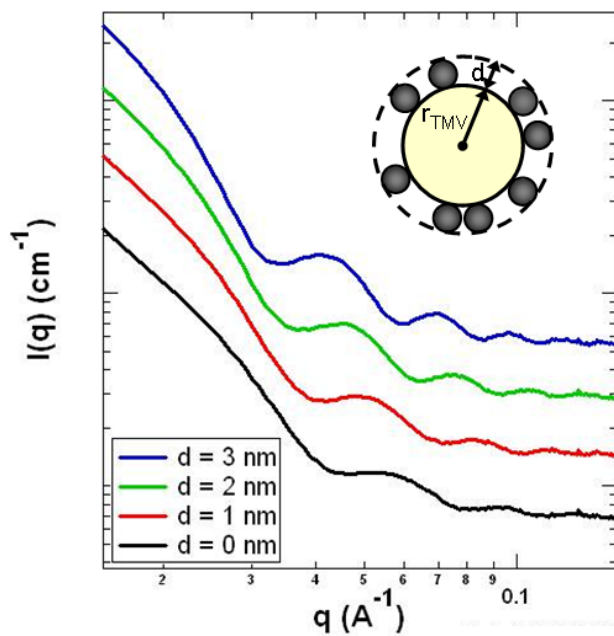


Figure 6.6: Modeled scattering curves of rod-shaped particles of various diameters, simulating the effect of increased coating thickness on TMV. Black: 18nm overall diameter, 0nm coating; red: 20nm overall diameter, 1nm coating; green: 22nm overall diameter, 2nm coating; blue: 24nm overall diameter, 3nm coating). Background scattering from water was added to the model scattering curves.

The simulated rod diameters were based on the 18nm diameter ($2r_{TMV}$) of the TMV rod (18nm diameter rod/0nm coating, bottom black line), plus a range of thicknesses of Pd nanoparticle coatings, d , (20 nm diameter rod/1nm coating, red line; 22nm diameter rod/2nm coating, green line; and 24nm diameter rod/3nm coating, blue line). The simulations assume complete coating of the TMV with a continuous, single-layer “film” of Pd particles. Background scattering from water was added to the model curves to simulate typical SAXS data of rod shaped particles in solution. First, Figure 6.6 confirms that in highly monodisperse systems, we observe oscillations in the scattering curves. Next, it is clear from Figure S1 that as the rod diameter increases, thus as particle size d increases, the oscillation minima shift towards lower q . This simulation suggests that the minima shift observed in Figures 6.1, 6.2, and 6.4 are a result of the increasing thickness of the Pd coating on TMV, thus growth of the Pd nanoparticles on the TMV surface.

We next simulate the effect of Pd particle coating density on the scattering curve data, as shown in Figure 6.7. For this, we first simulated model scattering curves of a 24nm diameter rod using the model rod-shaped particle scattering equation (Equation 6.1). To simulate increased amounts of Pd particles on the TMV surface, the intensity of the rod-shaped particle scattering curve was multiplied by various factors, since more Pd on the TMV surface theoretically results in higher scattering intensity. The simulated rod-shaped particle curve intensities ranged from 2 times (bottom maroon curve) to 300 times (top black

curve) the background scattering intensity. For these simulations, we assumed that the Pd nanoparticle coating was composed of a single layer of Pd particles of the same size on the TMV templates. In other words, we assumed identical rod diameter for all curves, resulting in identical minima locations. It is clear from Figure 6.7 that the scattering curve oscillations become more defined when the rod scattering produces a higher scattering intensity that is not diminished by the background scattering intensity; thus more Pd on the surface of TMV. Thus, this result suggests that the enhanced oscillations observed in Figure 6.3 were a result of increased coating of Pd nanoparticles on the TMV surface.

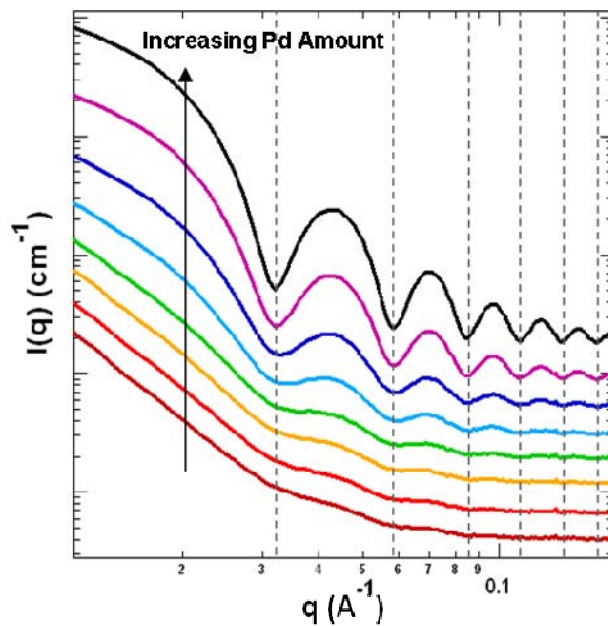


Figure 6.7: Modeled scattering curves simulating the effect of increased scattering intensity as a result of increased coating density on the TMV surface.

Model curves were multiplied by a range of factors as compared to the added background scattering from water; ranging from two times (bottom red curve) to 300 times (top black curve).

6.3 Conclusions

In this chapter, we examined the role of TMV1cys nanotemplates in Pd nanoparticle growth using *in situ* SAXS. First, we demonstrated that Pd nanoparticle growth was significantly different in the presence or absence of TMV1cys templates. Specifically, we observed that Pd particles formed directly on the TMV templates, and not in the bulk solution. Additionally, we observed that particles formed on the TMV1cys templates were significantly smaller than those formed in the absence of TMV1cys; 5nm or less vs. 12nm respectively. The coating of Pd nanoparticles on the TMV1cys templates was tunable, where the Pd particle coating density increased with increasing Pd precursor concentration. Increased sodium hypophosphite concentration resulted in slightly larger particles, however we note that this size difference was slight. Finally, we confirmed our SAXS based observations using TEM. Combined, these results demonstrate the value of *in situ* SAXS in examining dynamic changes in viral-nanoparticle hybrid structures, and provide insight into their growth. We believe that these results represent a significant step toward elucidating the fundamental mechanism of particle formation on these viral nanotemplates. We envision that these results will enable better controlled formation of functional viral-metal hybrid structures for a wide range of nanodevice applications such as catalysis, battery electrodes and sensors.

7 CONCLUSIONS

In summary, the results shown in this thesis demonstrate readily controllable palladium (Pd) nanoparticle formation on viral nanotemplates, through the electroless deposition of Pd precursor with a weak reducing agent, sodium hypophosphite.

First, we demonstrated that Pd nanoparticles preferentially formed on surface assembled genetically modified Tobacco Mosaic Virus (TMV1cys) in high density. Grazing Incidence Small-Angle X-ray Scattering (GISAXS) studies showed that particle size was tunable (4-18nm), simply by modulating hypophosphite concentration. This result highlighted simplicity of our controllable Pd nanoparticle formation method using TMV nanotemplates.

We then examined the dynamic behavior of these viral-metal entities, by conducting a thermal stability study using *in situ* Small-Angle X-ray Scattering (SAXS). We showed that the stability of both the surface assembled TMVs and Pd nanoparticles were enhanced by each other, and that the degradation of the Pd particles and TMV were coupled. These results confirm the utility of the TMV nanotemplate in stabilizing the Pd nanoparticles as compared to particles formed directly on the substrate surface.

Finally, we examined the growth of Pd nanoparticles in solution in the presence and absence of TMV1cys templates in order to gain insight into the role of TMV templates in Pd particle formation. First, we showed that Pd particle growth in the absence of TMV1cys templates was highly dependent on the Pd precursor concentration and particle size ranged from 4-13nm in diameter. Importantly, we show that the conversion yield is significantly higher than expected for many samples; conversion yield reached almost 100% in some cases when it was expected to be 58% or 17% based on the reaction equations. In comparison, we show the clear difference in particle growth on the TMV1cys templates, where particle size was consistently smaller; 5nm or less in diameter. Importantly, we show that Pd particles nucleate and grow on the TMV templates, and not in the bulk solution.

Upon closer examination, we acknowledge several key points. It is clear that Pd nanoparticles nucleate and grow on the surface of TMV1cys, presumably due to the high abundance of surface accessible thiol groups on the virus[43]. If we consider these thiol groups as possible Pd particle nucleation sites, we can draw several conclusions about the difference in particle size in the three different particle growth experiments. First, we observe that particles are larger in size on surface assembled TMV1cys than when formed on TMV1cys in solution; for example, 18nm vs. atomic sized, respectively in 0.5 mM Pd precursor and 5 mM hypophosphite. Additionally, we observe a significantly denser coating of Pd particles on surface assembled TMV1cys as compared to aqueous TMV1cys. We

hypothesize that this phenomenon could be due to the lower ratio of TMV1cys to Pd precursor and reducer in the surface assembled growth case as compared to solution growth case. In other words, with fewer nucleation sites and a higher volume of reagents, Pd precursor and reducer was in significant excess in the surface assembled TMV growth experiments, which could then lead to the formation of more large particles. Similarly, Pd nanoparticles formed in solution in the absence of TMV1cys were larger than those formed in solution in the presence of TMV1cys; for example, 12nm vs. 5nm, respectively. We hypothesize that the TMV1cys templates provide a high density array of nucleation sites enabling the formation of smaller, more dispersed Pd particles.

In conclusion, we believe that our simple TMV templated Pd nanoparticle formation approach, coupled with first-time in depth size and growth analysis using GISAXS and *in situ* SAXS, represents a significant advancement toward controlled metal nanoparticle growth. Additionally, we believe that these results represent a significant first step toward understanding the dynamic behaviors of viral-inorganic hybrid materials and nanodevices. The results of this work have been directly applied to current research endeavors furthering the use of viral-metal structures for catalysis applications.[66-69] We envision that these viral-metal entities can be further applied to a wide range of applications, such as batteries, sensors and nanoelectronics.

8 REFERENCES

1. Durand, J, Teuma, E, and Gomez, M, *An Overview of Palladium Nanocatalysts: Surface and Molecular Reactivity*. Eur J Inorg Chem, 2008. **23**: p. 3577-3586.
2. Forzatti, P and Groppi, G, *Catalytic combustion for the production of energy*. Catal Today, 1999. **54**(1): p. 165-180.
3. Kishore, S, Nelson, JA, Adair, JH, and Eklund, PC, *Hydrogen storage in spherical and platelet palladium nanoparticles*. J Alloys Compd, 2005. **389**(1-2): p. 234-242.
4. Lampert, JK, Kazi, MS, and Farrauto, RJ, *Palladium catalyst performance for methane emissions abatement from lean burn natural gas vehicles*. Appl Catal B, 1997. **14**(3-4): p. 211-223.
5. Pham-Huu, C, Keller, N, Ehret, G, Charbonniere, LJ, Ziessel, R, and Ledoux, MJ, *Carbon nanofiber supported palladium catalyst for liquid-phase reactions - An active and selective catalyst for hydrogenation of cinnamaldehyde into hydrocinnamaldehyde*. Journal of Molecular Catalysis a-Chemical, 2001. **170**(1-2): p. 155-163.
6. Navarro, O, Kaur, H, Mahjoor, P, and Nolan, SP, *Cross-Coupling and Dehalogenation Reactions Catalyzed by (N-Heterocyclic carbene)Pd(allyl)Cl Complexes*. J Org Chem, 2004. **69**(9): p. 3173-3180.
7. Vittorio, F, *High-Turnover Palladium Catalysts in Cross-Coupling and Heck Chemistry: A Critical Overview*. Adv Synth Catal, 2004. **346**(13-15): p. 1553-1582.
8. Xu, Y-H, Lu, J, and Loh, T-P, *Direct Cross-Coupling Reaction of Simple Alkenes with Acrylates Catalyzed by Palladium Catalyst*. J Am Chem Soc, 2009. **131**(4): p. 1372-1373.
9. Guibal, E and Vincent, T, *Chitosan-supported palladium catalyst. IV. Influence of temperature on nitrophenol degradation and thermodynamic parameters*. J Environ Manage, 2004. **71**: p. 15-23.
10. Omole, MA, K'Owino, IO, and Sadik, OA, *Palladium nanoparticles for catalytic reduction of Cr(VI) using formic acid*. Appl Catal B, 2007. **76**: p. 158-167.
11. Nguyen, K, Monteverde, M, Filoramo, A, Goux-Capes, L, Lyonnais, S, Jegou, P, Viel, P, Goffman, M, and Bourgoin, J-P, *Synthesis of Thin and Highly Conductive DNA-Based Palladium Nanowires*. Adv Mater, 2008. **20**: p. 1099-1104.
12. Richter, J, Seidel, R, Kirsch, R, Mertig, M, Pompe, W, Plaschke, J, and Schackert, HK, *Nanoscale Palladium Metallization of DNA*. Adv Mater, 2000. **12**(7): p. 507-510.
13. Guo, S and Dong, S, *Biomolecule-nanoparticle hybrids for electrochemical biosensors*. Trends Anal Chem, 2009. **28**(1): p. 96-109.

14. Teranishi, T and Miyake, M, *Size Control of Palladium Nanoparticles and Their Crystal Structures*. Chemistry of Materials, 1998. **10**(2): p. 594-600.
15. Li, Y, Boone, E, and El-Sayed, MA, *Size Effects of PVP-Pd Nanoparticles on the Catalytic Suzuki Reactions in Aqueous Solution*. Langmuir, 2002. **18**(12): p. 4921-4925.
16. Li, Y and El-Sayed, MA, *The Effect of Stabilizers on the Catalytic Activity and Stability of Pd Colloidal Nanoparticles in the Suzuki Reactions in Aqueous Solution* The Journal of Physical Chemistry B, 2001. **105**(37): p. 8938-8943.
17. Balci, S, Bittner, AM, Hahn, K, Scheu, C, Knez, M, Kadri, A, Wege, C, Jeske, H, and Kern, K, *Copper nanowires within the central channel of tobacco mosaic virus particles*. Electrochim. Acta, 2006. **51**(28): p. 6251-6257.
18. Balci, S, Noda, K, Bittner, AM, Kadri, A, Wege, C, Jeske, H, and Kern, K, *Self-assembly of metal-virus nanodumbbells*. Angewandte Chemie-International Edition, 2007. **46**(17): p. 3149-3151.
19. Bigall, NC, Reitzig, M, Naumann, W, Simon, P, Pee, K-Hv, and Eychmuller, A, *Fungal Templates for Noble-Metal Nanoparticles and Their Application in Catalysis*. Angew Chem Int Ed, 2008. **47**(7876-7879).
20. Deplanche, K, Woods, RD, Mikheenko, IP, Sockett, RE, and Macaskie, LE, *Manufacture of Stable Palladium and Gold Nanoparticles on Native and Genetically Engineered Flagella Scaffolds*. Biotechnol Bioeng, 2008. **101**(5): p. 873-880.
21. Gu, Q, Cheng, C, and Haynie, DT, *Cobalt metallization of DNA: toward magnetic nanowires*. Nanotechnol, 2005(8): p. 1358.
22. Mertig, M, Ciacchi, LC, Seidel, R, and Pompe, W, *DNA as a Selective Metallization Template*. Nano Lett, 2002. **2**(8): p. 841-844.
23. Seeman, NC and Belcher, AM, *Emulating biology: Building nanostructures from the bottom up*. Proc Nat Acad Sci, 2002. **99**(Suppl 2): p. 6451-6455.
24. Seidel, R, Ciacchi, LC, Weigel, M, Pompe, W, and Mertig, M, *Synthesis of Platinum Cluster Chains on DNA Templates: Doncidtions for Template-Controlled Cluster Growth*. J Phys Chem B, 2004. **108**: p. 10801-10811.
25. Zhou, JC, Gao, Y, Martinez-Molares, AA, Jing, X, Yan, D, Lau, J, Hamasaki, T, Ozkan, CS, Ozkan, M, Hu, E, and Dunn, B, *Microtubule-Based Gold Nanowires and Nanowire Arrays*. Small, 2008. **4**(9): p. 1507-1515.
26. Douglas, T and Young, M, *Host-guest encapsulation of materials by assembled virus protein cages*. Nature, 1998. **393**(6681): p. 152-155.
27. Douglas, T and Young, M, *Viruses: Making Friends with Old Foes*. Science, 2006. **312**(5775): p. 873-875.
28. Lee, S-W, Mao, C, Flynn, CE, and Belcher, AM, *Ordering of Quantum Dots Using Genetically Engineered Viruses*. Science, 2002. **296**(5569): p. 892-895.

29. Mao, C, Flynn, CE, Hayhurst, A, Sweeney, R, Qi, J, Georgiou, G, Iverson, B, and Belcher, AM, *Viral assembly of oriented quantum dot nanowires*. Science, 2003. **100**(12): p. 6946-6951.
30. Nam, KT, Kim, D-W, Yoo, PJ, Chiang, C-Y, Meethong, N, Hammond, PT, Chiang, Y-M, and Belcher, AM, *Virus-Enabled Synthesis and Assembly of Nanowires for Lithium Ion Battery Electrodes*. Science, 2006. **312**(5775): p. 885-888.
31. Royston, E, Ghosh, A, Kofinas, P, Harris, MT, and Culver, JN, *Self-Assembly of Virus-Structured High Surface Area Nanomaterials and Their Application as Battery Electrodes*. Langmuir, 2008. **24**(3): p. 906-912.
32. Royston, E, Lee, S-Y, Culver, JN, and Harris, MT, *Characterization of silica-coated tobacco mosaic virus*. J Colloid Interface Sci, 2006. **298**(2): p. 706-712.
33. Tseng, RJ, Tsai, C, Ma, L, Ouyang, J, Ozkan, CS, and Yang, Y, *Digital memory device based on tobacco mosaic virus conjugated with nanoparticles*. Nat Nano, 2006. **1**(1): p. 72-77.
34. Wang, X, Niu, Z, Li, S, Wang, Q, and Li, X, *Nanomechanical characterization of polyaniline coated tobacco mosaic virus nanotubes*. J Biomed Mater Res A, 2008. **87A**(1): p. 8-14.
35. Culver, JN, *Tobacco Mosaic Virus Assembly and Disassembly: Determinants in Pathogenicity and Resistance*. Ann Rev Phytopathol, 2002. **40**: p. 287-308.
36. Pettersen, EF, Goddard, TD, Huang, CC, Couch, GS, Greenblatt, DM, Meng, EC, and Ferrin, TE, *UCSF Chimera - A visualization system for exploratory research and analysis*. J Comput Chem, 2004. **25**(13): p. 1605-1612.
37. Namba, K, Pattanayek, R, and Stubbs, G, *Visualization of protein-nucleic acid interactions in a virus : Refined structure of intact tobacco mosaic virus at 2.9 Å resolution by X-ray fiber diffraction*. J Molec Biol, 1989. **208**(2): p. 307-325.
38. Bhat, TN, Bourne, P, Feng, Z, Gilliland, G, Jain, S, Ravichandran, V, Schneider, B, Schneider, K, Thanki, N, Weissig, H, Westbrook, J, and Berman, HM, *The PDB data uniformity project*. Nucleic Acids Res., 2001. **29**(1): p. 214-218.
39. Bromley, KM, Patil, AJ, Perriman, AW, Stubbs, G, and Mann, S, *Preparation of high quality nanowires by tobacco mosaic virus templating of gold nanoparticles*. J Mater Chem, 2008. **18**: p. 4796-4801.
40. Knez, M, Bittner, AM, Boes, F, Wege, C, Jeske, H, Mai, E, and Kern, K, *Bi-template Synthesis of 3-nm Nickel and Cobalt Nanowires*. Nano Lett, 2003. **3**(8): p. 1079-1082.
41. Knez, M, Sumser, M, Bittner, AM, Wege, C, Jeske, H, Martin, TP, and Kern, K, *Spatially Selective Nucleation of Metal Clusters on the Tobacco Mosaic Virus*. Adv Func Mater, 2004. **14**(2): p. 116-124.
42. Yi, HM, Nisar, S, Lee, SY, Powers, MA, Bentley, WE, Payne, GF, Ghodssi, R, Rubloff, GW, Harris, MT, and Culver, JN, *Patterned*

- assembly of genetically modified viral nanotemplates via nucleic acid hybridization*. Nano Letters, 2005. **5**(10): p. 1931-1936.
43. Lim, J-S, Kim, S-M, Lee, S-Y, Stach, EA, Culver, JN, and Harris, MT, *Quantitative study of Au(III) and Pd(II) ion biosorption on genetically engineered Tobacco mosaic virus*. J Colloid Interf Sci, 2010. **342**(2): p. 455-461.
 44. Ebner, M, Otto, H, and Werner, H, *Fragmentation and Recombination of CS₂ and CSSe in the Coordination Spher of Platinum Metals*. Angew Chem Int Ed, 1985. **24**(6): p. 518-519.
 45. Okeya, S, Kameda, K, Kawashima, H, Shimomura, H, Nishioka, T, and Isobe, K, *C=S Bond Fission in Coordinated Thioureas and Formation of a Sulfide-bridged Dinuclear Pd(II) Complex*. Chem Lett, 1995. **24**(7): p. 501-502.
 46. Lee, S-Y, Choi, J, Royston, E, Janes, DB, Culver, JN, and Harris, MT, *Deposition of Platinum Clusters on Surface-Modified Tobacco Mosaic Virus*. J Nanosci Nanotechnol, 2006. **6**: p. 974-981.
 47. Lee, S-Y, Royston, E, Culver, JN, and Harris, MT, *Improved metal cluster deposition on a genetically engineered tobacco mosaic virus template*. Nanotechnol, 2005. **16**: p. S435-S441.
 48. Tan, WS, Lewis, CL, Horelik, NE, Pregibon, DC, Doyle, PS, and Yi, H, *Hierarchical Assembly of Viral Nanotemplates with Encoded Microparticles via Nucleic Acid Hybridization*. Langmuir, 2008. **24**: p. 12483-12488.
 49. Yi, H, Rubloff, GW, and Culver, JN, *TMV Microarrays: Hybridization-Based Assembly of DNA-Programmed Viral Nanotemplates*. Langmuir, 2007. **23**(5): p. 2663-2667.
 50. Meulenkamp, EA, *Synthesis and Growth of ZnO Nanoparticles*. The Journal of Physical Chemistry B, 1998. **102**(29): p. 5566-5572.
 51. Magnuson, ML, Lytle, DA, Frietch, CM, and Kelty, CA, *Characterization of Submicrometer Aqueous Iron(III) Colloids Formed in the Presence of Phosphate by Sedimentation Field Flow Fractionation with Multiangle Laser Light Scattering Detection*. Analytical Chemistry, 2001. **73**(20): p. 4815-4820.
 52. Xiong, Y, Chen, J, Wiley, B, Xia, Y, Yin, Y, and Li, Z-Y, *Size-Dependence of Surface Plasmon Resonance and Oxidation for Pd Nanocubes Synthesized via a Seed Etching Process*. Nano Lett, 2005. **5**(7): p. 1237-1242.
 53. Robert J. Macfarlane, Lee, B, Hill, HD, Senesi, AJ, Seifert, S, and Mirkin, CA, *Assembly and organization processes in DNA-directed colloidal crystallization*. Proc Nat Acad Sci, 2009. **106**(26): p. 10493-10498.
 54. Christensen, ST, Lee, B, Feng, Z, Hersam, MC, and Bedzyk, MJ, *Hierarchical nanoparticle morphology for platinum supported on SrTiO₃(001): A combined microscopy and X-ray scattering study*. Appl Surf Sci, 2009. **256**: p. 423-427.

55. Rieker, T, Hanprasopwattana, A, Datye, A, and Hubbard, P, *Particle Size Distribution Inferred from Small-Angle X-ray Scattering and Transmission Electron Microscopy*. Langmuir, 1999. **15**: p. 638-641.
56. Park, SY, Lytton-Jean, AKR, Lee, B, Weigand, S, Schatz, GC, and Mirkin, CA, *DNA-programmable nanoparticle crystallization*. Nature, 2008. **451**: p. 553-556.
57. Biswas, K, Varghese, N, and Rao, CNR, *Growth Kinetics of Gold Nanocrystals: A Combined Small-Angle X-ray Scattering and Calorimetric Study*. Small, 2008. **4**(5): p. 649-655.
58. Gibaud, A, Dourdain, S, Gang, O, and Ocko, BM, *In situ grazing incidence small-angle x-ray scattering real-time monitoring of the role of humidity during the structural formation of templated silica thin films*. Phys Rev B, 2004. **70**(16): p. 161403.
59. Leroy, F, Revenant, C, Renaud, G, and Lazzari, R, *In situ GISAXS study of the growth of Pd on MgO(0 0 1)*. Appl Surf Sci, 2004. **238**(1-4): p. 233-237.
60. Renaud, G, Lazzari, R, Revenant, C, Barbier, A, Noblet, M, Ulrich, O, Leroy, F, Jupille, J, Borensztein, Y, Henry, CR, Deville, J-P, Scheurer, F, Mane-Mane, J, and Fruchart, O, *Real-Time Monitoring of Growing Nanoparticles*. Science, 2003. **300**(5624): p. 1416-1419.
61. Winans, RE, Vajda, S, Lee, B, Riley, SJ, Seifert, S, Tikhonov, GY, and Tomczyk, NA, *Thermal Stability of Supported Platinum Clusters Studied by in Situ GISAXS*. J Phys Chem B, 2004. **108**(47): p. 18105-18107.
62. Chen, M, Falkner, J, Guo, W-H, Zhang, J-Y, Sayes, C, and Colvin, VL, *Synthesis and self-organization of soluble monodisperse palladium nanoclusters*. J Coll Interface Sci, 2005. **287**: p. 146-151.
63. Barker, BD, *Electroless Deposition of Metals*. Surface Technology, 1981. **12**: p. 77-88.
64. Manocchi, AK, Horelik, NE, Lee, B, and Yi, H, *Simple, Readily Controllable Palladium Nanoparticle Formation on Surface-Assembled Viral Nanotemplates*. Langmuir, 2009. **26**(5): p. 3670-3677.
65. Manocchi, AK, Seifert, S, Lee, B, and Yi, H, *On the Thermal Stability of Surface-Assembled Viral-Metal Nanoparticle Complexes*. Langmuir, 2010. **26**(10): p. 7516-7522.
66. Lewis, CL, Lin, Y, Yang, C, Manocchi, AK, Yuet, KP, Doyle, PS, and Yi, H, *Microfluidic Fabrication of Hydrogel Microparticles Containing Functionalized Viral Nanotemplates*. Langmuir, 2010. **26**(16): p. 13436-13441.
67. Yang, C, Manocchi, AK, Lee, B, and Yi, H, *Viral Templated Palladium Nanocatalysts for Dichromate Reduction*. Appl Catal B: Environ, 2010. **93**(3-4): p. 282-291.
68. Yang, C, Manocchi, AK, Lee, B, and Yi, H, *Viral-templated palladium nanocatalysts for Suzuki coupling reaction*. J Mater Chem, 2010. **in press**.
69. Yang, C and Yi, H, *Facile approaches to control catalytic activity of viral-templated palladium nanocatalysts for dichromate reduction*. Biochem Eng J, 2010. **52**(2-3): p. 160-167.

70. Andre Guinier and Fournet, G, *Small Angle Scattering of X-rays*. 1955, New York: John Wiley and Sons.
71. Roe, R-J, *Methods of X-ray and Neutron Scattering in Polymer Science*. Topics in Polymer Science, ed. J.E. Mark. 2000, New York: Oxford University Press.
72. Vartanyants, IA, Zozulya, AV, Mundboth, K, Yefanov, OM, Richard, MI, Wintersberger, E, Stangl, J, Diaz, A, Mocuta, C, Metzger, TH, Bauer, G, Boeck, T, and Schmidbauer, M, *Crystal truncation planes revealed by three-dimensional reconstruction of reciprocal space*. Physical Review B, 2008. **77**(11): p. 115317.
73. Lee, B, Lo, C-T, Thiyagarajan, P, Winans, RE, Li, X, Niu, Z, and Wang, Q, *Effect of Interfacial Interaction on the Cross-Sectional Morphology of Tobacco Mosaic Virus Using GISAXS*. Langmuir, 2007. **23**(22): p. 11157-11163.
74. Jemian, PR, Weertman, JR, Long, GG, and Spal, RD, *Characterization of 9Cr-1MoVNb Steel by Anomalous Small-Angle X-ray Scattering*. Acta Metall Mater, 1991. **39**: p. 2477-2487.
75. Skilling, J and Bryan, RK, *Maximum entropy image reconstruction: general algorithm*. Mon. Not. R. astr. Soc, 1984. **211**: p. 111-124
76. Meneau, F, Sankar, G, Morgante, N, Winter, R, Catlow, CRA, Greaves, GN, and Thomas, JM, *Following the formation of nanometer-sized clusters by time-resolved SAXS and EXAFS techniques*. Faraday Discussions, 2002. **122**: p. 203-210.
77. Markiewicz, P and Goh, MC, *Atomic force microscopy probe tip visualization and improvement of images using a simple deconvolution procedure*. Langmuir, 1994. **10**(1): p. 5-7.
78. Glatter, O and Kratky, O, *Small-Angle X-ray Scattering*. 1982, London: Academic Press.
79. Coronado, E, Ribera, A, Garcia-Martinez, J, Linares, N, and Liz-Marzan, LM, *Synthesis, characterization and magnetism of monodispersed water soluble palladium nanoparticles*. J Mater Chem, 2008. **18**: p. 5682-5688.
80. Rao, CRK and Trivedi, DC, *Chemical and electrochemical depositions of platinum group metals and their applications*. Coord Chem Rev, 2005. **249**: p. 613-631.
81. Razvi, A and Scholtz, JM, *Lessons in stability from thermophilic proteins*. Protein Sci, 2006. **15**: p. 1569-1578.
82. Soares, RMD, Scremin, FF, and Soldi, V, *Thermal Stability of Biodegradable Films Based on Soy Protein and Corn Starch*. Macromol Symp, 2005. **229**: p. 258-265.
83. Yablokov, VA, Vasina, YA, Zelyaev, IA, and Mitrofanova, SV, *Kinetics of Thermal Decomposition of Sulfur-Containing Amino Acids*. Russ J Gen Chem, 2009. **79**(6): p. 1141-1145.
84. Heemeier, M, Stempel, S, Shaikhutdinov, SK, Libuda, J, Baumer, M, Oldman, RJ, Jackson, SD, and Freund, H-J, *On the thermal stability of*

- metal particles supported on a thin alumina film.* Surf Sci, 2003. **523**: p. 103-110.
85. Sullivan, JA, Flanagan, KA, and Hain, H, *Suzuki coupling activity of an aqueous phase Pd nanoparticle dispersion and a carbon nanotube/Pd nanoparticle composite.* Catal Today, 2009. **145**(1-2): p. 108-113.
 86. Kim, MH, Lee, B, Lee, S, Larson, C, Baik, JM, Yavuz, CT, Seifert, Sn, Vajda, S, Winans, RE, Moskovits, M, Stucky, GD, and Wodtke, AM, *Growth of Metal Oxide Nanowires from Supercooled Liquid Nanodroplets.* Nano Lett, 2009.
 87. Beaucage, G, Kammler, HK, and Pratsinis, SE, *Particle size distributions from small-angle scattering using global scattering functions.* J Appl Crystallogr, 2004. **37**: p. 523-535.
 88. Shu, J, Grandjean, BPA, Ghali, E, and Kaliaguine, S, *Autocatalytic Effects in Electroless Deposition of Palladium.* Journal of The Electrochemical Society, 1993. **140**(11): p. 3175-3180.
 89. Niederberger, M and Colfen, H, *Oriented attachment and mesocrystals: Non-classical crystallization mechanisms based on nanoparticle assembly.* Phys Chem Chem Phys, 2006. **8**: p. 3271-3287.
 90. Finney, EE and Finke, RG, *The Four-Step, Double-Autocatalytic Mechanism for Transition-Metal Nanocluster Nucleation, Growth, and Then Agglomeration: Metal, Ligand, Concentration, Temperature, and Solvent Dependency Studies.* Chem Mater, 2008. **20**: p. 1956-1970.
 91. Niu, Z, Bruckman, MA, Li, S, Lee, LA, Lee, B, Pingali, SV, Thiyagarajan, P, and Wang, Q, *Assembly of Tobacco Mosaic Virus into Fibrous and Macroscopic Bundled Arrays Mediated by Surface Aniline Polymerization.* Langmuir, 2007. **23**: p. 6719-6724.